

**CORTICAL LAYER-DEPENDENT HEMODYNAMIC REGULATION INVESTIGATED
BY FUNCTIONAL MAGNETIC RESONANCE IMAGING**

by

Cecil Chern-Chyi Yen

B.S. in Physics, National Tsing-Hua University, Taiwan, 1999

M.S. in Electrical Engineering, University of Pittsburgh, 2003

Submitted to the Graduate Faculty of
Swanson School of Engineering in partial fulfillment
of the requirements for the degree of
Doctor of Philosophy in Bioengineering

University of Pittsburgh

2011

UNIVERSITY OF PITTSBURGH
SWANSON SCHOOL OF ENGINEERING

This dissertation was presented

by

Cecil Chern-Chyi Yen

It was defended on

April 13, 2011

and approved by

George D. Stetten, MD/PhD, Professor

Howard J. Aizenstein, MD/PhD, Associate Professor

Mitsuhiro Fukuda, PhD, Assistant Professor

Justin C. Crowley, PhD, Assistant Professor, Carnegie Mellon University

Dissertation Director: Seong-Gi Kim PhD, Professor

Copyright © by Cecil Chern-Chyi Yen

2011

CORTICAL LAYER-DEPENDENT HEMODYNAMIC REGULATION INVESTIGATED BY FUNCTIONAL MAGNETIC RESONANCE IMAGING

Cecil Chern-Chyi Yen, PhD

University of Pittsburgh, 2011

Functional magnetic resonance imaging (fMRI) is currently one of the most widely used noninvasive neuroimaging modalities for mapping brain activation. Techniques such as blood oxygenation level dependent (BOLD) fMRI or cerebral blood volume (CBV)-weighted fMRI are based on the assumption that hemodynamic responses are tightly regulated by neural activity. However, the relationship between fMRI responses and neural activity is still unclear. To investigate this relationship, the unique properties of temporal frequency tuning of primary visual cortex neurons was used as a model since it can be used to separate the neural input and output activities of this area. During moving grating stimuli of 1, 2, 10 and 20 Hz temporal frequencies, two fMRI studies, areal and laminar studies, were conducted with different spatial resolution in a 9.4-T Varian spectrometer. In areal studies, BOLD fMRI was able to detect the difference in tuning properties between area 17 (A17), area 18 (A18) and lateral geniculate nucleus. In A17, the BOLD tuning curve seemed to reflect the local field potential (LFP) low frequency band (<12 Hz) rather than spiking activity and LFP gamma band (25-90 Hz). In laminar studies, a high spatial resolution protocol was adopted to resolve the different cortical layers in A17. In addition to BOLD fMRI, CBV-weighted fMRI was performed to eliminate the contamination from the superficial draining veins. These results showed that BOLD and CBV tuning curves do not reflect the underlying spiking activity or the LFP activity at infragranular layers (the bottom layer of three cortical layers). This implies that the hemodynamic response may not be regulated on a laminar level. Therefore, caution should be taken when interpreting

BOLD responses as the sole indicator of different aspects of neural activity in areal and laminar scales.

TABLE OF CONTENTS

1.0	INTRODUCTION.....	1
1.1	PHYSICS OF MAGNETIC RESONANCE.....	2
1.2	DEVELOPMENT OF FUNCTIONAL MAGNETIC RESONANCE IMAGING	10
1.2.1	Other functional neuroimaging modalities: PET and OIS.....	11
1.2.2	Blood oxygenation level dependent fMRI	13
1.2.3	Cerebral blood volume weighted fMRI.....	20
1.2.4	Neurophysiology of fMRI	26
1.3	OVERVIEW OF THE EARLY VISUAL SYSTEM.....	29
1.4	ORGANIZATION OF THE THESIS.....	34
2.0	BOLD RESPONSES TO DIFFERENT TEMPORAL FREQUENCY STIMULI IN THE LATERAL GENICULATE NUCLEUS AND VISUAL CORTEX: INSIGHTS INTO THE NEURAL BASIS OF FMRI.....	36
2.1	ABSTRACT.....	36
2.2	INTRODUCTION	37
2.3	MATERIALS AND METHODS.....	39
2.3.1	Procedures of animal preparation	39
2.3.2	Paradigm of visual stimulation.....	40
2.3.3	Protocol of MRI acquisition.....	42
2.3.4	Generation of fMRI maps.....	43

2.3.5	Quantitative region of interest analysis	44
2.4	RESULTS	45
2.4.1	Spatiotemporal characteristics of BOLD responses for various temporal frequency stimuli	45
2.4.2	BOLD temporal frequency tuning curve and preference maps.....	48
2.5	DISCUSSION	52
2.5.1	Preferred temporal frequency in early visual systems.....	52
2.5.2	Dynamic property of visual evoked response in early visual system	55
2.5.3	Relationships between BOLD, tissue pO ₂	56
2.5.4	Relationships between BOLD and neural activity.....	58
2.5.5	Conclusion	59
2.5.6	Acknowledgments	59
3.0	SOURCE OF CORTICAL LAYER-DEPENDENT HEMODYNAMIC RESPONSE STUDIED BY VISUAL STIMULUS OF TEMPORAL FREQUENCY	61
3.1	ABSTRACT	61
3.2	INTRODUCTION	62
3.3	MATERIALS AND METHODS	64
3.3.1	Animal preparation	64
3.3.2	Visual stimulation	65
3.3.3	MRI acquisition	66
3.3.4	fMRI maps generation	66
3.3.5	Quantitative region of interest analysis of temporal frequency stimulus.	67
3.4	RESULTS	68
3.5	DISCUSSION	72

3.5.1	Layer-dependent temporal frequency preference	72
3.5.2	Comparison to other studies	73
3.5.3	Potential limitations.....	74
3.5.4	Conclusion	75
3.5.5	Acknowledgments	76
4.0	SUMMARY AND FUTURE DIRECTIONS.....	77
4.1	SUMMARY	77
4.2	FUTURE DIRECTIONS.....	78
4.2.1	Hypercapnia challenge to investigate layer-dependent functional vascular reactivity	78
4.2.2	Optogenetic fMRI to study laminar hemodynamic regulation in a single cortical layer.....	80
	BIBLIOGRAPHY	82

LIST OF TABLES

Table 1.2.1 Susceptibility of selected substance in the brain (normal temperature, 1 atm)	15
Table 3.5.1 Temporal frequency preference of known spiking activity and predicted synaptic activity.....	73

LIST OF FIGURES

Figure 1.1 Motion of the magnetization vector in the presence of an oscillating magnetic field...	7
Figure 1.2 Relaxation behaviors of the magnetization with different T_1 and T_2	9
Figure 1.3 Simulated hemoglobin oxygen dissociation curves of cat and human.....	14
Figure 1.4 Diffusion of water molecules in the vicinity of red blood cells, capillaries/venules and large vein.....	17
Figure 1.5 A map of change of R_2^* induced by intravascular MION in feline brain.....	23
Figure 1.6 A schematic diagram of the cerebral microcirculation.....	27
Figure 1.7 Flowcharts of BOLD (a) and CBV-weighted (b) fMRI signal changes induced by neural activity.....	28
Figure 1.8 A schematic diagram of the feline early visual system.....	30
Figure 1.9 A zoomed cross section of feline cortical areal 17 stained with Luxol fast blue / Cresyl violet.....	31
Figure 1.10 A schematic diagram of blood circulation in the human visual cortex.....	33
Figure 2.1 Stimulus paradigm and regions of the early visual areas.....	41
Figure 2.2 Temporal frequency-dependent BOLD activation maps and time courses.....	46
Figure 2.3 Dynamic properties of BOLD responses in the early visual areas.....	47
Figure 2.4 Temporal frequency tuning curves of the early visual areas with BOLD fMRI, pO_2 , LFP and spiking activity.....	49
Figure 2.5 Temporal frequency preference maps with BOLD fMRI.....	51
Figure 3.1 Defining regions of three cortical layers.....	67
Figure 3.2 Activation maps of laminar BOLD (A-B) and CBV-weighted (C-D) fMRI activation maps for different temporal frequencies.....	69
Figure 3.3 Laminar BOLD (A-C) and relative CBV (D-F) response time-courses of different temporal frequencies.....	70
Figure 3.4 Temporal frequency tuning curves of laminar BOLD fMRI (A) and relative CBV fMRI (B).....	71

Figure 4.1 (A) CBV-weighted fMRI t-Test map of hypercapnic challenge in one animal and
(B) normalized CBV-weighted layer profiles of hypercapnic challenge and visual
stimulation from three animals. 79

PREFACE

I am sincerely grateful to my advisor, Dr. Seong-Gi Kim, for supporting me with the graduate research assistantship, guiding my research and mentoring my graduate work. I also like to thank all my committee members, Dr. Howard J. Aizenstein, Dr. Justin C. Crowley, Dr. Mitsuhiro Fukuda and Dr. George Stetten for their time and comments. Especially, I thank Dr. Fukuda for helping me to do experiments using optical intrinsic signal and providing helpful advice on the neurophysiological aspect of my study. I also thank Dr. Stetten for mentoring me in teaching the class of electronic laboratory.

I also appreciate all the helps from current and former members of Neuroimaging laboratory at University of Pittsburgh. In particular, I thank Dr. Vazquez for helping me to calibrate the temporal frequency visual stimuli; I thank Dr. Jin and Dr. Kim for his helpful discussion in my manuscript and experiment design; I thank Mrs. Hendrich for 9.4T support and proofreading my manuscripts; I thank Dr. Wang for preparing animals for my experiments and assisting me on maintaining the animal condition; I thank Dr. Park for providing his pulse sequences and helpful discussion on image reconstruction algorithm; I thank Dr. Moon for his helps in orientation column experiments and giving his post-processing and analysis code to me; I thank Dr. Hayashi for his useful discussion in using FSL and analysis methods; I thank Dr. Zhao for providing his hypercapnia challenge data, and I thank Dr. Poplawsky for proofreading my manuscript. In addition, I like to thank Dr. Ite Yu, Dr. Jow-Tsong Shy, Dr. Mahmoud El Nokali, Dr. Yi Wang, Dr. Ching-Chung Li, Dr. Mingui Sun, Dr. Chen Chang, Dr. Hsiao-Wen

Chung, and Dr. Constance Chu for their helps during my PhD studies or in the past. I thank all my friends including Kuang-Lung Hsueh, Chien-Yuan Lin and my sister, Chern-Yu Sherry Yen, for their support in my personal life.

Finally, I like to dedicate this thesis to my parents as well as my wife, Chi-yin Lui. Without their constant support and trust, I will not be able to finish this thesis.

1.0 INTRODUCTION

Functional magnetic resonance imaging (fMRI) is currently the method of choice to noninvasively map neural activity in the central nervous system of mammals. Neuroscientists and psychologists have applied fMRI to identify cognitive function of brain regions and connectivity among its areas (9). However, most fMRI methods do not measure neural activity directly. Instead, fMRI measures signal changes associated with the hemodynamic response, such as cerebral blood volume (CBV), cerebral blood flow (CBF) and blood oxygen level dependent (BOLD) contrast, as the surrogate for the underlying neural activity. Many efforts have been made in the past decade to understand the relationship between the hemodynamic response and the underlying neural activity, especially the spatial localization of the fMRI signal to the neural activity (10, 11). The consensus is that, with a volumetric picture element (voxel) size of several cubic millimeters, the fMRI signal change co-localizes with the site of increasing neural activity (12).

As fMRI techniques improve, researchers are currently able to probe the hemodynamic response with a sub-cubic-millimeter voxel size, which develops concerns regarding the spatial localization of the fMRI signal to neural activity at this microscopic scale. To study the sub-cubic-millimeter spatial co-localization, a feline model of cortical layer-dependent hemodynamic regulation is used here. The discussion of cortical layer-dependent fMRI shall begin with an

introduction to the physical principles of MR, followed by the mechanism of fMRI and an overview of the feline early visual system.

1.1 PHYSICS OF MAGNETIC RESONANCE

Magnetic resonance imaging (MRI) was developed by Paul Lauterbur and Peter Mansfield, based on the physics of nuclear magnetic resonance (NMR), more than 30 years ago (13, 14). Today, MRI is one of the most popular *in vivo* imaging modalities to visualize almost every organ system, such as the central nervous system, cardiovascular, and musculoskeletal systems. The advantages of MRI over other *in vivo* imaging modalities includes noninvasiveness, negligible radiation deposition, flexible selection of inclination and depth of the imaging plane, and, most importantly, its ability to portray the soft tissue and vasculature with various contrast depending on the imaging protocols. In this section, the basic of MR physics is elucidated.

NMR consists of three key elements:

- 1) Nuclei with a non-zero nuclear magnetic dipole momentum
- 2) External static magnetic field
- 3) Resonance phenomena during radiation of an oscillating magnetic field

The first key element, the nuclear magnetic dipole moment or magnetic moment (μ), was discovered by two physicists, Gerlach and Stern in 1922 (15). The magnetic moment has units of Joule/Tesla. This vector quantity indicates the tendency of nuclei to align with magnetic fields and is determined by another vector quantity, the nuclear spin angular momentum or spin (\mathbf{I}), and a nucleus-dependent constant, the gyromagnetic ratio (γ). Spin is an intrinsic property of the particle and has the same unit as classical angular momentum: Joule/second. The value of the

gyromagnetic ratio depends on nucleus and is influenced by its surrounding nuclear environment (chemical shift). For example, γ , defined as $\gamma/2\pi$, is equal to 4.25764×10^7 Hz/Tesla for the hydrogen nucleus of water molecules, compared to 4.25775×10^7 Hz/Tesla for the hydrogen nucleus (16). The positive sign of γ indicates that the magnetic moment is parallel to the nuclear spin angular momentum. The relation of these three quantities can be expressed as

$$\boldsymbol{\mu} = \gamma \mathbf{I} \quad (1.1)$$

Equation 1.1 implies that the magnetic moment will precess under the influence of an external magnetic field at certain angular frequency. This is analogous to a spinning top wobbling under a gravity field from the classical physics' point of view.

Since the magnetic moment is a vector quantity, it has magnitude and direction. The magnitude of the magnetic moment is proportional to the magnitude of the spin and is determined by the nuclear spin quantum number (I). Hence, the magnitude of the magnetic moment can be rewritten to include I as

$$|\boldsymbol{\mu}| = \mu = \gamma \hbar [I(I+1)]^{1/2} \quad (1.2)$$

In equation 1.2, I can be zero, an integral or a half-integral following three rules as described below:

- 1) Nuclei with an even number of protons and an even number of neutrons possess a zero spin number.
- 2) Nuclei with an odd number of protons and an odd number of neutrons possess an integral spin number.
- 3) Nuclei with an odd number of protons plus a neutron possess a half-integral spin number.

Nuclei with $I = 0$, i.e. no magnetic moment, cannot be detected by NMR. For example, the hydrogen nucleus, the most commonly used nucleus in MRI, has a nuclear spin quantum number of $\frac{1}{2}$.

Although the magnitude of the magnetic moment is known for a given nucleus and its surrounding nuclear environment, the direction of the magnetic moment is random due to the thermal motion of the atom. If an external static magnetic field (\mathbf{B}) is applied to the experimental object, the magnetic moment inside the object will tend to align with the external magnetic field. Note that \mathbf{B} has unit of Tesla and is sometime referred to as the magnetic flux density. This phenomenon can be explained by the second law of thermodynamics that spin tends to stay at the lowest possible energy state and the magnetic energy of this system is

$$\text{Magnetic Energy} = -\boldsymbol{\mu} \cdot \mathbf{B} \quad (1.3)$$

Thus, the negative sign in front of the magnetic moment suggests the lowest magnetic energy occurs when the magnetic moment is parallel to the external magnetic field. We know from quantum mechanism that the state of magnetic energy for spin is quantized and that the number of states is determined by I . For nuclei with $I = \frac{1}{2}$, like hydrogen nuclei or fluorine-19, only two energy states exist.

For $I = \frac{1}{2}$ nuclei, the magnetic moment ($\boldsymbol{\mu}$) precesses along the two pre-defined directions under the static magnetic field (\mathbf{B}). To describe the precession of the spin, we need to look at the torque applied to the spin. The torque, which is equal to the change rate of the spin (\mathbf{I}), experienced by the magnetic moment can be express as:

$$\text{Torque} = d\mathbf{I}/dt = \boldsymbol{\mu} \times \mathbf{B} \quad (1.4)$$

Substituting equation 1.1 into equation 1.4, we have

$$d\boldsymbol{\mu}/dt = \gamma \boldsymbol{\mu} \times \mathbf{B} \quad (1.5)$$

This is the equation of motion for an individual spin in the classical physics treatment. Without loss of generality, assuming \mathbf{B} is applied in the z-direction $\mathbf{B} = (0,0,B_0)$ and using the complex representation to simplify the solution, equation 1.5 can be solved as following

$$\mu_{xy}(t) \equiv \mu_x(t) + i\mu_y(t) = \mu_{xy}(0) e^{-i\gamma B_0 t} \quad (1.6)$$

$$\mu_z(t) = \mu_z(0) \quad (1.7)$$

where $\mu_{xy}(0) \equiv \mu_x(0) + i\mu_y(0)$ and $\mu_z(0)$ are the initial conditions. The angular frequency of nuclear precession (ω_0), or the Larmor frequency, is defined as $-\gamma B_0$. For $\gamma > 0$, like the proton, the Larmor frequency is negative and the precession direction of the spin is clockwise, if observed against the direction of the magnetic field.

To describe the phenomenon observed in MR experiments, which is the vector summation of individual magnetic moments, a macroscopic magnetization vector (\mathbf{M}) is introduced. Magnetization can be defined as:

$$\mathbf{M} \equiv \sum \boldsymbol{\mu} / V \quad (1.8)$$

where V is the volume and the units of \mathbf{M} is Ampere/Meter. The time evolution of the magnetization, known as the Bloch equation, can then be derived from equation 1.5 as following:

$$d\mathbf{M}/dt = \gamma \mathbf{M} \times \mathbf{B} - \mathbf{R} \cdot (\mathbf{M} - \mathbf{M}(0)) \quad (1.9)$$

where \mathbf{R} is the relaxation matrix returning the magnetization back to its initial condition (equilibrium or lowest energy state) and $\mathbf{B}(t)$ is the static magnetic field in the z direction plus a time varying magnetic field, which include oscillating and gradient magnetic fields. Substituting $\mathbf{R} = (R_2, R_2, R_1)$, $\mathbf{M}(0) = (0, 0, M_0)$, $\mathbf{M} = [M_x(t), M_y(t), M_z(t)]$ and $\mathbf{B}(t) = [B_x(t), B_y(t), B_z(t)]$ into equation 1.9, we determine the Bloch equation at its stationary coordinates:

$$dM_x(t)/dt = \gamma [M_y(t)B_z(t) - M_z(t)B_y(t)] - R_2 M_x(t) \quad (1.10)$$

$$dM_y(t)/dt = \gamma [M_z(t)B_x(t) - M_x(t)B_z(t)] - R_2 M_y(t) \quad (1.11)$$

$$dM_z(t)/dt = \gamma [M_x(t)B_y(t) - M_y(t)B_x(t)] - R_1[M_z(t)-M_0] \quad (1.12)$$

where M_0z is the magnetization at the equilibrium state. R_2 ($=1/T_2$) is the spin-spin relaxation rate, which refers to the exchange rate of energy between nuclei as they approach each other, and R_1 ($=1/T_1$) is the spin-lattice relaxation rate, which is the exchange rate of energy between the nuclei and its surrounding lattice. R_1 and R_2 values vary depending on the motion of the spin, surrounding temperature, and static magnetic field.

From the Bloch equation, we can calculate the magnetization during the excitation pulse. Assuming the duration of the excitation pulse is relatively short compared to T_1 and T_2 , the relaxation matrix \mathbf{R} can be neglected during excitation. Equation 1.9 becomes:

$$d\mathbf{M}/dt = \gamma \mathbf{M} \times \mathbf{B} \quad (1.13)$$

and is very similar to equation 1.5 for the time evolution of the individual spin. Mathematically, the above equation is not intuitive to be understood under stationary coordinates due to the magnetization precessing at Larmor frequency (ω_0) in the x-y (transverse) plane. Therefore, the rotating coordinate, in which the x-y plane rotates clockwise along the z-axis at a certain frequency (ω), is introduced to replace the stationary coordinate. Let the three axes of the rotating frame be defined as:

$$\mathbf{x}' \equiv \cos(\omega t)\mathbf{x} - \sin(\omega t)\mathbf{y} \quad (1.14)$$

$$\mathbf{y}' \equiv \cos(\omega t)\mathbf{x} + \sin(\omega t)\mathbf{y} \quad (1.15)$$

$$\mathbf{z}' \equiv \mathbf{z} \quad (1.16)$$

And let

$$\mathbf{M}_{\text{rot}} \equiv M_{x'}(t)\mathbf{x}' + M_{y'}(t)\mathbf{y}' + M_{z'}(t)\mathbf{z}' \quad (1.15)$$

$$\partial\mathbf{M}_{\text{rot}}/\partial t \equiv dM_{x'}(t)/dt \mathbf{x}' + dM_{y'}(t)/dt \mathbf{y}' + dM_{z'}(t)/dt \mathbf{z}' \quad (1.16)$$

$$\mathbf{B}_{\text{rot}} \equiv B_{x'}(t)\mathbf{x}' + B_{y'}(t)\mathbf{y}' + B_{z'}(t)\mathbf{z}' \quad (1.17)$$

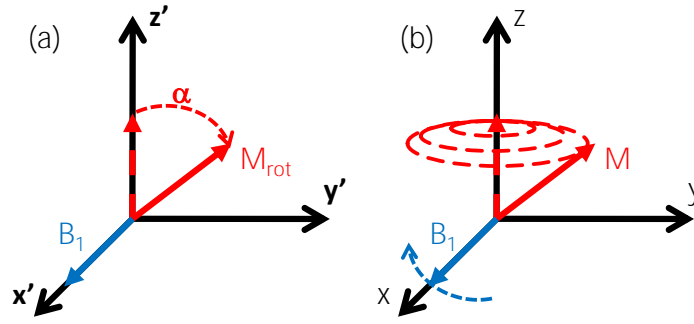


Figure 1.1 Motion of the magnetization vector in the presence of an oscillating magnetic field.

(a) M_{rot} precesses along B_1 in the rotating coordinate of frequency ω_0 (b) M nutates toward the x-y plane in the stationary coordinate

Then, equation 1.13 can be rewritten as

$$d\mathbf{M}/dt = \partial\mathbf{M}_{rot}/\partial t + \boldsymbol{\omega} \times \mathbf{M}_{rot} \quad (1.18)$$

where $\boldsymbol{\omega}$ is $-\omega\mathbf{z}$. Next, we substitute equation 1.17 into 1.13 and we have

$$\partial\mathbf{M}_{rot}/\partial t = \gamma\mathbf{M}_{rot} \times \mathbf{B}_{rot} - \boldsymbol{\omega} \times \mathbf{M}_{rot} = \gamma\mathbf{M}_{rot} \times \mathbf{B}_{eff} \quad (1.19)$$

where $\mathbf{B}_{eff} = \mathbf{B}_{rot} + \boldsymbol{\omega}/\gamma$ is the effective magnetic field that \mathbf{M} experiences in the rotating coordinate. If an additional time-varying magnetic field $B_1(t)\mathbf{x}'$, or the excitation pulse, is applied onto the magnetization with an oscillating frequency equal to the Larmor frequency ($\omega_0 = \gamma B_0$), then

$$\mathbf{B}_{eff} = B_0\mathbf{z}' + B_1(t)\mathbf{x}' - \omega_0/\gamma \mathbf{z}' = B_1(t)\mathbf{x}' \quad (1.20)$$

Since the Larmor frequency of the proton is at the range of radiofrequency (RF), the time-varying $B_1(t)$ is also called RF magnetic field, or RF pulse, when it is turned on for a very short period of time. Now, \mathbf{B}_{eff} essentially equals to \mathbf{B}_1 and the magnetization only experiences the external \mathbf{B}_1 . This condition is referred as on resonance excitation condition. We substitute equation 1.20 into 1.19, and then we have

$$\partial\mathbf{M}_{rot}/\partial t = \gamma\mathbf{M}_{rot} \times \mathbf{B}_1 \quad (1.21)$$

The above equation indicates that \mathbf{M}_{rot} precesses along the direction of the external magnetic field \mathbf{B}_1 , which is \mathbf{x}' in the rotating coordinates. The angle α of the magnetization moving toward the transverse is determined by the magnitude and the duration of the \mathbf{B}_1 . Looking from stationary coordinate, the magnetization nutates toward the transverse plane. The motion of the magnetization in two coordinates can be illustrated in the schematic drawing in Figure 1.1.

After the magnetization has been perturbed from the initial equilibrium state by an additional RF pulse, it will return to the initial state according to the second law of the thermodynamics. This process can be described in the rotating coordinate by first transforming the Bloch equation 1.9 in the stationary coordinates into the rotating coordinates as

$$\partial\mathbf{M}_{\text{rot}}/\partial t = \gamma\mathbf{M}_{\text{rot}} \times \mathbf{B}_{\text{eff}} - \mathbf{R} \cdot (\mathbf{M}_{\text{rot}} - \mathbf{M}_{\text{rot}}(0)) \quad (1.22)$$

Then, in the Larmor frequency rotating coordinates, $\partial\mathbf{M}_{\text{rot}}/\partial t = -\mathbf{R} \cdot (\mathbf{M}_{\text{rot}} - \mathbf{M}_{\text{rot}}(0))$. Solving the above equation, we have

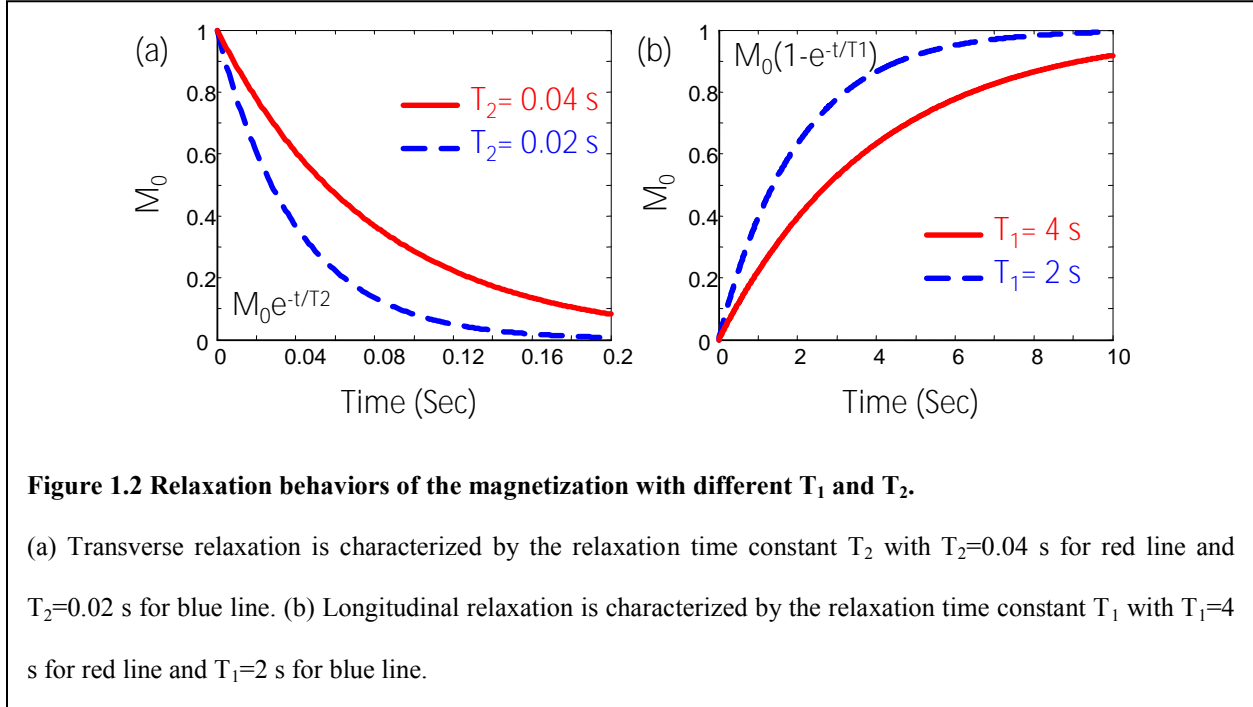
$$M_{x'y'}(t) \equiv M_{x'}(t) + iM_{y'}(t) = M_{x'y'}(0+) e^{-R2t} \quad (1.23)$$

$$M_{z'}(t) = M_0(1 - e^{-R1t}) + M_{z'}(0+)e^{-R1t} \quad (1.24)$$

where the new initial condition $M_{x'y'}(0+)$ and $M_{z'}(0+)$ are the magnetization on the transverse plane and along z-axis right after the RF pulse. M_0 is the magnetization of the equilibrium state. If the magnetization is on the transverse plane after the RF pulse, i.e. $\alpha = 90^\circ$, then $M_{x'y'}(0+) = M_0$ and $M_{z'}(0+) = 0$. Substituting them into 1.23 and 1.24, we can describe the motion of $M_{x'y'}$ and $M_{z'}$ during the relaxation and is illustrated in Figure 1.2. To develop a desired T_2 contrast, longer duration between the RF excitation and the signal acquisition is favorable. This duration is termed the echo time (TE). On the other hand, to develop a desired T_1 contrast, shorter

duration between two repeated RF excitations is favorable. This duration is termed the repetition time (TR).

If the static magnetic field (B_0) is spatially inhomogeneous, it introduces another



relaxation term, T_2' . Since the Larmor frequency is proportional to B_0 , field heterogeneity changes the resonance frequency of the nearby spins, which reduces the coherence of the phase of the magnetization vector. The incoherence of the phase results in anti-synchronization of the magnetization vector and loss of the net magnetization observed in transverse plane. Therefore, apparent T_2 , or simply T_2^* , measured on a MR instrument, is shorter than the intrinsic spin-spin relaxation time, T_2 . The relation of these three quantities is

$$1/T_2^* = 1/T_2 + 1/T_2' \quad \text{or} \quad R_2^* = R_2 + R_2' \quad (1.25)$$

The incoherence of the phase originating from field inhomogeneities can be refocused by applying additional RF pulse to rotate the magnetization by 180 degrees. Immediately after the 180° RF pulse, the magnetization starts to refocus at the same rate as they dephased. The recovered MR signal is called a spin echo. Note that unless a Carr-Purcell pulse train or a spin-

lock pulse are applied, a 180° RF refocusing pulse can only refocus the magnetization loss due to diffused spins experience relatively smooth field inhomogeneity during TE. In the above two special types of magnetization preparation, additional relaxation mechanisms of $T_{1\rho}$ and/or $T_{2\rho}$ are introduced, which is beyond the scope of this thesis. Thus, in practice, T_2 measured by the spin echo experiment contains the intrinsic T_2 and any irreversible factors, such as diffusion.

In summary, the MRI signal can be expressed in equation 1.26 without loss of generality

$$S = S_0(1 - e^{-TR/T_1})e^{-TE/T_2^*} \quad (1.26)$$

where S is the MR signal intensity measured at a certain TR and TE, whereas S_0 is the MR signal intensity measured at $TR = \infty$ and $TE = 0$. If the voxel contains multiple compartments with different T_1 and T_2^* , the total signal is the summation of MR signal of the individual compartments multiplied by their volume fraction.

1.2 DEVELOPMENT OF FUNCTIONAL MAGNETIC RESONANCE IMAGING

Since the discovery of blood oxygenation level dependent (BOLD) fMRI (17-21) and cerebral blood volume (CBV) weighted fMRI (22), fMRI has become the most widely accepted tool to map the functional activities of the brain (23). fMRI has revolutionized cognitive neuroscience and neurophysiology because of the combination of noninvasiveness and high spatiotemporal resolution compared to other well-known neuroimaging modalities, such as positron emission tomography (PET) and optical imaging of intrinsic signals (OIS). Before introducing the development of fMRI, let me explain the development of PET and OIS and their advantages and disadvantages.

1.2.1 Other functional neuroimaging modalities: PET and OIS

PET is one of the first noninvasive neuroimaging tools to study the function of the human brain (24). PET uses exogenous radioactive tracers, which emit positrons and generate pairs of high-energy photons when they interact with electrons by annihilation. The entire mass of the electron-positron pair is converted into two 511-kiloelectronvolt photons emitted in opposite directions. These photons, in the frequency range of a gamma ray, are then detected to form the grounds of PET. PET can be used to measure many physiological parameters like CBF, CBV, cerebral glucose consumption rate ($CMR_{Glucose}$), and cerebral oxygen consumption rate (CMR_{O_2}) with various tracers. For example, ^{15}O labeled H_2O has been used to measure CBF (25) and CBV (26, 27), ^{18}F labeled fludeoxyglucose has been used to measure $CMR_{Glucose}$ (28). However, the spatial resolution of PET is currently limited to 2 mm for clinical PET and 1 mm for animal microPET systems (29), which are much worse than that of high-field MRI. In addition, the temporal resolution is also relatively poor compared to fMRI. The biggest disadvantage of utilizing PET in functional neuroimaging is the restriction on the number of repetitive measurements that can be made on a subject due to the accumulation of radiation exposure from the radioactive tracers. Repetitive measurement is necessary for comparing resting state versus stimulus state and for signal averaging.

Another important tool to study brain function is OIS. OIS is based on the fact that the light absorption rate of oxyhemoglobin (oxyHb) and deoxyhemoglobin (deoxyHb) have different wavelength dependencies (30). To perform an OIS experiment, the cortical surface has to be first exposed and illuminated through an interference filter connected to a tungsten-halogen light source. Then, a charge coupled device (CCD) is used to capture the reflected light from the tissue. At about 570 nm wavelength of illumination, the absorption rate is identical for

oxyhemoglobin and deoxyhemoglobin. Thus, the reflected light is weighted toward total hemoglobin concentration in the imaging area and is conceptually similar to the CBV-weighted fMRI. At around 620 nm, the absorption rate of oxyhemoglobin is negligible compared with that of deoxyhemoglobin. Consequently, the reflected light emphasizes the change in deoxyhemoglobin and is conceptually similar to BOLD fMRI. OIS has been proved to robustly map orientation columns and many other functional structure in the cat visual cortex (31). The biggest advantage of OIS is its excellent spatiotemporal resolution, which is only limited by the quality of the CCD and the signal to noise ratio. In a typical OIS experiment performed in our laboratory, the spatial resolution is about 27.5 μm and the temporal resolution is a few hundred milliseconds. The drawback of the OIS technique is its invasiveness, which disturbs the neurophysiology of the subject and renders it unsuitable for imaging human subject. Also, OIS can only image the surface of the cortex with a penetration depth of few hundred micrometers and thus can't be used to study the hemodynamic regulation of cortical layers, which are usually thicker than 1 mm.

Compared to fMRI, other neuroimaging modalities either suffer from lower spatiotemporal resolution, like PET, magnetoencephalography and near infrared spectroscopy; or restricted application due to invasiveness, like OIS, two-photon microscopy and electrophysiology. Hence, fMRI has its unique advantages of being a noninvasive neuroimaging method, while keeping good spatiotemporal resolution. It is also the method of choice in human brain mapping. However, the relationship between the hemodynamic response and the underlying neural activity is still unclear after decades of research. This uncertainty prevents us from interpreting of the fMRI signal, or signal from any hemodynamic-based neuroimaging

technique, as the underlying neural process. Therefore, in the following sections, the basics of BOLD fMRI and CBV weighted fMRI will be elucidated.

1.2.2 Blood oxygenation level dependent fMRI

BOLD contrast relies on the change in magnetic properties of hemoglobin binding to oxygen (17). Hemoglobin (Hb) is an oxygen-transport protein existing in the red blood cells of all vertebrates, except crocodiles and icefish. Each hemoglobin protein contains four subunits; each subunit can combine with four molecules of oxygen, and the binding reactions of the four subunits occur cooperatively. The oxygen-hemoglobin dissociation curve has a sigmoidal shape and can be described by the Hill equation:

$$Y = [\text{OxyHb}] / [\text{Total Hb}] = (\text{PO}_2)^n / [(\text{P}_{50})^n + (\text{PO}_2)^n] \quad (1.27)$$

where Y is the oxygen saturation level, PO_2 is the partial pressure of oxygen (mmHg), P_{50} is the oxygen partial pressure when Y become 50% (mmHg) and n is the Hill coefficient. In cat, P_{50} is 36.8 mmHg and n is 3.207 (6), which are larger than that of human ($\text{P}_{50} = 26$ mmHg and $n = 2.8$). The simulated curved for both species can be found in Figure 1.3. In normal baseline condition, Y is around 100%, 80% and 60% for blood in arteries, capillaries and veins, respectively. The hemoglobin's affinity for oxygen is influenced by several factors including blood P_{CO_2} , H^+ concentration, temperature, and the concentration of 2,3-diphosphoglycerate. Increasing the H^+ and/or carbon dioxide concentrations reduces the oxygen affinity of hemoglobin, which is known as Bohr Effect. In addition to oxygen, hemoglobin also binds to carbon dioxide and forms carbaminohemoglobin. About 20% - 30% of the carbon dioxide is carried away from the tissue by carbaminohemoglobin in the red blood cells (32).

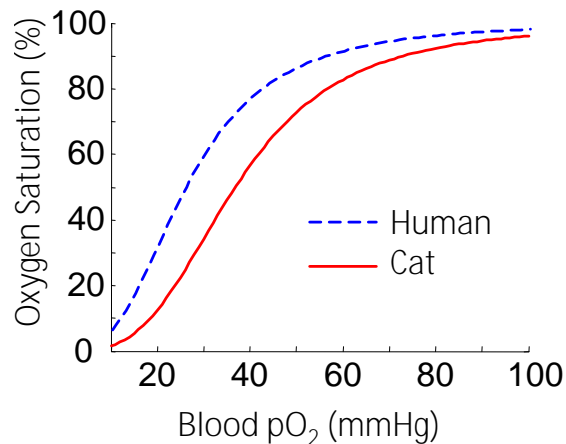


Figure 1.3 Simulated hemoglobin oxygen dissociation curves of cat and human.

The simulated curve was generated from equation 1.27. In cat, P_{50} is 36.8 mmHg and n is 3.207 (6) which are both larger than that of human where P_{50} is 26 mmHg and n is 2.8. Thus, feline hemoglobin dissociation curve is slightly shifted to the right comparing to that of human.

According to early works done by Pauling and Coryell, oxyhemoglobin and deoxyhemoglobin protein have been known to be diamagnetic and paramagnetic, respectively (33). By definition, paramagnetic or diamagnetic material possesses positive or negative volume magnetic susceptibility, or susceptibility in short, (χ) under room temperature and atmospheric pressure. χ is the ratio, which is dimensionless in international system (SI) units, of magnetization of a substance placed within a magnetic field and is equal to zero in a vacuum. Note that most literatures reported χ in centimeters-grams-seconds (CGS) unit and a factor of 4π are required to convert it to SI units. χ originates from i) the magnetic moment of the electrons, ii) the orbital motion of the electrons, and iii) the magnetic moment of nuclei. Mostly, the orbital motion of the electrons contributes a negative value to the susceptibility, whereas electron and nuclear magnetic moments contribute a positive value. However, nuclear magnetic moments are many orders smaller than that of electrons and, therefore, its contribution to the overall χ is usually negligible. In paramagnetic substances, the contribution from the magnetic

moment of the electrons is greater than the orbital motion of the electrons. When the iron core of the hemoglobin does not bind to any oxygen, i.e. deoxyhemoglobin, it exhibits paramagnetic properties due to the strong magnetic moment of unpaired electrons from the iron. In contrast, when the iron core of the hemoglobin binds to oxygen molecules to form oxyhemoglobin, there is no magnetic moment of unpaired electrons and, thus, it is diamagnetic. Susceptibility of some substances of the brain is listed in table 1.2.1. χ_{blood} can be expressed as a function of Hct and Y (34)

$$\chi_{\text{blood}} = \text{Hct}(Y \chi_{\text{oxy}} + (1-Y)\chi_{\text{deoxy}}) + (1 - \text{Hct})\chi_{\text{plasma}} \quad (1.28)$$

where χ_{oxy} and χ_{deoxy} are the susceptibilities of fully oxygenated blood and deoxygenated blood, respectively, as listed in table 1.2.1. When $Y=1$ and $\chi_{\text{plasma}} \sim \chi_{\text{oxy}} \sim \chi_{\text{water}}$ is approximated, then χ_{blood} is equal to χ_{water} . Since Hct is relatively constant under normal physiological conditions, Y is the key factor in determining χ_{blood} .

Table 1.2.1 Susceptibility of selected substance in the brain (normal temperature, 1 atm)

Substance	χ (10^{-6} or ppm) in SI unit
Water	-9.01 (35)
Oxygen	1.75 (35)
Room air (78% N ₂ , 21% O ₂ , 1% Ar)	0.36 (35)
Lipid family	Anisotropic, averaged -10 (36)
Cortical bone	-8.70 (36)
Oxyhemoglobin	-9.91 (36)
Deoxyhemoglobin	0.20 (36)
Fully oxygenated whole blood (χ_{oxy})	-9.25 (37)
Fully deoxygenated whole blood (χ_{deoxy})	-5.93 (37)
Blood plasma (χ_{plasma})	Estimated -9.07 (37)

Changes in χ_{blood} induce a change in the magnetic field (ΔB) depending on the relative position of the blood vessel. To simplify our calculation, a single vessel can be modeled as an infinite cylinder. For intravascular compartments, the magnetic field change (ΔB_{intra}) induced by deoxyHb can be expressed by equation 1.29 (38)

$$\Delta B_{\text{intra}} = \Delta\chi/2 B_0(\cos^2\theta - 1/3) \quad (1.29)$$

where $\Delta\chi = \chi_{\text{blood}} - \chi_{\text{water}}$ (the susceptibility difference between blood and water), B_0 is the static magnetic field, and θ is the angle between the direction of B_0 and the orientation of the vessel. Note that the susceptibility of the arterial blood is close to that of water, resulting in $\Delta B_{\text{intra}}=0$ within the arteries and considering venous or capillary blood for BOLD contrast. Within a given voxel, vessels in the brain have many different orientations, which induce inhomogeneity of the local magnetic field. Hence, recalling from the previous section, T_2' is shortened by inhomogeneity of the magnetic field within each voxel. Besides affecting T_2' , the presence of deoxyhemoglobin also shortens T_2 of the blood. Assuming water molecules diffuse like Brownian motion in the blood vessel with a diffusion coefficient (D) close to $2.96 \mu\text{m}^2/\text{ms}$ (39), then during TE (typically 20 ms to optimize the contrast for the functional studies (40)) the diffusion length (λ) of water spins can be estimated by (41)

$$\lambda = (6 D TE)^{1/2} \quad (1.30)$$

to be about $19 \mu\text{m}$. This length is larger than the diameter of the red blood cell ($7.9 \mu\text{m}$ for human and $5.8 \mu\text{m}$ for cats (42)). Hence, during TE, the nuclear spin of the water molecule experiences dramatic magnetic field variations around the vicinity of many paramagnetic deoxyHb. The magnetic inhomogeneities are dynamically averaged for all spins, since this effect is similar for all water molecules inside the vessel. Therefore, this effect is irreversible by the refocusing pulse mentioned in the previous section and, therefore, alters T_2 of the water (43).

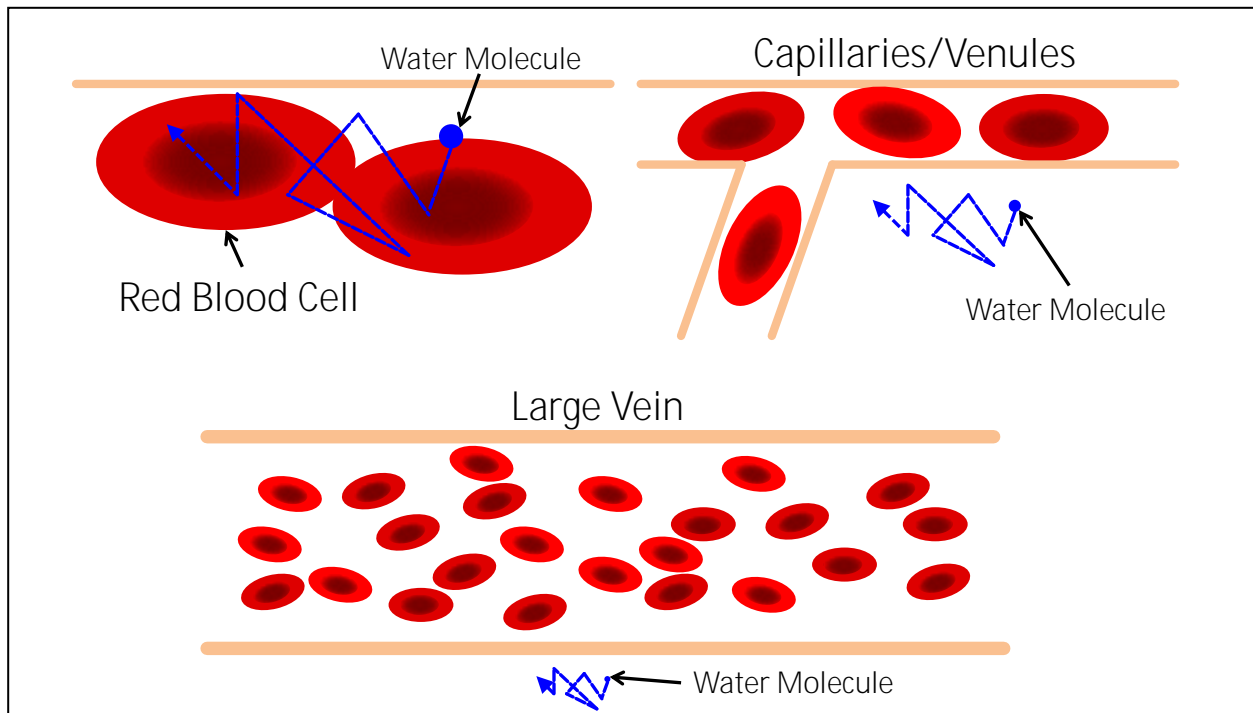


Figure 1.4 Diffusion of water molecules in the vicinity of red blood cells, capillaries/venules and large vein.

The magnetic field gradients are most significant close to the source of the large susceptibility that is red blood cells, capillaries/venules, and large blood veins. For water molecule near large veins, the diffusion lengths are comparable to the vessel diameters and thus no dynamic averaging occurs.

Since $1/T_2^*$ is the combination of reciprocal of T_2' and T_2 (equation 1.25), T_2^* of water inside the vessel also changes by the paramagnetic deoxyHb. This effect is illustrated in the upper left cartoon of the Figure 1.4. Under high magnetic fields, venous blood has a very short T_2 compared to that of tissue water due to its quadratic dependency on the external magnetic field (43). Therefore, intravascular venous blood is reduced when TE is relative long. For example, at a 9.4T magnetic field and in the feline brain, T_2^* is 29.8 ± 3.5 ms (44) for tissue and 5-7 ms for venous blood of $Y \sim 0.7$. If TE is set to 20 ms and TR is long enough to ignore T_1 weighting, signal intensity of venous blood is only 4 % compared to that of tissue water according to equation 1.26. Thus, signal from intravascular venous blood can be safely ignored (45) in my fMRI studies using 9.4T and long TE. Note that most of the conventional human fMRI are

performed at 1.5T or 3T magnetic fields where intravascular venous signal cannot be neglected (46-49). The exchange rate of water between the intravascular pool and the extravascular pool is restricted by the tight junction of the blood-brain-barrier. The typical residence time of water in the capillary is greater than 500 ms (50, 51). This is relative long compared to a typical TE used in fMRI and, thus, extravascular spins must be treated as an independent compartment. For the extravascular compartment, the magnetic field change (ΔB_{extra}) induced by deoxyHb can be expressed by equation 1.31 (38)

$$\Delta B_{\text{extra}} = \Delta\chi/2 B_0 (a/r)^2 \sin^2\theta \cos 2\phi \quad (1.31)$$

where a is the radius of the blood vessel, r is the distance from the point to the center of the blood vessel, ϕ is the azimuthal angle between the azimuth reference direction and the orthogonal projection of the r vector on the reference plane and the rest of the parameters are the same as equation 1.29. The ratio of a/r is crucial to determine ΔB_{extra} . For randomly oriented capillaries or venules, with diameters of $<10 \mu\text{m}$ or $10\text{-}60 \mu\text{m}$ (52) that is comparable to the water diffusion length ($\sim 19 \mu\text{m}$) during TE, spins experience a steep magnetic gradient before acquisition and is similar to the effect in the blood vessel. Hence, extravascular spins in the vicinity of dense capillaries and/or venules experience similar dynamic averaging of the magnetic field inhomogeneity and, thus, the T_2 of water is affected (53, 54). For veins with a diameter between 60 to $250 \mu\text{m}$ (52), which is several times larger than the water diffusion length during TE, the spins experience a smoother magnetic gradient. Thus, no dynamic averaging occurs near the vicinity of the large veins and T_2 is not affected. By separately calculating the intravascular and extravascular effects, one can see that the paramagnetic deoxyHb induced T_2 and T_2^* changes are dependent on the magnetic field and vasculature.

To calculate the BOLD signal, one also needs to consider the blood volume. From the previous section, we know that the MR signal in an imaging voxel is weighted by the volume fraction of different biological compartments. Hence, the blood volume fraction (v) is another important factor affects the BOLD signal, especially venous blood since there is no significant susceptibility difference between arterial blood and the tissue water pool. An empirical finding by Ogawa stated that R_2^* change, induced by changes in BOLD contrast, is proportional to Y and v_{venous} and can be expressed as (55)

$$\Delta R_2^* = -A[\Delta Y v_{\text{venous}} - \Delta v_{\text{venous}}(1-Y)] \quad (1.32)$$

where Δ indicates the change of that quantity between two conditions, v_{venous} is the venous blood volume fraction and A is a scaling constant. In early works, dynamic R_2^* changes have been reported during anoxic periods (56), as well as R_2 changes during graded hyperoxia in rat (57). Substituting equation 1.32 into 1.26 and ignoring the T_1 weighting term by setting a long TR, the relative BOLD signal change can be approximated as

$$\Delta S/S = A TE [\Delta Y v_{\text{venous}} - \Delta v_{\text{venous}}(1-Y)] \quad (1.33)$$

where A is the scaling factor determined from the fitted experimental data. However, the quantitative aspect of the BOLD signal change is not clear due to the influence of too many unknown parameters from the vasculature and hemodynamics. Equation 1.33 may not be sufficient to describe every condition (58) and thus many efforts have been made to calibrate BOLD signals empirically in terms of hemodynamic and vascular parameters. For example, a hypercapnia condition, which modulates CBF and CBV (27) without alternating the oxygen consumption rate (59), has been used to investigate this physiological scaling term. A multiple parameter fitting equation has been proposed as (60)

$$\frac{\Delta S}{S} = TE\alpha\beta(1-Y)^\beta \left(\frac{\Delta Y}{1-Y} v_{\text{BOLD}} - \frac{k\Delta v_{\text{BOLD}}}{\beta} \right) \quad (1.34)$$

where α and β are scaling constants, v_{BOLD} is the part of the total venous volume fraction that contributes to the BOLD signal, which is close to v_{venous} , and κ is another scaling constant defined as $\Delta v = \kappa \Delta v_{\text{BOLD}}$. If β and κ are both equal to one, then equation 1.34 is identical to 1.33. Once v_{venous} is known, Y can be estimated from equation 1.33 or 1.34. Using Fick's principle: $\text{CMRO}_2 = \text{CBF}[\text{Hb}](1-Y)$, relative CMRO_2 ($\Delta \text{CMRO}_2 / \text{CMRO}_2$) can be calculated from Y (60-64).

From the above discussion, we theoretically find that BOLD contrast is tightly coupled with both v_{venous} and ΔY . Practically, BOLD contrast is also influenced by additional physiological parameters such as change in baseline Hct (65-67), baseline Y (68) and T_1 changes induced by blood in-flow (20, 69-75). This makes quantitative comparison of the BOLD signal across subjects relatively difficult. Alternative to BOLD contrast, which uses deoxyHb as an endogenous susceptibility agent, exogenous susceptibility agents can be administered into the blood to measure the relative CBV in order to alleviate the aforementioned pitfalls. In the next section, we will discuss about the mechanism of CBV-weighted fMRI.

1.2.3 Cerebral blood volume weighted fMRI

CBV-weighted fMRI was adopted to map the functional activity of the human visual cortex using Gadolinium (Gd) chelate as the exogenous susceptibility agent before BOLD fMRI (22, 76). Gd was chelated with low molecular weight ligands due to its toxicity (77). Because the R_2^* change of the blood is linearly proportional to the concentration of the susceptibility agent, the signal intensity changes can be readily converted to the concentration time curve reflecting the passage of the agent through the volume of interest. By monitoring the MR signal intensity

before, during and after bolus injection of Gd chelate, relative CBV can be estimated from the tracer kinetics studies, as did similar PET studies (78, 79). To obtain the absolute CBV, one needs to normalize the relative CBV against voxels containing only blood. However, this normalization is difficult to achieve in practice due to the large amount of susceptibility agents in these voxels, which lead to complete loss of signal (80). Consequently, the linear relationship between R_2^* and the concentration of the agents is invalid. Nevertheless, due to limited Gd accumulation, MR dynamic measurements of the Gd chelate cannot be repeated many times within one session, which is essential for fMRI studies.

To mitigate this issue, MRI measurements of relative CBV based on the steady state of T_1 shortening agents, like Gd chelate, have been proposed (81, 82). From the previous section, we knew that brain can be treated as two compartments: intravascular and extravascular pools, due to the tight junction of the blood brain barrier. Thus, the T_1 shortening effect only occurs in the intravascular compartment. Relative CBV can be estimated by the signal intensity difference between the pre-contrast and post-contrast conditions, assuming a linear relationship between R_1 and the concentration of the agent. However, robust measurement of the relative CBV at steady state requires the intravascular contrast agent to have a longer half-life in the blood. Recently, this problem has been overcome by the introduction of an FDA approved gadofosveset trisodium (83) or Gd labeled red blood cells (84). Another problem of this method is the sensitivity. Considering that blood only occupies *ca.* 5.4 ± 2.3 % of brain tissue in cats (85), the signal change in steady-state T_1 measurements is limited to a very small blood volume fraction, which decreases the sensitivity of this method. On the other hand, from section 1.2.1, we know that the susceptibility effect extends an additional radius beyond the blood vessel. Thus, T_2^* weighted MRI is more sensitive to changes in the signal than T_1 weighted MRI. Although T_2^* weighted

MRI is desired, Gd is known to have weaker R_2^* relaxivity (change in relaxation rate per unit molar) than R_1 relaxivity, such that it's not a good candidate for use as a steady-state T_2^* shortening agent. For dynamic T_2^* weighted MRI with bolus injection, the first-pass concentration is high enough, which compensates for the low R_2^* relaxivity of the Gd chelate.

Opposite to Gd, iron is known to possess stronger R_2^* relaxivity than R_1 relaxivity, which may be a good candidate for use with steady-state T_2^* -weighted MRI. However, iron is rapidly cleared from the blood by the liver and spleen in the body. Hence, many efforts have been made to coat the iron with a bio-compatible material, such as dextran. In the early 90s, iron oxide particles, with a size of 80 - 150 nm, have been introduced for MR CBV measurement (86, 87). The half-life time in the blood for this iron particle is around 6 min, which can be extended to 81 min by shirking the particle size to 20 - 40 nm (88). Later, monocrystalline iron oxide nanoparticles (MION), with a particle size of less than 20 nm, have been synthesized and the half-life time in blood is longer than 180 min (89). MION has been adopted in many prior fMRI studies (90-94) and I also used it in my fMRI studies to investigate the relative CBV response. In the next paragraph, I will explain how to calculate relative CBV in fMRI.

Similar to endogenous iron in the deoxyHb for BOLD fMRI, the exogenous susceptibility agent, MION, induces a T_2^* change in and around the vasculature. However, MION concentration in the blood does not change by the oxygenation state of the blood, as does deoxyHb. An empirical finding of the R_2^* change induced by the changes in the quantity of any paramagnetic agent (deoxyHb or MION) can be derived (49, 76, 90, 95-97)

$$\Delta R_2^{*\text{Agent}} = A' [\text{Agent}] \Delta\chi v = A^{\text{Agent}} v \quad (1.34)$$

where A' is the scaling constant that depends on the tissue morphology, $[\text{Agent}]$ is the susceptibility agent concentration in the blood, $\Delta\chi$ is again equal to $\chi_{\text{blood}} - \chi_{\text{water}}$, v is the blood

volume, and A^{Agent} is the new scaling constant incorporating A' [Agent] $\Delta\chi$ under the steady-state condition. In equation 1.34, R_2^* and R_2 is exchangeable for most conditions (78), whereas R_2 measurement is weighted toward microvasculature when water diffusion is similar across voxels (48, 98-100). The scaling constant may vary depending on the concentration of the contrast agent, but the equation remains valid. $\Delta R_2^{*\text{Agent}}$ or $\Delta R_2^{\text{Agent}}$ is proportional to the total blood volume, or microvascular blood volume, presuming A^{Agent} does not vary by location. A map of these two quantities has been used to show the blood volume of baseline or disease models (101-104), and I also used this technique to map the baseline CBV distribution in the feline brain as shown in Figure 1.5.

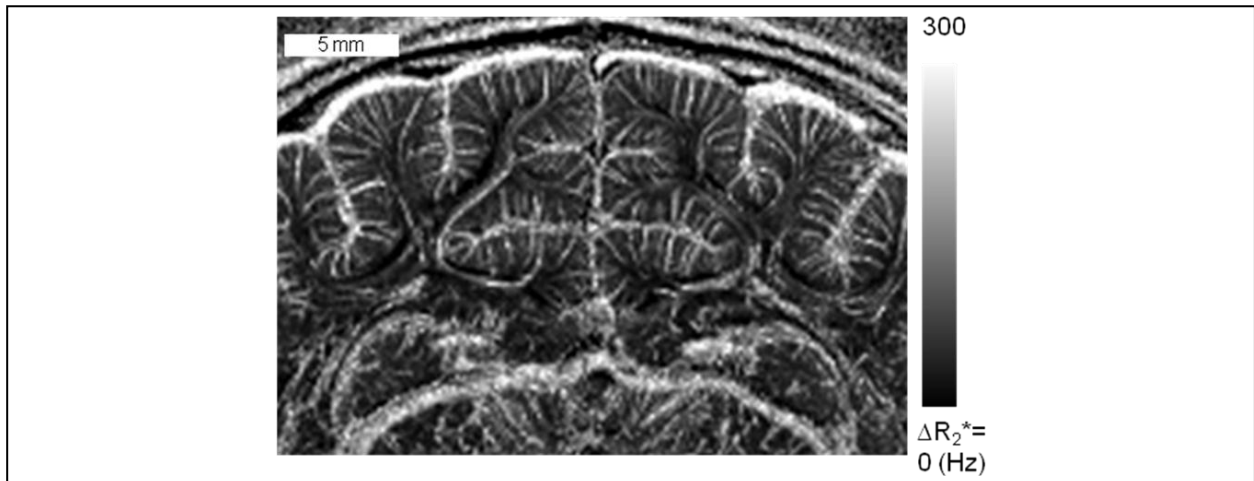


Figure 1.5 A map of change of R_2^* induced by intravascular MION in feline brain.

ΔR_2^* map, which is proportional to baseline CBV, can be calculated from the high resolution 3D gradient echo data of pre- and post- MION administration using equation 1.34. The penetrating vessels perpendicular to the cortical surface can be seen as a bright line within the cortex.

To simplify our calculation, assuming that the change in R_2^* of BOLD ($\Delta R_2^{*\text{BOLD}}$) was induced by perturbations of the hemodynamics, can be separated into blood volume contribution and deoxyhemoglobin contribution (94)

$$\Delta R_2^{*\text{BOLD}} = \Delta R_2^{*\text{CBV}} + \Delta R_2^{*\text{Hb}} = A^{\text{BOLD}} \Delta v + \Delta A^{\text{BOLD}} v \quad (1.35)$$

Equation 1.35 is very similar to equation 1.32 if $A\Delta Y$ and $-A(1-Y)$ are replaced with ΔA^{BOLD} and A^{BOLD} . The first term $\Delta R_2^{*\text{CBV}}$ and the second term $\Delta R_2^{*\text{Hb}}$ account for changes in R_2^* due to changes in blood volume and deoxyHb concentration, respectively. When an exogenous contrast agent, like MION, is administrated into blood, the second term is not affected and equation 1.35 becomes:

$$\Delta R_2^{*\text{BOLD+MION}} = (A^{\text{BOLD}} + A^{\text{MION}})\Delta v + \Delta A^{\text{BOLD}} v \quad (1.36)$$

Subtracting equation 1.36 from 1.35, we find:

$$\Delta R_2^{*\text{BOLD+MION}} - \Delta R_2^{*\text{BOLD}} = A^{\text{MION}} \Delta v \quad (1.37)$$

Equation 1.37 indicates that one can isolate the R_2^* contribution due to blood volume changes once A^{MION} is known. Instead, one can calculate the relative CBV change ($\Delta v/v$) by substituting $A^{\text{MION}} = \Delta R_2^{*\text{MION}}/v$ from equation 1.34 and we can get:

$$\Delta v/v = (\Delta R_2^{*\text{BOLD+MION}} - \Delta R_2^{*\text{BOLD}})/\Delta R_2^{*\text{MION}} \quad (1.38)$$

From equation 1.35, we can find ΔR_2^* from dividing the signal after the event by the signal before the event and then taking the natural logarithm as

$$\Delta R_2^{*\text{BOLD+MION}} = -\ln(S_{\text{PostMION_Stim}}/S_{\text{PostMION_Base}})/TE_{\text{MION}} \quad (1.39)$$

$$\Delta R_2^{*\text{BOLD}} = -\ln(S_{\text{BOLD_Stim}}/S_{\text{BOLD_Base}})/TE_{\text{BOLD}} \quad (1.40)$$

$$\Delta R_2^{*\text{MION}} = -\ln(S_{\text{PostMION_Base}}/S_{\text{PreMION_Base}})/TE_{\text{MION}} \quad (1.41)$$

where TE_{MION} and TE_{BOLD} are the TEs used in MION fMRI and BOLD fMRI studies, respectively (their optimal TEs are different (40)), $S_{\text{PostMION_Stim}}$ is the MR signal following perturbation of the hemodynamics (stimulation) and after MION administration, $S_{\text{PostMION_Base}}$ is the MR signal without perturbation of the hemodynamics (baseline) and after MION administration, $S_{\text{BOLD_Stim}}$ is the MR signal with perturbation of the hemodynamics (stimulation) and before the MION administration, $S_{\text{BOLD_Base}}$ is the MR signal without perturbation of the

hemodynamics (baseline) and before MION administration, $S_{PreMION_Stim}$ is the MR signal without perturbation of the hemodynamics (baseline) and before MION administration. S_{BOLD_Base} and $S_{PreMION_Stim}$ differ in their TE values. Substituting equation 1.39-41 into 1.38 and, after some algebraic manipulation, we can get:

$$\frac{\Delta v}{v} = \frac{\ln\left(\frac{S_{PostMION_Stim}}{S_{PostMION_Base}}\right) - \frac{TE_{MION}}{TE_{BOLD}} \ln\left(\frac{S_{BOLD_Stim}}{S_{BOLD_Base}}\right)}{\ln\left(\frac{S_{PostMION_Base}}{S_{preMION_Base}}\right)} \quad (1.42)$$

Equation 1.42 implies that BOLD contrast contributes positively to the signal change, thus neglecting this term results in under-estimating the relative CBV (98, 105). Note that the ΔR_2 may not be linearly correlated with $\Delta\chi$ of the venous blood (106) and, thus, this model may over-compensate the ΔR_2 from BOLD. CBV fMRI using an exogenous susceptibility agent has one advantage over BOLD fMRI. The susceptibility change induced by MION is many orders larger than deoxyHb and, thus, this method is much more sensitive than BOLD fMRI, especially in lower magnetic fields. This is because the BOLD contribution is supra-linearly dependent on the magnetic field (58), whereas MION induced ΔR_2^* changes are saturated at higher magnetic fields (90, 93). Although the sensitivity gained using MION as an exogenous susceptibility agent is not as high as in lower magnetic fields, the advantage of MION over BOLD still persists up to 9.4T (98, 107-109).

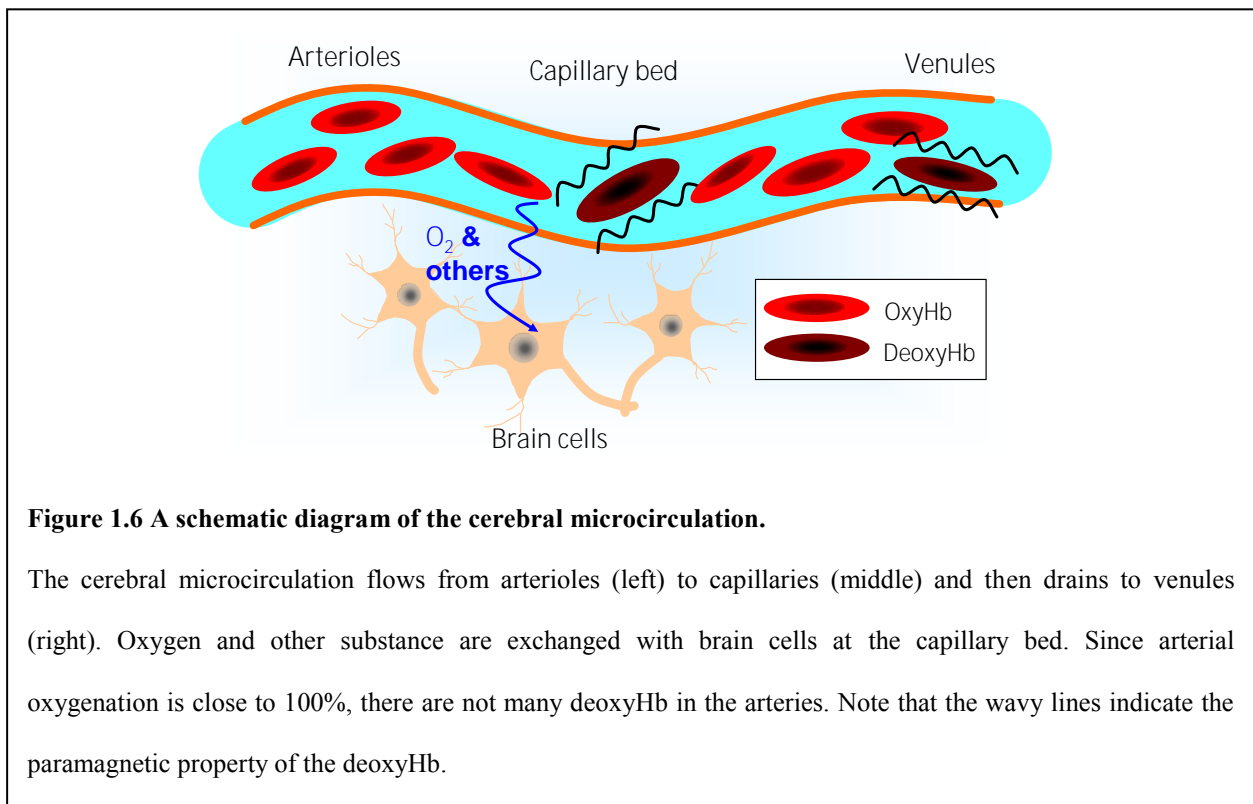
In the previous two sections, we have discussed the contrast mechanism of BOLD fMRI using deoxyHb as an endogenous susceptibility agent and CBV-weighted fMRI using an exogenous susceptibility agent. BOLD fMRI is sensitive to changes in both blood oxygenation and venous blood volume, while CBV fMRI is only sensitive to blood volume. BOLD fMRI and CBV fMRI, plus the aforementioned ^{15}O PET and OIS, all share one common characteristic by

using changes in the hemodynamics as an indicator of the underlying neural activity. However, the detailed mechanism of how neural activity evokes the hemodynamic response is still unclear. In the next section, I will discuss the basic physiology of fMRI and the current consensus about the relationship between neural activity and the evoked hemodynamic response.

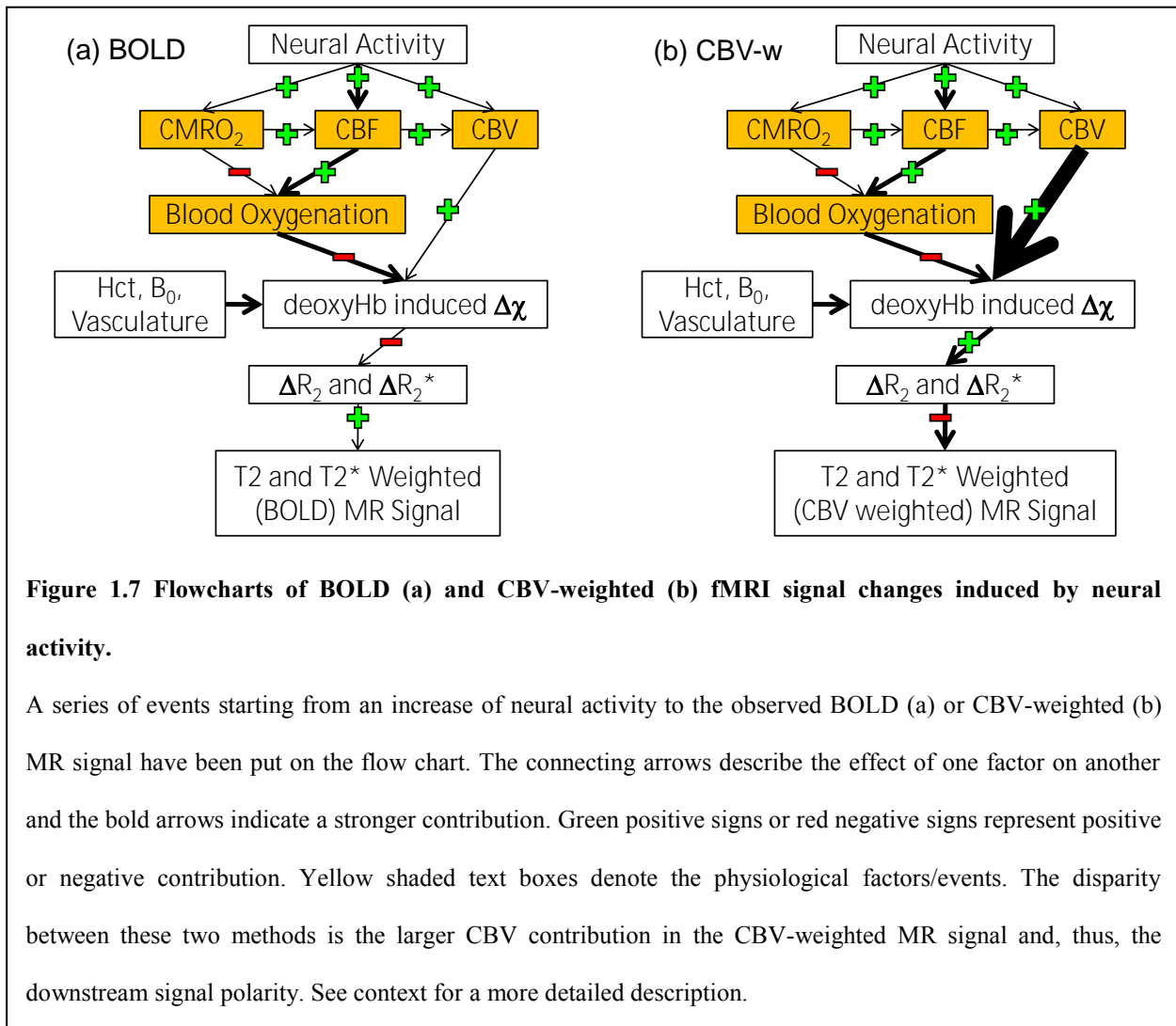
1.2.4 Neurophysiology of fMRI

A working brain requires a continuous supply of oxygen and glucose from blood vessels, because brain cells constantly relies on oxygen and glucose to generate energy and only a small reservoir of oxygen (110) and glucose (111) have been found in the brain. Brain cells, including neurons and glial cells, use glucose and oxygen as their energy source. Thus, the cerebral vasculature is tightly regulated to meet the energy demand of brain cells and this relationship is termed neurovascular coupling (112). The exact signaling pathway of neurovascular coupling is still unknown, but glial cells, especially astrocytes, are believed to involve in this pathway (113-115). What we do know from the experimental results is that increases in neural activity by sensory stimuli, psychological state changes, pharmaceutical intervention, cognitive tasks, etc. are accompanied by increases in CBF and CBV (116). Furthermore, changes in $CMRO_2$ and $CMR_{Glucose}$ have been observed despite the fact that changes in $CMR_{Glucose}$ is significantly larger than changes in $CMRO_2$ during neural stimulation (117). A working hypothesis of this mismatch, dubbed the lactate shuttle, is that lactate is produced in astrocytes by anaerobic metabolism during intense neural activity and later transported to neurons for generating energy via aerobic metabolism (118, 119). The detailed mechanism of the lactate shuttle is still unclear and a further discussion about $CMR_{Glucose}$ is beyond the scope of this thesis, since glucose does not influence the T_2 or T_2^* weighted MR signal.

To understand the connection between fMRI signals to the neurophysiology, one needs to know the cerebral microcirculation first. In Figure 1.6, a schematic diagram of the cerebral microcirculation is shown. The blood circulation uni-directionally flows from arteries to veins via the arterioles, capillaries and venules. Oxygen and other substances, like glucose, water, etc., are exchanged across the blood brain barrier to brain cells at the capillary bed. Arterial oxygenation is normally near 100% and drop to 60% at the veins.



Aforementioned neurovascular coupling events, except changes in $CMR_{Glucose}$, are illustrated in the first stage of the flow chart shown in Figure 1.7 (120-122). Besides neurovascular coupling, increases in $CMRO_2$ are known to promote CBF and CBV via nitric oxide (123, 124) and CBV is correlated with CBF through the Grubb's equation (CBV is proportional to CBF^α , where α is 0.38 for monkey (27), 0.4 for rat (125) and 0.3 for human (126)). Given blood oxygenation in the artery is near 100%, an increase in CBF means more



fully oxygenated blood is supplied to the tissue and CBF contributes positively to the blood oxygenation on the venous side (127). On the other hand, CMRO₂ contributes negatively to blood oxygenation. Hence, blood oxygenation is influence by two opposite contributions. During intense neural activity, oxygen delivery from the blood surpasses the oxygen demand, resulting in an increase of blood oxygenation (116). The increase of blood oxygenation reduces the susceptibility change induced by deoxyhemoglobin, which was detailed in section 1.2.1. In contrast, an increase in CBV elevates the quantity of endogenous deoxyHb or exogenous susceptibility agent, resulting in a susceptibility increase. The net susceptibility change is the combination of blood oxygenation, CBV and neural activity non-specific factors, such as

hematocrit, static magnetic field, and vasculature. Without administering a susceptibility agent, such as MION, the increase of CBF dominates the final ΔT_2 or ΔT_2^* and causes a T_2 or T_2^* weighted MR signal to increase as seen from the Figure 1.7a. In case of intravascular administration of MION, signal loss due to the increase of the volume fraction of MION overwhelms the contribution from the change in blood oxygenation resulting in decrease of the overall MR signal (Figure 1.7b).

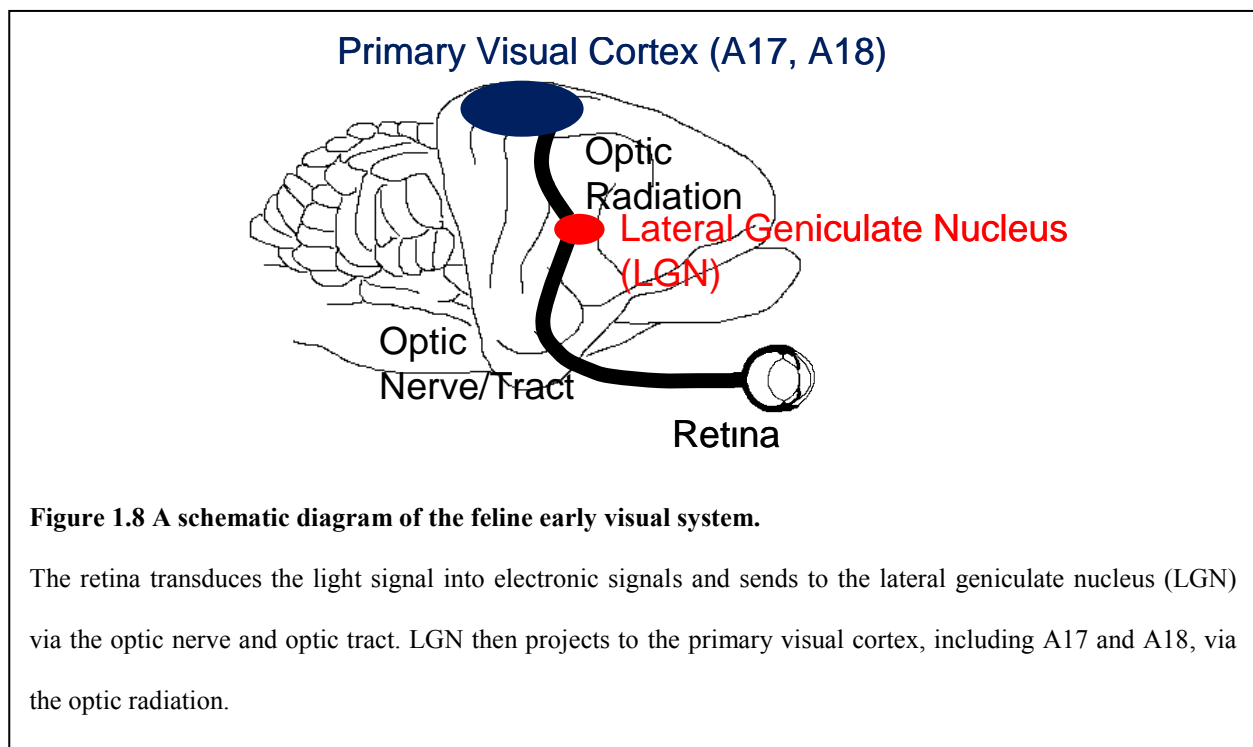
In summary, during neural stimulation evoked hyperemia, both the CBF and CBV increase results in a surplus of oxygenation delivery and an elevated Y . Next, the MR signal increases due to decreases of R_2^* , whereas the MION induced R_2^* increase outpaces the BOLD effect and leads to an MR signal decrease. Instead of measuring neural activity directly, BOLD and CBV-weighted fMRI measure the change in hemodynamics as a surrogate of the underlying neural activity. Therefore, it is crucial to understand the relationship between the fMRI signal and the underlying neural activity in order to correctly interpret the meaning of the fMRI signal. In the next two chapters, I will show results from two experiments regarding the relationship between the hemodynamic response and the underlying neural activity on a macroscopic and microscopic scale. Before that, let me briefly introduce my animal model, the feline visual system, for these fMRI studies. Both blood circulation and simple neural circuitry will be covered in the next section.

1.3 OVERVIEW OF THE EARLY VISUAL SYSTEM

In the early 1960's, Hubel and Wiesel were the first to systematically study the neurophysiology of the visual system using the microelectrode (128). They discovered that the

primary visual cortex had a columnar and laminar functional organization and provided a general framework for understanding intra-cortical processing. Since then, neurophysiology of the primary visual cortex has been extensively explored, especially in the feline model.

The early visual system consists of the neural pathway from the retina to the primary visual cortex, as shown in Figure 1.8. The first stop of the early visual pathway is the retina, which is a multi-layered structure lining the inner surface of the eye. These layers are nourished by two independent blood supplies: the retinal and choroidal circulations. The light signal is transduced to an electrical signal by the retina, which transmits to the lateral geniculate nucleus (LGN) through optic nerve and optic tract. The percent of optic nerve crossing to the contralateral side of optic tract of the cat is about 65% (129), which is closer to primate (50%) compared to other laboratory animals such as dog (75% (129)), ferret (89% (130)), rat (90% (131)). The LGN is a layered structure in the ventro-postero-lateral corner of the thalamus that receives segregated input from the two eyes for most mammals. Besides receiving inputs from



the retina, LGN also receives inputs from the superior colliculus. The superior colliculus consists of superficial layers that receive direct inputs from the retina and visual cortex, and intermediate and deep layers that receive inputs from other non-visual cortical and subcortical areas. Another notable subcortical visual structure is the pulvinar, which is the largest extrageniculate visual thalamic complex that runs along the medial edge of the LGN. However, the pulvinar is not considered part of the early visual system since it receives most of its inputs from the cortex and little from the retina (132). The LGN has two separate blood supplies: the anterior choroidal artery (a branch of the internal carotid artery), and the lateral choroidal artery (a branch of the posterior cerebral artery). The anterior choroidal artery supplies the lateral and medial parts of LGN whereas the lateral choroidal artery supplies the hilus and the mid-zone of the LGN (133). Neurons of the LGN send most of their efferents via the optic radiation to the primary visual cortex.

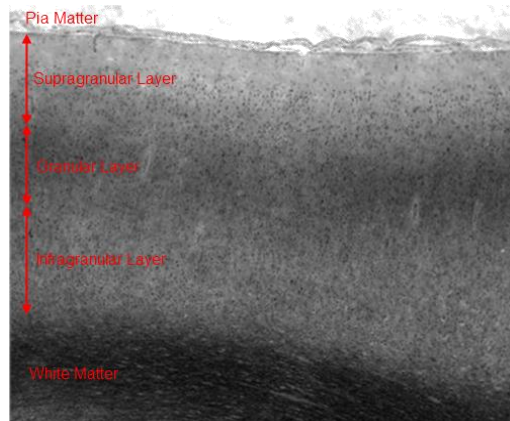


Figure 1.9 A zoomed cross section of feline cortical areal 17 stained with Luxol fast blue / Cresyl violet.

Luxol fast blue stain is used to stain myelin, which appears to be dark in this figure. Cresyl violet stain is used to stain neurons, which appear as dots scattered within the parenchyma. The total thickness of the gray matter is about 1.7 mm and is divided into six layers. Layers 2 and 3 are supragranular layers. Layer 4 is a granular layer that appears as a dark band in the middle of the gray matter. The granular layer contains a high density of myelinate axons and neuronal cells. Layers 5 and 6 are infragranular layers.

The visual cortex is the main processing unit for visual information of the central nervous system. In cats, the primary visual cortex, or A17, is roughly 1.7 mm thick and spans from the pia matter to the white matter. The laminar functional architecture of A17 can be classified into three principle layers: supragranular layer, granular layer and infragranular layer. The laminar organization has been labeled in the histology shown in Figure 1.9. The granular layer is the cytoarchitectural layer 4 and receives input from the lateral geniculate nucleus (LGN), which is the relay for visual information in the thalamus. Then, the granular layer projects to the supragranular layer. The supragranular layer consists of cytoarchitectural layers 2 and 3, which mainly project to higher cortical areas and have little projects to the infragranular layer. The infragranular layer consists of cytoarchitectural layers 5 and 6, which also receives projections from LGN. The infragranular layer then projects back to LGN and other subcortical areas like superior colliculus and pons. In addition to the hierarchical connections, neurons in each layer send collaterals to form local connections.

The blood circulation in the brain is also an important factor affecting the hemodynamic response in the cerebral cortex (114). A schematic diagram of the cerebral cortical circulation is shown in Figure 1.10. The cortex receives its blood supply through the penetrating arteries/arterioles, which branch out from the superficial pial arteries. Arteries and arterioles are equipped with an endothelial cell layer and multiple layers of smooth muscle cells, which control the diameter of these vessels. When penetrating arteries reach deeper into the brain, their basal lamina contact with the endfeet of astrocytes and these arteries turn into cerebral arterioles (134). Cerebral arterioles give rise to capillaries, where substances are exchanged with brain cells (see Figure 1.6). Capillaries are comprised of single endothelial cells with an average diameter of $5.1 \pm 0.84 \mu\text{m}$. Some capillaries are embraced by pericytes, which may function as a blood shunt

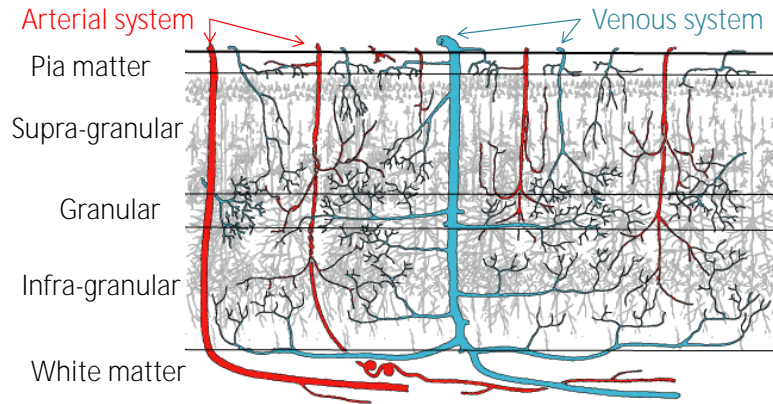


Figure 1.10 A schematic diagram of blood circulation in the human visual cortex.

Arteries branch out from the superficial arteries in the pia mater and penetrate into the parenchyma perpendicular to the cortical surface. Then, these arteries branch out into small arterioles perpendicular to the penetrating artery, which connect to the capillary bed. Blood returns to the cortical draining veins through the connected penetrating veins. Original figure from (5) and modified figure courtesy of Justin Gardner (8).

(135). The capillary density across the cortical layers is heterogeneous and correlates linearly with the $CMR_{Glucose}$ and CBF (136). Although some researchers are suspecting that the pericytes plays a key role in controlling the local hemodynamic response (137), capillaries only account for 1/3 of the cerebrovascular resistance (138), which cannot be the main determinant for the cortical hemodynamic regulation. The remaining 2/3 of the cerebral resistance is attributed to pial arteries and large arteries (138, 139) and is possibly responsible for the cortical hemodynamic regulation. After exchanging substances with brain cells at capillaries, blood is drained into venules, which are then connected to penetrating vein/venules. Eventually, the penetrating veins merge into the pial veins on the cortical surface. The above model of cortical circulation is a simplified model, which is sufficient to investigate the laminar hemodynamic response.

1.4 ORGANIZATION OF THE THESIS

In the first chapter, I have given an overview of functional neuroimaging with a focus on fMRI. I have introduced the basic MR physics and the contrast mechanism of MRI. Then, the connection of MR signal changes to the physiological parameters, like $CMRO_2$, CBV, CBF, blood oxygenation, have been elucidated. Although the exact mechanism of neurovascular coupling is still unclear, I have briefly summarized the current consensus on this issue. Finally, the feline early visual system has been outlined, concentrating on the visual cortex and blood circulation, which is relevant to later chapters.

In chapter two, I have investigated the relationship between BOLD fMRI and neural activity in the feline visual cortex by comparing the temporal frequency tuning curves of BOLD fMRI to those measured by electrophysiology in the literature. BOLD tuning curve seem to resemble the tuning curves of the low frequency band of the local field potential and, to a smaller degree, to spiking activity. Additionally, according to the spiking activity measurements, different visual areas have different preferred temporal frequencies. BOLD fMRI can measure this property, which is consistent with those found in the literature.

The laminar hemodynamic regulation has been discussed in chapter three using BOLD and MION aided CBV-weighted fMRI. According to the spiking activity measurement in the literature, the infragranular layer has a higher temporal frequency preference than the granular and supragranular layers. The temporal frequency preference of the local field potential can be predicted from the hierarchical order of the visual cortex and the infragranular and granular layers still have a higher preferred frequency compared to the infragranular layer. Surprisingly, the laminar tuning curves of BOLD and CBV-weighted fMRI do not show a significant

difference across the three layers. Therefore, hemodynamic response may not reflect the underlying neural activity in the laminar scale as promised on the areal scale.

In chapter four, I show some preliminary data acquired by my colleague, Dr. Zhao, to investigate the vascular factor of CBV weighted fMRI. A hypercapnia challenge with a regular visual stimulus was performed with MION aided CBV-weighted fMRI. The layer profiles of these two stimuli are similar and the trough is located at the same position. This implies that the functional reactivity of the cortical vasculature influences the CBV-weighted image significantly and that the hemodynamic response may not be regulated at the laminar level. In the future, to further verify my finding, optogenetic engineered animals may be used with fine control of excitation of an individual layer.

2.0 BOLD RESPONSES TO DIFFERENT TEMPORAL FREQUENCY STIMULI IN THE LATERAL GENICULATE NUCLEUS AND VISUAL CORTEX: INSIGHTS INTO THE NEURAL BASIS OF FMRI

2.1 ABSTRACT

The neural basis of the blood oxygenation level dependent (BOLD) functional magnetic resonance imaging (fMRI) remains largely unknown after decades of research. To investigate this issue, the unique property of the temporal frequency tuning that could separate neural input and output in the primary visual cortex was used as a model. During moving grating stimuli of 1, 2, 10 and 20 Hz temporal frequencies, we measured 9.4-T BOLD fMRI responses simultaneously in the primary visual cortex of area 17 (A17) and area 18 (A18), and the lateral geniculate nucleus (LGN) of isoflurane-anesthetized cat. Our results showed that preferred temporal frequencies of the BOLD responses for A17, A18 and LGN were 3.1 Hz, 4.5 Hz and 6.0 Hz, respectively, which were comparable to the previously reported electrophysiological data. Additionally, the difference of BOLD response onset time between LGN and A17 was 0.5 s, which is 18 times larger than the difference of neural activity onset time between these areas. We then compared the frequency-dependent BOLD fMRI response of A17 with tissue partial pressure of oxygen (pO_2) and electrophysiological data of the same animal model reported by Viswanathan and Freeman (Nature Neuroscience, 2007). The BOLD tuning curve resembled the

low frequency band (<12 Hz) of local field potential (LFP) tuning curve rather than spiking activity, gamma band (25-90 Hz) of LFP, and tissue pO₂ tuning curves, suggesting that the BOLD fMRI signal relates closer to low frequency LFP.

2.2 INTRODUCTION

Functional magnetic resonance imaging (fMRI) with blood oxygenation level dependent (BOLD) contrast is one of the most important noninvasive modalities to study the function of the human brain (18, 20, 140). Many neuroscientists and psychologists rely on BOLD fMRI to decode sophisticated neural processes in different brain areas. Nevertheless, the connection between the BOLD signal and the underlying neural activity is still under debate, even after decades of research (141). Without a comprehensive understanding of how the BOLD signal relates to different aspects of neural activities, BOLD fMRI cannot be correctly interpreted.

Neural activity can be broadly classified into local field potentials (LFP) and spiking activity; LFP is generally believed to represent synaptic activity including neural input (142, 143), while spiking activity represents supra-threshold neural output. It has been reported that the BOLD fMRI response is correlated with i) underlying LFP rather than spiking activity (144), ii) mostly spiking activity (145, 146), or iii) both LFP and spiking activity (147). Because spiking activity always occurs together with LFP, it is difficult to separate their contributions to the BOLD response in most circumstances. Decoupling between LFP and spiking activity, however, can be achieved by using different temporal frequency properties between thalamocortical input and cortical output (148). The thalamocortical input driven by lateral geniculate nucleus (LGN), the main visual relay nucleus located in the thalamus, has a higher temporal frequency

preference (1) than spiking activity in feline cortical area 17 (A17) and area 18 (A18) (2). Note that although feline A18 shares many similarities in neuronal and vascular properties as A17, the temporal frequency preference (tuning) of A18 is slightly higher than A17 (2). Thus, cortical input and output in primary visual cortex dissociate at high temporal frequency stimulation. Using this property, Viswanathan and Freeman (148) measured both neural activity and tissue partial pressure of oxygen (pO_2) with a polarographic oxygen sensor in feline A17, and found a change in pO_2 even in the absence of spiking activity during high temporal frequency stimulation. Assuming that the BOLD fMRI signal is analogous to pO_2 change, Viswanathan and Freeman (148) suggested that the BOLD fMRI reflects LFP. However, this inference may not be valid due to the non-linear relationship between tissue pO_2 and BOLD signal (127), and contributions of cerebral blood volume (CBV) to the BOLD signal (58). Therefore, it is important to perform BOLD fMRI during different temporal frequency stimuli for addressing neural sources of the BOLD signal.

In the present study, we obtained BOLD fMRI in feline early visual system (LGN, A17 and A18) at 9.4 T during four different temporal frequency stimulations of 1, 2, 10 and 20 Hz. The BOLD response versus temporal frequency (i.e., temporal frequency tuning curve) was determined. Then, frequency tuning curves and dynamics of BOLD fMRI in A17, A18 and LGN were compared with corresponding spiking activity data reported in the literature (1-4, 149) in order to determine the consistency between fMRI and neural activity. Finally, the BOLD tuning curve of A17 was compared to neural and pO_2 tuning curves in the same animal model reported by Viswanathan and Freeman (148) for examining the neural source of BOLD fMRI. Part of the work was presented in abstract forms (150, 151).

2.3 MATERIALS AND METHODS

2.3.1 Procedures of animal preparation

Eight adolescent cats, weighted between 1.14 and 1.68 kg, were used under an animal protocol approved by the Institutional Animal Care and Use committee at the University of Pittsburgh. Atropine sulfate (0.05 mg/kg, IM) was injected to suppress mucus secretion. The cat was then anesthetized with an intramuscular injection of a ketamine (10 – 20 mg/kg) / xylazine (0.2 mg/kg) cocktail and intubated for mechanical ventilation with a pressure-driven ventilator (24 – 28 stroke/min). Isoflurane gaseous anesthesia was maintained at 1.5% in a mixture of $N_2/O_2 = 0.7/0.3$ during surgical preparation. A cephalic intravenous catheter was placed for infusion of supplemental fluids (5% dextrose) with pancuronium bromide (0.15 – 0.2 mg/kg/hr). The pupils were dilated by 1% tropicamide ophthalmic solution and nictitating membranes were retracted by 2.5% phenylephrine hydrochloride. Contact lenses were then fitted to both eyes. The cat was placed in a custom-built cradle and restrained in normal postural position with ear and a bite bars. Rectal temperature was maintained between 37.7 and 38.3° C by a feedback-controlled water circulator. End-tidal CO_2 was monitored by a capnometer and maintained in the range of 3.4 – 3.8% by adjusting the volume and/or rate of the ventilator. Vital signs were displayed and recorded using a polygraph system (BIOPAC, Goleta, CA, USA). During functional studies, the isoflurane level was maintained at 0.9 – 1.1%. In addition to isoflurane, functional sessions were also performed under mixture of pentobarbital (1.5 mg/kg/hr) and fentanyl (10 μ g/kg/hr) in two cats to examine the influence of anesthesia on temporal frequency-dependent fMRI responses.

2.3.2 Paradigm of visual stimulation

Four temporal frequencies including 1, 2, 10 and 20 Hz of vertical sinusoid-gratings were projected on a frosted glass screen positioned 9 to 11 cm away from the cat eyes. Thus, the stimulation spanned approximately $54^\circ - 67^\circ$ in the visual field of view (θ in Figure 2.1A) for the cat. Visual stimuli were generated by a personal computer using custom Matlab script (MathWorks, Natick, MA, USA) with Psychophysics Toolbox extensions (152). The frame-dropping rate for our stimuli, reported by Psychophysics Toolbox, was less than 0.1% for all experiments. Due to the electronic property of our LCD projector (NEC Display Solutions, Itasca, IL, USA; model: MT-1055; resolution 1024×768 pixels and 60 Hz refresh rate), the peak-to-peak intensity had to be reduced to 60% of the maximum intensity such that a proper sinusoid pattern was generated for all temporal frequencies. The accuracy of the generated sinusoid pattern was examined by a fast charge-coupled device (>100 frame/s). The luminance for the crest and the trough of the sinusoid pattern was ~ 25 cd/m² and ~ 4 cd/m² as determined by a chroma meter. Each epoch of the stimulation paradigm consisted of 4-s unidirectional moving sinusoidal gratings and 20-s stationary gratings (see Figure 2.1A). The spatial frequency, defined as number of cycles of a sinusoidal grating that spans 1° of the visual angle, was fixed to 0.15 cycle/degree for all temporal frequency stimuli. A total of 32 epochs with four temporal frequencies were pseudo-randomized within each fMRI run, and ≥ 15 runs were performed.

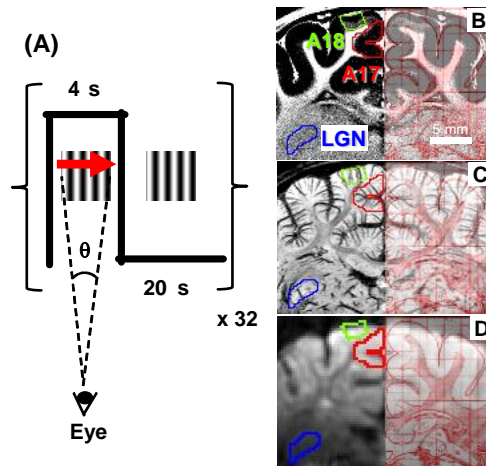


Figure 2.1 Stimulus paradigm and regions of the early visual areas.

(A) Each stimulus epoch consisted of 4-s moving sinusoidal gratings and 20-s stationary gratings. The temporal frequency of moving sinusoidal gratings (unit: cycles/sec) is defined as number of cycles of a grating passing at one visual point per 1 second, and spatial frequency (unit: cycles/deg) is defined as number of cycles of a sinusoidal grating that span 1 degree of the visual angle, θ . Since the velocity of the moving sinusoidal grating is linearly proportional to the temporal frequency when the spatial frequency is fixed, higher temporal frequency corresponds to faster movement of the sinusoidal grating. (B – D) Regions of interest (ROI) of A17 (red), A18 (green) and LGN (blue) were obtained in both hemispheres, but overlaid on T_1 -weighted (B), T_2^* -weighted (C), and baseline EPI images (D) only on the left hemisphere for display. The same ROIs were used for further data analyses, and shown in subsequent figures. The cat brain atlas (7) of a corresponding slice was overlaid on the right hemisphere of the three images (B – D). In the T_1 -weighted image (B), in which gray matter signal is almost nulled, white matter and cerebrospinal fluid (CSF) appear white. In the T_2^* weighted image (C), vein, gray matter, and white matter appear dark, white, and gray, respectively. LGN was identified in the lower lateral sub-cortex of the image surrounded by grayish optical radiation, optic nerve and dark veins in the T_2^* weighted image, and appears a little darker than the surrounding region in the T_1 -weighted image. Note that the lateral boundaries of A17 and A18 ROIs were chosen to be parallel to the penetrating veins in T_2^* weighted image. The baseline EPI image (D) shows no distortion and matches well with the atlas and conventional anatomic images.

2.3.3 Protocol of MRI acquisition

The cat was placed inside a 9.4-T/31-cm horizontal bore magnet interfaced to a Unity INOVA console (Varian, Palo Alto, CA, USA). The actively shielded 12-cm diameter gradient insert reached its maximum gradient strength of 40 Gauss/cm within 120 μ s. A custom-built butterfly-shaped surface coil with length \times width \times depth = 5 \times 3 \times 1.5 cm³ was used. This coil was etched on a flexible Teflon-printed circuit board (Rogers Corporation, Rogers, CT, USA) mounted on a half cylinder acrylic plate. Three-plane scout images were acquired for the initial positioning of the imaging slices. An automatic three-dimensional (3-D) gradient shimming routine was used to minimize the magnetic field inhomogeneity over the imaging slices, yielding a water spectral linewidth of <25 Hz. To precisely prescribe the slice position of fMRI studies, a 3-D venographic image with isotropic resolution of 78 μ m³, which delineated veins and gray matter, was obtained using a 3-D gradient-recalled echo imaging technique with flow compensation (153). To acquire anatomical reference for fMRI, myelin-enhanced T₁-weighted images were obtained using a multiple-segment inversion-recovery turbo fast low angle shot (IR-TurboFLASH) sequence with in-plane resolution of 156 μ m² (154) in the same imaging slices as fMRI. Inversion time was set to the nulling point of the gray matter at 9.4 T.

For fMRI studies, two or four adjacent coronal 2-mm-thick images covering both the primary visual cortex and LGN were acquired using a partial-Fourier gradient-recalled echo-planar imaging (GR-EPI) sequence (155) with a 4.096-ms apodized sinc RF excitation pulse. The RF power was determined as the average of the optimal RF power at the visual cortex and LGN. The imaging parameters were: field of view = 40 \times 30 mm², matrix size = 128 \times 60 (with phase-encoding overscan lines of 12) reconstructed to 128 \times 96, in-plane resolution = 313 \times 313

μm^2 , readout echo spacing = 0.4998 ms, TE = 20 ms, and TR = 1 s. To minimize Gibbs ringing artifacts, the missing 36 k-space lines were synthesized by the projection onto convex set theory (156). A data collection order of imaging slices was reversed for every other run to cancel out the timing error between slices after averaging.

2.3.4 Generation of fMRI maps

Before doing any statistical tests, a linear detrend and a Fermi high-pass temporal filter with a radius of 0.021 Hz and a width of 0.001 Hz were applied to minimize signal fluctuations induced by low frequency signal drifting (<0.021 Hz). Additionally, a Gaussian notch temporal filter with a center frequency of 0.429 ± 0.019 Hz (mean \pm SD; depending on the respiration rate of each run) and a bandwidth of 0.009 Hz was applied to reduce the breathing-related fluctuation. The frequency of the stimuli was 0.042 Hz, which was not affected by the notch filter or the Fermi high-pass filter. The first few epochs of each run were discarded because of the progression reaching a steady state condition and the potential influence of acoustic noise on the visual system via indirect projection from the auditory system (157). To determine the proper hemodynamic response function (HRF), an independent component analysis was carried out using MELODIC in FSL (FMRIB's Software Library) (158) and a single gamma HRF was determined from the time course of the first independent component. All fMRI activation maps were calculated using FEAT in FSL with cluster significance threshold of $p = 0.05$ (159). No additional spatial or temporal filtering was applied. Activation maps generated by FSL were overlaid on the baseline EPI images of each animal using MRICron (160).

2.3.5 Quantitative region of interest analysis

Time course analysis: As shown in Figure 2.1B – D, regions of interest (ROI) of A17 (red) and A18 (green) were defined on IR TurboFLASH image (Figure 2.1B), while the ROI of LGN (blue) was defined on venographic image (Figure 2.1C), but avoiding large veins, according to the cat brain atlas (7) using STIMULATE (161) and ImageJ (162) programs. For better visualization, a high-pass Gaussian spatial filter was applied to anatomical images to reduce the signal variation induced by B_1 inhomogeneity. The functional image acquired by the partial-Fourier GR-EPI sequence (Figure 2.1D) showed minimal geometric distortion near the ROIs comparing to the anatomical images using the same overlay of the cat brain atlas (7) on the right hemisphere as a visual guide. Furthermore, functional image showed good contrast and no partial Fourier acquisition induced Gibbs ringing artifact (Figure 2.1D). BOLD time courses of the three aforementioned ROIs were extracted from the raw data in each cat and then averaged across all isoflurane-anesthetized cats.

To analyze the dynamic property of fMRI responses in three visual areas, time courses were first linearly interpolated to 0.2 s temporal resolution, then the onset and peak times were determined as the point at which 10% and 90% of the maximum response was attained for each isoflurane-anesthetized cat (163). The interval of the interpolation was determined empirically. A two-tailed paired t-test was used to determine timing differences between areas.

Frequency tuning curve: Temporal frequency tuning curves were generated for each ROI. The BOLD fMRI responses were averaged from 5 to 8 s after stimulation onset for each temporal frequency, and then normalized by the maximum fMRI response of each ROI in order to minimize inter-animal variations. Then, the temporal frequency tuning curve was obtained by plotting the normalized response vs. the temporal frequency for each cat, and averaged across all

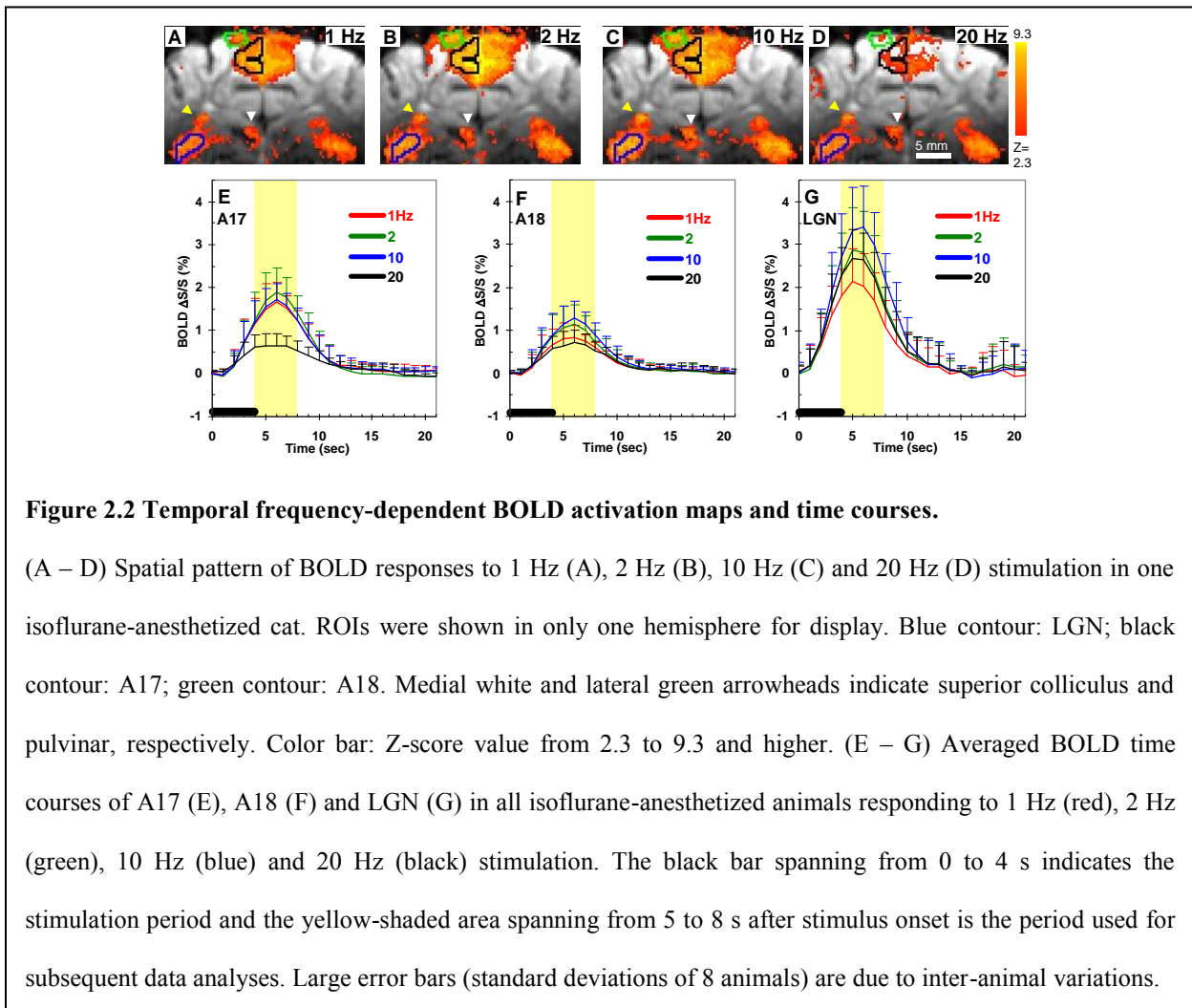
isoflurane-anesthetized cats. The preferred frequency, i.e. the temporal frequency of the maximum response, was obtained by fitting normalized BOLD responses of all eight cats vs. the logarithm of four temporal frequencies with a Gaussian distribution (3) using Ezyfit toolbox in Matlab (164). The map of preferred frequency was generated by finding the preferred frequency of each pixel. Pixels were excluded from fitting if no significant activation was found in all four temporal frequencies and were removed from display if the correlation coefficient of the fitting was lower than 0.3.

2.4 RESULTS

2.4.1 Spatiotemporal characteristics of BOLD responses for various temporal frequency stimuli

To compare spatial patterns of BOLD responses to four temporal frequency stimuli, BOLD fMRI activation maps were overlaid on the averaged baseline GR-EPI image in one isoflurane-anesthetized cat (Figure 2.2A – D). ROIs of A17 (black), A18 (green) and LGN (blue) were defined as described in the Material and methods section (see Figure 2.1B – D). Positive BOLD responses to 1 Hz (Figure 2.2A), 2 Hz (Figure 2.2B) and 10 Hz (Figure 2.2C) stimulation were mainly found in the LGN, A17 and A18 and had similar patterns with slight variations. For 20 Hz stimulation (Figure 2.2D), activation areas of A17 and A18 were smaller compared to that of lower frequencies, while the activation area of LGN was maintained for all frequencies. It should be noted that activation in the superior colliculus (white arrowhead) or pulvinar (yellow arrowhead) were not observed in all cats, thus, they were not included for further analyses.

The distinct BOLD response to various temporal frequency stimuli can be further illustrated by comparing averaged areal time courses for eight isoflurane-anesthetized cats as shown in Figure 2.2E – G. In A17 (Figure 2.2E), the BOLD fMRI response to 20 Hz stimulation is the lowest (black), while the three other temporal frequencies exhibit similar amplitudes. In A18 (Figure 2.2F), responses to 2 Hz (green) and 10 Hz (blue) have higher amplitudes than 1 Hz (red) and 20 Hz (black). In LGN (Figure 2.2G), the response to 10 Hz stimulation has the highest, while 1 Hz stimulation induces the lowest amplitude; time courses with 2 Hz and 20 Hz stimulation are almost identical. Comparing these three areas, LGN always has the highest BOLD response for all temporal frequency stimuli.



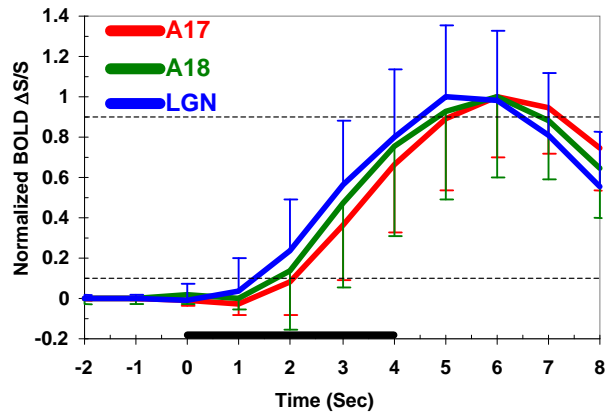


Figure 2.3 Dynamic properties of BOLD responses in the early visual areas.

Averaged, normalized BOLD time courses of A17 (red), A18 (green) and LGN (blue) in 8 isoflurane-anesthetized animals responding to 2 Hz stimulation were obtained. For clarity, only a 2-s pre-stimulus onset period and an initial 8-s post-stimulus onset period were plotted. The onset time was determined by the time to reach 10% of the peak amplitude (horizontal dashed line). Onset time of LGN response (1.8 ± 0.6 s) is significantly shorter than that of A17 (2.3 ± 0.4 s) and A18 (2.3 ± 0.7 s). The time to peak was determined by the time to reach 90% of the peak amplitude (horizontal dashed line). Peak time of LGN (4.6 ± 0.8 s) is significantly shorter than that of A17 (5.4 ± 0.6 s) and A18 (5.1 ± 1.0 s). Error bars = SD of 8 animals.

To examine the dynamic response of the BOLD signal in the early visual system, normalized BOLD time courses of A17, A18 and LGN were obtained for 2 Hz stimulation (Figure 2.3). The dynamic property of the BOLD response induced by 2 Hz was similar to that of 1 and 10 Hz, while the 20 Hz time course was not analyzed for temporal characteristics due to its small amplitude in A17 and A18. The BOLD response of LGN increased earlier and reached the peak earlier than A17 and A18. The onset time of A17, A18 and LGN (horizontal line at $y = 0.9$ in Figure 2.3) was 2.3 ± 0.4 , 2.3 ± 0.7 and 1.8 ± 0.6 s (mean \pm SD, $n = 8$ isoflurane-anesthetized cats), respectively. The onset time of LGN was significantly earlier than both A17 ($p = 0.022$, same or earlier in 8 out of 8 cats) and A18 ($p = 0.034$, same or earlier in 7 out of 8 cats); the onset time of A17 and A18 was not significantly different ($p=0.84$). The peak time of A17, A18

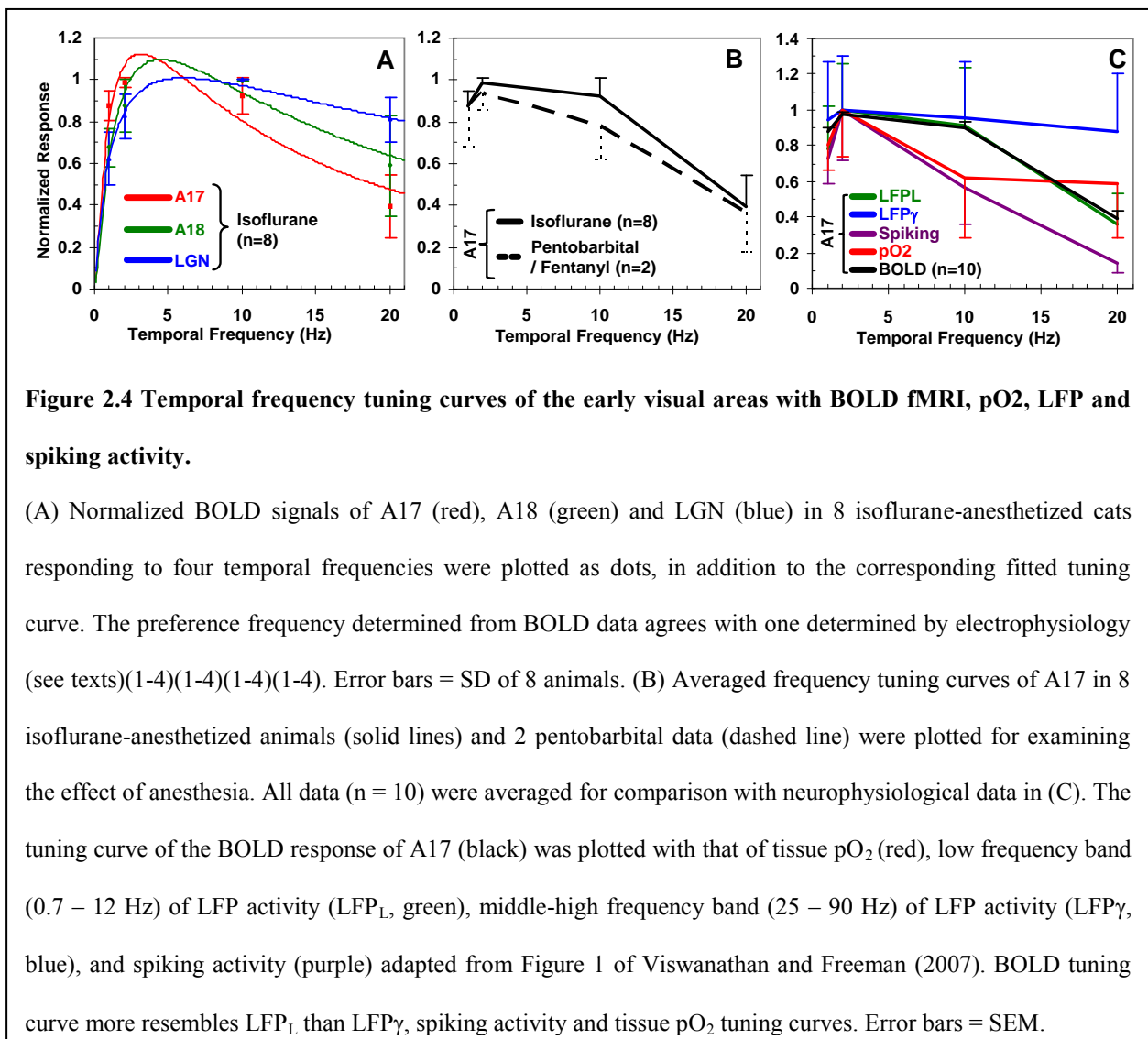
and LGN (horizontal line at $y = 0.1$ in Figure 2.3) was 5.4 ± 0.6 , 5.1 ± 1.0 and 4.6 ± 0.8 s (mean \pm SD), respectively. The peak time of LGN was significantly earlier than A17 ($p = 0.0047$, same or earlier in 8 out of 8 cats); the peak time between A17 / A18 ($p=0.28$) and A18 / LGN ($p=0.14$) were not significantly different. Generally, the BOLD response of LGN started 0.5 s earlier and peaked 0.8 s earlier than A17.

2.4.2 BOLD temporal frequency tuning curve and preference maps

To better visualize the difference in temporal frequency preference among A17, A18 and LGN of the isoflurane-anesthetized cats, normalized responses of four temporal frequencies and fitted temporal frequency tuning curves (see Material and methods) are shown in A. The Pearson's correlation coefficients (R) of the fitted Gaussian curves to the normalized BOLD responses for A17, A18 and LGN of eight cats were 0.86, 0.72 and 0.77, respectively. The preferred frequency of the tuning curve was 3.1 Hz for A17 (red), 4.5 Hz for A18 (green) and 6.0 Hz for LGN (blue). The bandwidth (full width at half maximum) of the tuning curve was 16 Hz for A17, 24 Hz for A18 and 52 Hz for LGN. Hence, A17 showed a lower preferred frequency and a narrower tuning bandwidth followed by A18 and LGN.

To determine the effect of anesthetics on the BOLD tuning curves and to compare the previously reported data obtained under sodium thiopental and fentanyl cocktail (148), we also determined and plotted average BOLD tuning curve of A17 in two animals under pentobarbital / fentanyl anesthesia (dashed line in Figure 2.4B). Pentobarbital was used as an alternative to sodium thiopental, because sodium thiopental was discontinued by its manufacturer in the United States. Both thiopental and pentobarbital are short-acting barbiturate anesthetics that act on the GABA_A receptor and pentobarbital is the main metabolite of sodium thiopental (165). Thus, the

effect of pentobarbital on neural activity should be very similar to that of sodium thiopental. We observed that the BOLD preferred frequency (3.1 vs. 2.6 Hz) and tuning bandwidth (16 vs. 16 Hz) were similar between isoflurane and pentobarbital/fentanyl. The general trend of BOLD tuning curves was also similar ($R = 0.97$, p -value of two-tailed t -test = 0.03), regardless of anesthesia. Thus, we averaged all data including 8 isoflurane- and 2 pentobarbital/fentanyl-anesthetized studies for the comparison with previously reported neurophysiological data.



To examine the neural basis of fMRI, an A17 temporal frequency tuning curve of tissue pO_2 , low frequency band of LFP (LFP_L : 0.7 – 12 Hz), gamma band of LFP (LFP_γ : 25 – 90 Hz) and spiking activity were adapted from data of Viswanathan and Freeman (148) and plotted together with the BOLD tuning curve of A17 in Figure 2.4C. Because the tuning curves of all low frequency bands of LFP, including LFP_δ (0.7 – 4 Hz), LFP_θ (4 – 8 Hz), and LFP_α (8 – 12 Hz), are almost indistinguishable, we considered all these low frequency components as one low frequency band and averaged them under the name LFP_L . The correlation coefficients and their corresponding p-value (two-tailed t-distribution) of BOLD tuning curve to LFP_L , LFP_γ , spiking activity and tissue pO_2 tuning curves were calculated: 0.98 (p=0.017), 0.95 (p=0.050), 0.92 (p=0.078) and 0.69 (p=0.31), respectively. Despite the small sampling size of 4, p-values give us a rough idea about the resemblance between these tuning curves. The BOLD tuning curve bears more resemblance to the LFP_L tuning curve compared to LFP_γ , spiking activity and tissue pO_2 tuning curves. The ratio between the response of 20 vs.10 Hz stimuli for LFP_L , LFP_γ , spiking activity and tissue pO_2 were 0.49, 0.92, 0.25 and 0.94, respectively, while that of BOLD fMRI response was 0.44. This ratio again indicates that BOLD fMRI relates closer to LFP_L than LFP_γ , spiking activity and tissue pO_2 .

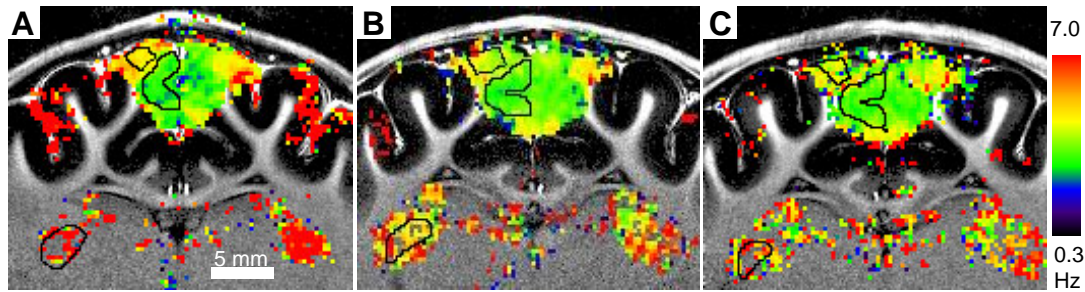


Figure 2.5 Temporal frequency preference maps with BOLD fMRI.

(A) and (B,C) are maps from two different animals whereas (B) and (C) are from the same animal in two different sessions. Color bar: preferred temporal frequency from 0.3 Hz (black) to 7 Hz and above (red). Black contours: A17, A18 and LGN. The preference maps of both animals show similar distribution of the preferred temporal frequency. The temporal frequency preference within our cortical ROIs (A17 and A18) is homogeneous indicating minimal sampling bias. Note that the peripheral visual field (lower edge of A17) shows higher temporal frequency preference.

The preferred frequency can be used for differentiating A17 and A18. Figure 2.5 shows preferred frequency maps of two representative cats where Figure 2.5B and Figure 2.5C are from the same cat in two different sessions. The similarity between Figure 2.5B and Figure 2.5C indicates that the temporal frequency preference map is reproducible across sessions. In A17 and A18 of both cats, the preferred frequency was around 3 – 4 Hz and 4 – 5 Hz, respectively. Within each cortical area, the distribution of the preferred frequency appears to be homogeneous from the cortical surface to the white matter, especially in A17. Due to limited number of frequencies, a preferred frequency cannot be robustly detected when the bandwidth of the tuning curve is large like LGN. Thus, the preferred frequency map in LGN looks inhomogeneous and discrete due to the inaccuracy of fitted values, exclusion of unreliable fittings, and contamination of large veins and white matter. At the ventral area outside of the A17 ROI, which represents a peripheral visual field, the preferred frequency appeared to be slightly higher than the majority of A17. The

shifting was less obvious for A18 and might not be detectable in the current experimental protocol.

2.5 DISCUSSION

2.5.1 Preferred temporal frequency in early visual systems

Temporal frequency is a fundamental visual feature. Detecting the regional temporal frequency preference in the visual system is an important step toward understanding and modeling the processing of visual information in the brain (166, 167). Furthermore, an impairment of the motion perception reflected in abnormal temporal frequency tuning properties may potentially serve for early detection of Alzheimer's disease or glaucoma (168). To distinguish fine changes in temporal frequency preferences, many temporal frequencies with a wide range should be used. However, only four temporal frequencies within 1 – 20 Hz range were used to obtain sufficient temporal SNR in our fMRI studies. In addition, we used a 2-mm slice thickness to obtain sufficient SNR resulting in partial volume effects that might influence the magnitude of the BOLD response. In cortical area, the boundaries of gray matter, white matter and CSF are consistent over 2 mm, i.e. voxels containing non-gray matter are minimal within A17 and A18 ROIs as examined with 3-D venogram (slice thickness = 117 μm , data not shown). On the other hand, we are aware that the LGN ROI may have a significant number of voxels containing white matter or vessels (150), because feline LGN is irregular in the caudal to rostral direction. However, the preferred frequency obtained from the BOLD response is still

valid because the partial volume effect will change the BOLD magnitude similarly for all temporal frequency stimuli.

The cat primary visual cortex consists of cytoarchitectural subdivisions: A17 and A18. Although feline A17 and A18 conventionally relate to the primate V1 and V2, hierarchical processing in A17 and A18 is ambiguous in the cat and many other phylogenetically lower mammals compared to primate. For example, electrophysiological studies suggest that A17 and A18 contribute in complementary ways to visual processing of motion signals, such that A17 and A18 are responsible for encoding low and high temporal frequencies, respectively (169). Our temporal frequency tuning properties of BOLD responses in A17 and A18 may as well satisfy this notion. The preferred temporal frequency of A17 measured by BOLD fMRI (3.1 Hz) is comparable to that determined by electrophysiology (~ 3.8 Hz (3) and ~ 2.6 Hz (4)), despite of the BOLD tuning curve of A17 having a wider bandwidth (16 Hz) than that of spiking activity (2.73 Hz) (149). Similarly, the preferred temporal frequency of A18 with BOLD fMRI (4.5 Hz) is consistent with electrophysiological findings (3 – 10 Hz) (2). Despite the clear difference between A17 and A18 optimal temporal frequency, their tuning curves are largely overlapped.

LGN is a thalamic relay nucleus located between the retina and the primary visual cortex. LGN not only conveys retinal information to the cortex, but also receives feedback information from the cortex and other subcortical areas such as the superior colliculus. This is important for visual perception because LGN can influence the amount and nature of information relayed to the cortex (170). This dynamic control mechanism of LGN, if not suppressed by anesthesia, is one of the neural substrates of the visual attention (170). The preferred frequency of LGN measured by BOLD fMRI (6.0 Hz) falls within the range determined by electrophysiology (4 Hz – 11 Hz) (1). As seen in neural and BOLD responses, LGN is less selective to temporal

frequencies of stimuli and can process relatively faster movements because of its higher tuning preference and broader tuning bandwidth. While cortical neurons fail to respond to high temporal frequency stimuli, LGN neurons respond well to such stimuli. The reason for this behavior still remains unknown (171).

There are a few temporal frequency-dependent BOLD fMRI studies in animal visual cortex with diffuse flashing light instead of moving gratings (172-174). Note that the diffuse light source has no spatial pattern (spatial frequency = 0 cycle/degree), which evokes less cortical neural activity compared to moving grating stimulus (175). Zhang et al. (174) varied the inter-stimulus interval (ISI) of flashing light-emitting diodes for their fMRI studies in cats, which could be considered as changing temporal frequency without the directional information. However, the stimulus duration was not fixed while varying the ISI in their cat studies; thus, it is difficult to compare their results to our findings. Van Camp et al. (173) and Pawela et al. (172) varied the flickering frequency of their diffuse light source with fixed stimulus duration in rats, but did not report frequency tuning properties. It would be interesting, if this information was available, to investigate the difference of tuning properties between cats and rats.

To examine the spatial distribution of the preferred frequency in the early visual system, the preferred frequency was determined on a voxel-by-voxel basis (Figure 2.5A – C). In cortical areas, the preferred frequency is homogeneous within the ROI suggesting that our ROI-based analysis is not prone to sampling bias seen in most of the point-by-point electrophysiological recording techniques. At peripheral visual fields, there is an increment of temporal frequency preference that is not startling since the preferred temporal frequency increases abruptly at the peripheral visual field according to electrophysiological measurements (176). Note that the A17 ROI excluded these areas responsible for the peripheral vision. The shift of temporal frequency

preference with retinal eccentricity may be better determined if a middle sagittal plane is used. In A18, the shift of temporal frequency preference between central and peripheral visual fields was not detectable in our BOLD fMRI studies, because this frequency shift was too small, as reported by electrophysiological recordings (176), to be detected by our stimulus paradigm.

Previously, several attempts have been made to map the temporal frequency preference in the visual cortex. Optical intrinsic signal (OIS) has been used to map the temporal frequency preference in monkeys (177) and cats (178). Our result agrees with their findings that no significant difference in temporal frequency was observed across A17 except in the peripheral visual field. However, Sun et al. (179) reported using fMRI that low and high temporal frequency domains were clustered separately in human visual cortex, which is inconsistent with our fMRI and OIS measurements (177, 178). The discrepancy may arise from the use of anesthesia in animal models or difference in species.

2.5.2 Dynamic property of visual evoked response in early visual system

We observed a faster onset of LGN BOLD response compared to the cortical response. Does this BOLD onset difference reflect the sequence of neural events? Electrophysiological measurements from the literature showed that the mean neural latency (95% confidence intervals in parenthesis) to LGN and A17 are 76 (70.2 – 82.2) and 104 (98.7 – 109.6) ms (180). Since A17 are innervated by LGN directly, the neural onset time difference between LGN and A17 can be estimated by subtracting the latency of LGN from that of A17, which is about 28 ms. This timing difference is 18 times smaller than the onset time difference (500 ms) measured by BOLD fMRI. Hence, the difference of BOLD onset time between A17 and LGN cannot be interpreted simply as difference of neural activity onset time between these two areas. The sluggish BOLD response

in A17 may attribute to different vascular reactivity (181) and/or neurovascular coupling (182) in these two areas.

2.5.3 Relationships between BOLD, tissue pO₂

We have observed unexpected dissimilarity between our BOLD tuning and tissue pO₂ tuning curve measured by Viswanathan and Freeman (148) especially at higher temporal frequency. The normalized BOLD response is 69% of the tissue pO₂ change at 20 Hz stimulation (Figure 2.4C) and is even smaller at 30 Hz when linearly extrapolate both tuning curves. This discrepancy may be explained by a few possibilities as described below.

Firstly, the discrepancy may stem from difference between pO₂ and oxygen saturation level. It is often assumed that the change in tissue pO₂ is analogous to the BOLD response (148). Tissue pO₂ is determined by the oxygen diffusion gradient to the blood pO₂, while the venous oxygen saturation level (S_vO₂) is related to the BOLD signal (58). Thus, the crucial link is whether blood pO₂ is linearly correlated with S_vO₂. This relationship is described by the Hill equation of the oxygen dissociation curve with P₅₀ = 36.8 mmHg and n = 3.207 in cats (6), with $S_vO_2/(1-S_vO_2) = (pO_2/P_{50})^n$. To investigate the relationship between blood pO₂ and S_vO₂, we assume tissue pO₂ is similar to blood pO₂ in microvessels. Since Viswanathan and Freeman (148) only provided a relative pO₂ change of ~10% for a 2 Hz stimulus and ~6% for a 30 Hz stimulus, baseline tissue pO₂ in cats has to be taken from the literature. If the baseline tissue pO₂ is about 38.1 mmHg (183), then the tissue pO₂ change of 10% and 6% corresponds to 3.8 mmHg and 2.3 mmHg, respectively. At this condition, the S_vO₂ change is approximately linear to tissue pO₂. This corroborates with the argument that tissue pO₂ change is linearly correlated with the BOLD response. However, if the baseline tissue pO₂ is 12.8 mmHg (184), a change in pO₂ will

be amplified more than the linear change in S_vO_2 in the supra-linear regime of the oxygen dissociation curve. When the S_vO_2 change is determined from 1.3 mmHg (10% of baseline pO_2) and 0.77 mmHg (6% of baseline tissue pO_2), for 2 and 30 Hz stimulations, then the relative change in S_vO_2 between the low frequency and high frequency responses is about 96% of the relative tissue pO_2 change. Thus, tissue pO_2 may no longer correlate linearly with the BOLD response. However, this non-linearity alone cannot explain the large difference (~69%) between the BOLD response and the tissue pO_2 change.

Secondly, the discrepancy may arise from CBV contribution to the BOLD signal. CBV is known to play an important role in the BOLD signal (58). If the CBV tuning curve is dramatically different from the tissue pO_2 tuning curve, then the BOLD tuning curve may diverge from the corresponding tissue pO_2 and CBV responses. However, this is unlikely to be the case, because our preliminary data indicates that the BOLD and CBV temporal frequency tuning curves are almost identical.

Thirdly, the discrepancy may be derived from the difference of anesthetics used. Both isoflurane (185) and barbiturate (186) dilate cerebral vessels and increase baseline cerebral blood flow. Cerebral blood flow, cerebral metabolic rate oxygen, mean arterial pressure and oxygen delivery are similar between these two anesthetics except that the cerebral vascular resistance is lower under isoflurane in human subjects (187). Most importantly, our preliminary results (Figure 2.4B) showed that the BOLD tuning curves under pentobarbital / fentanyl and isoflurane were similar. Therefore, we do not think different anesthetics are the primary cause of the observed discrepancy between pO_2 and BOLD tuning curves.

Finally, point-by-point measurements of the tissue pO_2 which is sampled by oxygen sensors with areal sensitivity of $200 \mu m^2$ (148) are prone to sampling bias if the number of

sampling points are limited, since tissue pO_2 is heavily influenced by the surrounding vasculature and the distance to the vessels (183). Thus, pO_2 data obtained from a limited number of single-point measurements may differ from large volume data of fMRI. In summary, the interpretation of pO_2 measurement should be cautious when it is used as a BOLD analog.

2.5.4 Relationships between BOLD and neural activity

To address the neural source of the BOLD signal, we compared the frequency tuning curve of BOLD signal with that of the known neural activity components (Figure 2.4C). Based on the correlation coefficient between these tuning curves, the trend of the BOLD tuning curve exhibits better resemblance to the LFP_L tuning curve than LFP_γ and spiking activity. Our result agrees with the findings of Maier et al. (188) that BOLD correlates better with low frequency band of LFP (5 – 30 Hz) than spiking activity in the monkey's primary visual cortex during perceptual tasks. Our data also agrees with studies in human visual cortex, which show that the BOLD signal is better correlated with the low frequency band (below 40 Hz) of LFP using electroencephalography (189). Furthermore, Martuzzi et al. (190) reported significant resemblance between the BOLD response and the low frequency band (< 14 Hz) of LFP in human visual cortex using electroencephalography. However, they also reported the similarity between BOLD and gamma band (44 – 78 Hz) of LFP which corroborates with the finding in monkey visual cortex from Logothetis et al. (144), but it disagrees with the result from Muthukumaraswamy and Singh (191) that BOLD signal does not closely correlate with gamma band of LFP (40 – 60 Hz) using magnetoencephalography. Although our result shows more resemblance of the BOLD tuning curve to LFP_L tuning curve, it does not rule out the potential roles of LFP_γ and spiking activity in the basis of the BOLD fMRI. Our results shed insight into

the complicated neural basis of the BOLD fMRI by providing evidences about closer relationship between BOLD response and LFP_L rather than LFP_γ or spiking activity.

2.5.5 Conclusion

We have successfully obtained the temporal frequency tuning curves of the early visual system in anesthetized cats using fMRI. In agreement with previous electrophysiological findings, BOLD fMRI was able to detect the subtle differences in the preferred temporal frequencies in A17, A18 and LGN. This implies that BOLD fMRI can show not only the location of the activation, but also the tuning property of the underlying neurons. We have also demonstrated that the BOLD signal of LGN increased earlier than that of A17 and A18 as known in the sequence of neural events. This hemodynamic onset time difference, however, is far larger than the neural onset time difference between LGN and A17/A18. Finally, we have demonstrated an apparent discrepancy between tuning curves of BOLD and tissue pO_2 responses, suggesting that tissue pO_2 measured point-by-point cannot simply represent the BOLD signal. Furthermore, the BOLD tuning curve was more similar to the low frequency band (< 12 Hz) of LFP than the gamma band of LFP and spiking activity, indicating that cautious should be taken when interpret BOLD response as sole indicator of different aspect of the neural activity.

2.5.6 Acknowledgments

This work was supported by NIH grants EB003324, EB003375, and NS44589. We thank Ping Wang and Michelle Tasker for animal preparation, Kristy Hendrich for 9.4 T supports, Alberto Vazquez for calibrating high temporal frequency stimulation, and Alexander Poplawsky

for editing. We are also grateful to Tao Jin, Alberto Vazquez, Kristy Hendrich and Alexander Poplawsky for helpful discussions.

3.0 SOURCE OF CORTICAL LAYER-DEPENDENT HEMODYNAMIC RESPONSE STUDIED BY VISUAL STIMULUS OF TEMPORAL FREQUENCY

3.1 ABSTRACT

Cognitive and developmental neuroscientists have been interested in cortical laminar neural response for decades. However, challenges have been posed to study the laminar neural activity noninvasively because the spatiotemporal resolution requirement for studying laminar neural activity is relatively high. Prior high resolution fMRI studies in visual cortex have shown that cerebral blood volume (CBV) weighted response, comparing to BOLD response, is more specific to the cortical layer with the highest neural activity. Thus, contrast agent aided CBV-weighted fMRI may potentially provide a minimum-invasive method to probe the laminar neural activity suitable for longitudinal studies. However, regional hemodynamic responses including CBV response are heavily influenced by the functional reactivity of the local vasculature. Since local vasculature is quite different across cortical layers, the observed layer-dependent hemodynamic response may be affected by the functional reactivity in the local vasculature instead of underlying neural response. Thus, to test whether layer-dependent hemodynamic response represents the laminar neural response, we performed BOLD and CBV-weighted fMRI during various temporal frequencies of the visual stimuli to modulate the cortical laminar neural activity. The response function (temporal frequency tuning curve) of three layers are similar to

one another for both BOLD and CBV fMRI. The fitted peak temporal frequency (preferred frequency) of three layers are between 2.99 to 3.16 Hz for BOLD fMRI and 2.74 to 2.98 Hz for CBV-weighted fMRI which are close to one another within the error range. This result is rather unexpected because the preferred frequency of infragranular layer is higher than the other two layers according to the spiking activity measurement from the literature. Besides, the synaptic activity, predicted by the hierarchical order of mammalian visual system, shows higher preferred frequency in infragranular layer and granular layer than that of supragranular layer. Therefore, hemodynamic response may not reflect the underlying neural activity in the cortical layer scale. This implicates that the layer-dependent hemodynamic response may represent the layer-dependent functional vascular reactivity.

3.2 INTRODUCTION

Neuroscientists have been interested in cortical laminar neural response for decades in an attempt to better understand inter-laminar sensory processing (192) and development of the cerebral cortex (193). If hemodynamic responses are sensitive to underlying changes in neural activity, these laminar neural responses may be noninvasively probed by hemodynamic-based functional magnetic resonance imaging (fMRI) techniques such as blood oxygenation level dependent (BOLD) fMRI (18, 20, 21) or contrast agent aided cerebral blood volume (CBV) fMRI (90, 91). Hemodynamic-based fMRI is currently one of the most widely available noninvasive functional neuroimaging modalities with reasonably spatiotemporal resolution.

Conventional gradient-echo (GE) BOLD response has been shown to be localized to the layer with the highest neural activity in rat olfactory bulb with iso-amyl acetate stimulus (194)

and monkey visual cortex with directional visual stimulus (195). In contrast, most of the fMRI researchers found that the superficial cortical layer has higher GE BOLD signal change than the middle cortical layer with the highest neural activity due to signal contributions of the pial draining veins. This problem can be alleviated by spin-echo (SE) pulse sequence by minimizing the signal contributions around large veins (44, 45, 196). On the other hand, monocrySTALLINE iron oxide nanoparticles (MION) (89) aided CBV-weighted fMRI has been shown to have higher specificity to the highest neural activity layer (98, 197-199). In addition, arterial CBV(200), cerebral blood flow (201), and post-stimulus BOLD undershot (202) fMRI have been reported to have higher laminar specificity than regular BOLD fMRI. Under most stimulus conditions, the middle cortical layer has the highest neural response, thus the localization of highest fMRI response to the middle layer can provide a mean to evaluate the spatial specificity of the fMRI response. However, regional hemodynamic response including CBV response is heavily influenced by the functional reactivity of the local vasculature (203) which has layer-dependent distribution (204, 205). Hence, the observed layer-dependent hemodynamic response may be biased toward functional reactivity of the local vasculature and may not represent the underlying neural activity.

To address this issue, we performed BOLD and CBV-weighted fMRI with various temporal frequency visual stimuli to modulate the laminar-specific neural response. Neural responses (as assessed by spiking activity) to temporal frequency of visual stimuli have been shown to peak at ~3.5 Hz in the supragranular layer (upper-most of the three principal cortical layers), ~3.1 Hz in the granular (middle) layer and ~6.0 Hz in the infragranular (bottom) layer of the cat (206). Infragranular layer has the highest temporal frequency preference (frequency at peak) of the three layers. Thus, if the hemodynamic responses are specific to these layer-

dependent neural activity changes, then fMRI signals are expected to follow the same trend as neural activity. To better visualize the trend of the temporal frequency preference, the fMRI response versus stimulus temporal frequency (temporal frequency tuning curve) can be generated. In the present study, four temporal frequencies, 1 Hz, 2 Hz, 10 Hz and 20 Hz, were selected to map the temporal frequency preference in the early visual system. Series of laminar BOLD and CBV-weighted fMRI were performed to study the layer-dependent hemodynamic response in cat primary visual cortex. To differentiate the three cortical layers, high spatial resolution myelin-enhanced (T_1 weighted) and microvascular-sensitive (T_2 weighted) anatomical images were acquired at the same position as functional studies. When the temporal frequency tuning curves of BOLD and relative CBV response were compared across three layers, we found these laminar tuning curves were very similar to each other which did not reflect the change of underlying neural response. We found that cortical layer-dependent hemodynamic response is probably independent of underlying neural activity.

3.3 MATERIALS AND METHODS

3.3.1 Animal preparation

Seven adolescent cats weighted between 1.32 and 1.86 kg were used for temporal frequency visual stimuli experiments with BOLD and CBV-weighted fMRI under an animal protocol approved by the Institutional Animal Care and Use committee at the University of Pittsburgh. Detail procedures of animal preparation have been described previously (98). Briefly, the cat was mechanically ventilates and maintained under 1.0 – 1.1% of isoflurane in a mixture

of $N_2/O_2 = 0.7/0.3$. A femoral artery was cannulated for monitoring arterial blood pressure while a femoral vein was cannulated for infusion of supplemental fluids (5% dextrose) with pancuronium bromide (0.15 – 0.2 mg/kg/hr). For CBV-weighted fMRI, a bolus of 10 – 15 mg/kg of MION (Massachusetts General Hospital, Boston, MA, USA) was administered intravenously along with ~1.5 ml/kg 10% dextran-40 solution. Additional 10 mg/kg of MION might be administered depending on the animal condition three hours after first MION injection.

3.3.2 Visual stimulation

Four temporal frequencies including 1 Hz, 2 Hz, 10 Hz and 20 Hz of vertical sinusoid-gratings were projected on a frosted glass screen 9 – 11 cm away from the cat eyes using a video projector (NEC Display Solutions, Itasca, IL, USA; model: MT-1055). The contrast and luminance of the binocular full-field visual stimuli were 72% and 25 cd/m², and the spatial frequency was 0.15 cycle/degree for all temporal frequency stimuli. Visual stimuli were generated by a personal computer using custom-written Matlab script (MathWorks, Natick, MA, USA) with Psychophysics Toolbox extensions (152). Each epoch of the stimulation paradigm consisted of 24-s unidirectional moving sinusoidal gratings and 48-s stationary gratings. Total 16 epochs with four temporal frequencies were pseudo-randomized within each run. 7 – 9 runs of BOLD fMRI and 8 – 16 runs of subsequent CBV-weighted fMRI were conducted within each session depending on the animal condition.

3.3.3 MRI acquisition

Animals were placed inside a 9.4-T/31-cm horizontal bore magnet and 12-cm diameter gradient insert (maximum gradient strength of 40 Gauss/cm) interfaced to a Unity INOVA console (Varian, Palo Alto, CA, USA). A custom-built balanced single loop coil with 1.7-cm diameter was used for improving signal-to-noise ratio over the visual cortical area. Sets of three-plane scout images were acquired for positioning the scout fMRI slices. Based on the scout BOLD fMRI studies, single coronal 1-mm thick slice was selected perpendicular to the cortical surface. To acquire high-resolution anatomical reference, myelin-enhanced T_1 -weighted images were obtained using multiple-segment inversion-recovery turbo fast low angle shot (IR-TurboFLASH) sequence. Microvasculature-sensitive T_2 -weighted images were obtained using fast spin echo sequence after MION injection. Temporal frequency-dependent fMRI data were acquired using two-shot gradient-recalled echo planar imaging (GR-EPI) sequence with slice thickness = 1 mm, FOV = $20.1 \times 13.4 \text{ mm}^2$, matrix size = 96×64 zero-filled to 128×128 , TE = 25-ms (BOLD fMRI) and 10-ms (CBV-weighted fMRI), and TR= 0.5 s per segment.

3.3.4 fMRI maps generation

For BOLD fMRI data, a linear detrend and a Fermi high-pass temporal filter with a radius of 0.021 Hz and a width of 0.001 Hz was applied to minimize signal fluctuations induced by low frequency signal drifting (<0.021 Hz). For CBV-weighted fMRI data, the linear detrend was not applied and a Fermi low-pass filter with a radius of 0.0017 Hz was applied in addition to the high-pass filter. In this way, the slow trend of MION wash-out in the blood was preserved. To reduce the breathing-related fluctuation, a Gaussian notch temporal filter with the center

frequency determined by the respiration rate of each run was applied. The bandwidth and magnitude of both filters were determined empirically. To determine the proper hemodynamic response function (HRF), an independent component analysis was carried out using MELODIC in FSL (FMRIB's Software Library) (158) and a double gamma HRF was determined from the time course of the first independent component. fMRI activation maps were calculated using FMRI Expert Analysis Tool, part of FSL, with hemodynamic response function set to double gamma function and cluster significance threshold of $p = 0.05$ (159).

3.3.5 Quantitative region of interest analysis of temporal frequency stimulus

The ROI of supragranular layer (red), granular layer (green), infragranular layer (blue) were defined on the myelin-enhanced IR-TurboFLASH images (Figure 3.1: right) manually, based on the myelin-sensitive T_1 -weighted the and microvascular-sensitive spin-echo images. In T_1 -weighted image, the bright stripe at A17 could be clearly visualized in the middle of the

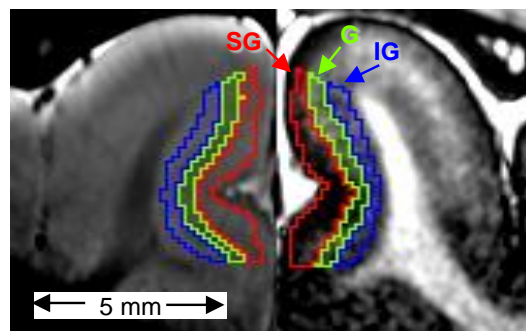


Figure 3.1 Defining regions of three cortical layers.

ROI of supragranular layer (SG: red), granular layer (G: green) and infragranular layer (IG: blue) were defined on T2 weighted image (left) and T1-weighted image (right). ROI of granular layer delineated the rich myelin layer shown as the bright band in T1 weighted image and high capillary density layer shown as the hypo-intensity band in T2-weighted image.

primary visual cortex, which was presumably the granular layer. In the microvasculature-sensitive fast spin echo image after the injection of MION, the hypo-intensity band (Figure 3.1: left) (200) resulting from high capillary density was also believed to be the granular layer (205). Regional time courses of relative BOLD change and BOLD-compensated relative CBV were then extracted and calculated from the fMRI data with custom-written Matlab script. To minimize the bias toward particular animal, the normalized temporal frequency tuning curves were generated by first averaging from 4 s after stimulation onset to 4 s after stopping of the stimulation (i.e. 5 – 28 s) with respect to each temporal frequency. Then, the time-averaged responses were normalized to the maximum response of one temporal frequency and averaged across animals. The preferred frequency, i.e. the temporal frequency of the maximum response, was obtained by fitting the normalized BOLD response and the logarithm of the temporal frequency with the Gaussian distribution (3) using Ezyfit toolbox in Matlab (164).

3.4 RESULTS

Figure 3.2 shows the layer-dependent BOLD (top row) and CBV-weighted (bottom row) fMRI activation maps of two temporal frequencies, 2 Hz (left column) and 20 Hz (right column), overlaid on the baseline GR-EPI image in one cat. Maps of 1 Hz and 10 Hz are not shown here since they are similar to the map of 2 Hz. The BOLD response was the highest on the cortical surface (see Figure 3.2A and Figure 3.2B) because of susceptibility effect of large pial vessels, which might obscure the laminar temporal frequency tuning. In CBV-weighted fMRI (Figure 3.2C and Figure 3.2D), there was little activation on the cortical surface, thus layer-dependent responses could be compared across temporal frequency. Both BOLD and CBV-weighted fMRI

responses were lower in both A17 and A18 at 20 Hz stimulation than at lower temporal frequency (Figure 3.2A &C vs. Figure 3.2B &D).

The averaged BOLD and relative CBV time courses (n=7) were obtained from

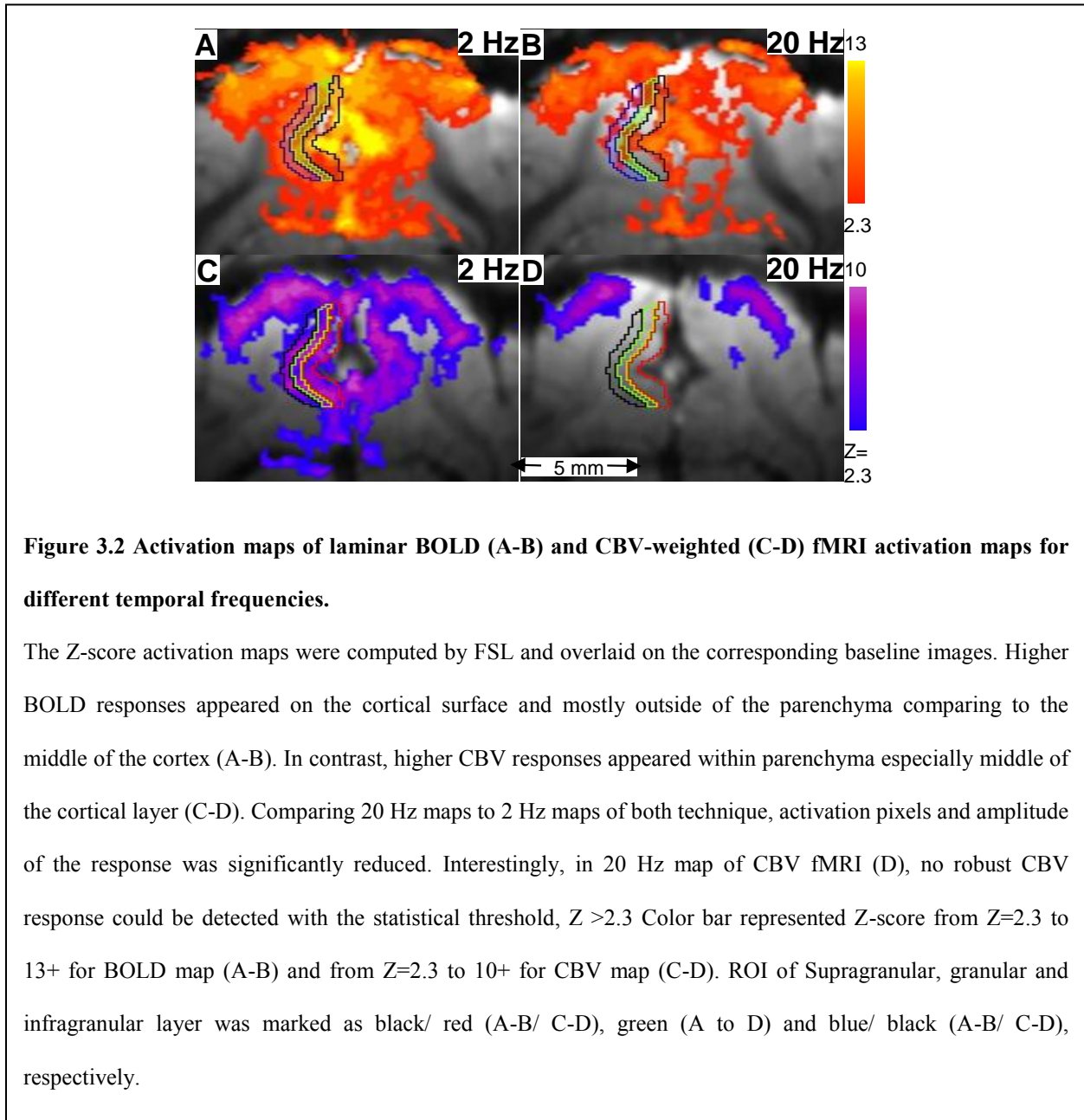


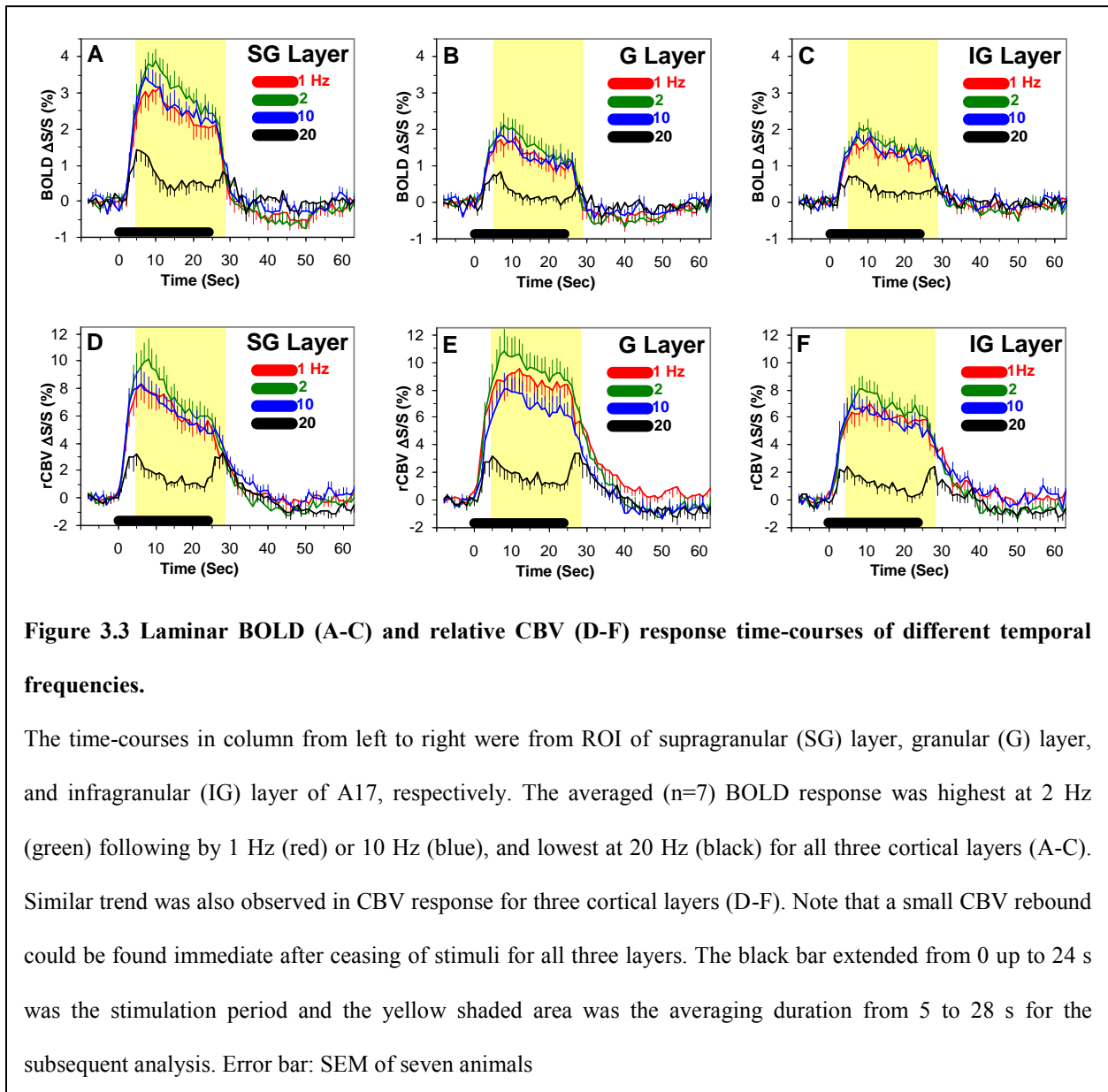
Figure 3.2 Activation maps of laminar BOLD (A-B) and CBV-weighted (C-D) fMRI activation maps for different temporal frequencies.

The Z-score activation maps were computed by FSL and overlaid on the corresponding baseline images. Higher BOLD responses appeared on the cortical surface and mostly outside of the parenchyma comparing to the middle of the cortex (A-B). In contrast, higher CBV responses appeared within parenchyma especially middle of the cortical layer (C-D). Comparing 20 Hz maps to 2 Hz maps of both technique, activation pixels and amplitude of the response was significantly reduced. Interestingly, in 20 Hz map of CBV fMRI (D), no robust CBV response could be detected with the statistical threshold, $Z > 2.3$. Color bar represented Z-score from $Z=2.3$ to 13+ for BOLD map (A-B) and from $Z=2.3$ to 10+ for CBV map (C-D). ROI of Supragranular, granular and infragranular layer was marked as black/ red (A-B/ C-D), green (A to D) and blue/ black (A-B/ C-D), respectively.

supragranular (left column), granular (middle column), infragranular layer ROI (right column) in A17 for four temporal frequency stimuli (Figure 3.3). Both the BOLD and the relative CBV responses reached their peak around 7-8 s and slightly decreased during the remaining

stimulation period. The BOLD time courses were highest on supragranular layer, while the relative CBV time courses were highest at granular layer. The CBV time courses showed significant rebound after the 20-Hz stimulation stop in six out of seven animals. This off-response is one of the reasons that most of the pixels fail to correlate with the hemodynamic response function for 20-Hz stimuli in A17 (Figure 3.2D).

To generate the temporal frequency tuning curves, normalized BOLD and relative CBV



responses were averaged over seven animals for three cortical layers and then plotted against four temporal frequencies in Figure 3.4. Both BOLD (Figure 3.4A) and relative CBV responding to 20 Hz stimulation (Figure 3.4B) were significantly lower than other three frequencies. No significant difference is found for three cortical layers in any temporal frequency for BOLD and CBV fMRI. Correlation coefficients of the BOLD tuning curves were 0.998, 0.998, and 0.997 for supragranular vs. granular layer, supragranular vs. infragranular layer and granular vs. infragranular layer, respectively. Correlation coefficients of the relative CBV tuning curves were 0.997, 0.999, and 0.999 for supragranular vs. granular layer, supragranular vs. infragranular layer and granular vs. infragranular layer, respectively. All the curves were highly correlated with p value less than 10^{-5} . The fitted preferred frequency for these three layers of BOLD are 3.16 Hz, 2.99 Hz and 3.12 Hz whereas relative CBV are 2.98 Hz, 2.74 Hz and 2.83 Hz with correlation coefficients larger than 0.9. Therefore, the trend of laminar BOLD tuning curves and laminar relative CBV tuning curves are similar to one another.

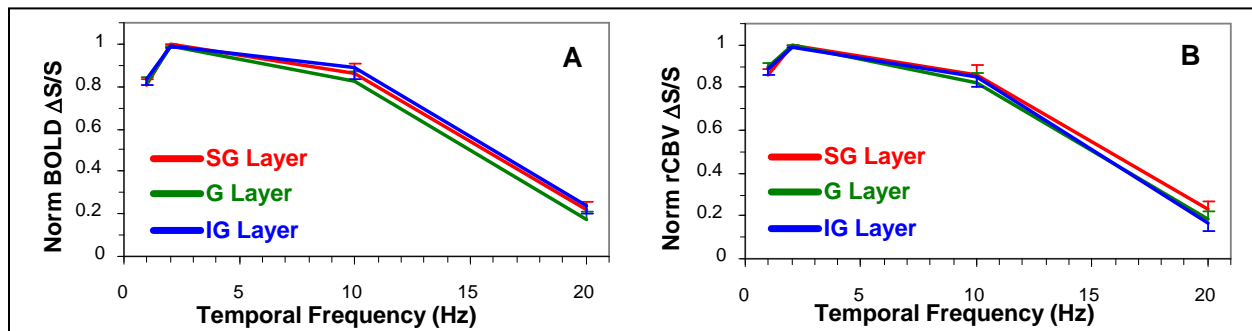


Figure 3.4 Temporal frequency tuning curves of laminar BOLD fMRI (A) and relative CBV fMRI (B).

No significant difference of BOLD or CBV response could be found among infragranular layer (blue), granular layer (green) and supragranular layer (red) for each frequency. Error bar: SEM of seven animals

3.5 DISCUSSION

3.5.1 Layer-dependent temporal frequency preference

In primary visual cortex, i.e. A17, neurons at supragranular, granular and infragranular layer exhibit different temporal frequency preference (206, 207). Neural responses to temporal frequency of visual stimuli have been shown to peak at ~ 3.5 Hz in the supragranular layer, ~ 3.1 Hz in the granular (middle) layer and ~ 6.0 Hz in the infragranular layer of the cat (206). The relative spiking activity of supragranular and granular layer at A17 drops significantly at higher temporal frequency comparing to lower temporal frequency. In contrast, the relative spiking activity of infragranular layer does not drop as much as the other two layers at higher temporal frequency comparing to lower temporal frequency. In addition to relative spiking activity which is related to neural output, the preferred frequency of laminar synaptic activity related to neural input can be derived from the hierarchical order of mammalian visual system. One can assume that the preferred frequency of the upstream spiking activity can predict the downstream synaptic activity. LGN projects mainly to granular layer and to infragranular layer of primary visual cortex and then granular layer projects to supragranular layer (208). The aforementioned model of visual pathway is highly simplified for the purpose of deriving the temporal frequency preference of laminar synaptic activity. The neural input (synaptic activity) of infragranular layer and supragranular layer is analogous to the spiking activity (output) of LGN and granular layer, respectively. The temporal frequency preference measured by spiking activity of LGN is about 4 - 11 Hz (1) and is higher than that of granular and supragranular layer. Therefore, the synaptic temporal frequency preference of granular and infragranular layer is similar to the spiking temporal frequency preference of LGN (148). The synaptic temporal frequency preference of

supragranular layer is similar to spiking temporal frequency preference of granular layer. The simplified visual pathway and the temporal frequency preference of known spiking preferred frequency and predicted synaptic preferred frequency are summarized in the Table 3.1. The predicted synaptic preferred frequency is labeled as high for granular and infragranular layer indicating that it is higher than that of supragranular layer. Overall, each layer exhibits unique combination of temporal frequency preference of known input and predicted output.

Despite of shift in laminar temporal frequency preference of spiking activity and synaptic activity, there is no significant difference in the laminar tuning curves of BOLD and CBV as shown in Figure 3.4. No preferred frequency shift can be observed across layers, which disagree with the results from reported spiking activity and predicted synaptic activity. Hence, our result indicates that hemodynamic response does not reflect the change in laminar neural response.

Table 3.5.1 Temporal frequency preference of known spiking activity and predicted synaptic activity

		Preferred Frequency	
		Known Spiking	Predicted Synaptic
Cortical Layers	Supragranular	3.5	<i>Low</i>
	Granular	3.1	High
	Infragranular	6	High
LGN		4-11	

3.5.2 Comparison to other studies

BOLD response has been reported to be specific to the glomerular layer of rat olfactory bulb which is the layer with the highest neural response (194). However, glomerular layer of the olfactory bulb is also the outermost layer (209, 210) which is sensitive to non-specific

susceptibility effect induced from the superficial draining veins. Additionally, since the laminar organization of olfactory bulb is quite different from that of somatosensory cortex, olfactory bulb findings cannot be generalized to other cortical areas. In primate visual cortex, BOLD fMRI has been reported to be specific to neural activity utilizing the preference of directional visual stimulus in the granular layer (211). However, the granular layer has higher vascular reactivity across the cortex, thus high differential BOLD response may be due to higher blood flow or volume contribution. Further investigations are necessary to elucidate the relationship between laminar neural and vascular responses.

3.5.3 Potential limitations

Potential limitations of these studies include inaccurate definition of three laminar ROIs and partial volume contamination. To minimize the error in granular layer ROI selection, laminar ROIs were defined on myelin-enhanced T_1 -weighted image and then refined on microvasculature-sensitive T_2 -weighted image (Figure 3.1). Partial volume contributions from cerebrospinal fluid and white matter to the nearby gray matter ROI were examined on the corresponding 3-D venographic image with isotropic voxel size of $157^3\mu\text{m}^3$. Minimal cerebrospinal fluid or white matter were included in the ROIs over 1-mm slice thickness of our functional image. Another potential limitation is that our stimulus paradigm contained only four temporal frequencies due to the constriction of experimental time. More temporal frequencies are desirable to differentiate small preferred frequency shift in laminar-specific neural activity. However, using the similar stimulus paradigm, prior studies in areal temporal frequency preference has been shown to detect ~ 1.3 Hz temporal frequency shift between A17 and A18 (212) which is smaller than the expected difference between infra- and supragranular layer.

Moreover, the sensitivity of our fMRI protocol may not have enough sensitivity to detect the visual stimulus-induced change in laminar hemodynamic response. Recently, our group has reported BOLD or CBV-weighted fMRI can be used to map the orientation columns in cat visual cortex (108, 213). This indicates that our fMRI protocol has sufficient sensitivity to differentiate change in underlying neural response in sub-millimeter scale. However, the thickness of the granular layer in feline A17 is less than 0.6 mm which is smaller than the diameter of a orientation column in A18 (~0.8 mm) (169). Thus, higher sensitivity is required for fMRI to detect the laminar hemodynamic response. Further signal averaging, use of ultra-high magnetic MRI system and cryogenic coil may increase the sensitivity to detect the laminar fMRI signal in the future.

3.5.4 Conclusion

We have successfully used high resolution fMRI to generate the laminar temporal frequency tuning curve of visual system in anesthetized cats. Temporal frequency tuning curves of laminar BOLD and CBV are almost identical across layers, even though different temporal frequency preference of spiking activity between upper and lower cortical layers are reported in the literature. Furthermore, it is also inconsistent with the preferred frequency of synaptic activity derived from the hierarchical order of early visual system. Therefore, the laminar hemodynamic responses including BOLD and CBV do not reflect the change of the laminar neural response.

3.5.5 Acknowledgments

This work is funded by NIH grants EB003324, EB003375, and NS44589. We thank Ping Wang and Michelle Tasker for animal preparation, Kristy Hendrich for 9.4 T support. We are also grateful to Tae Kim, Alberto Vazquez and Kristy Hendrich for helpful discussions.

4.0 SUMMARY AND FUTURE DIRECTIONS

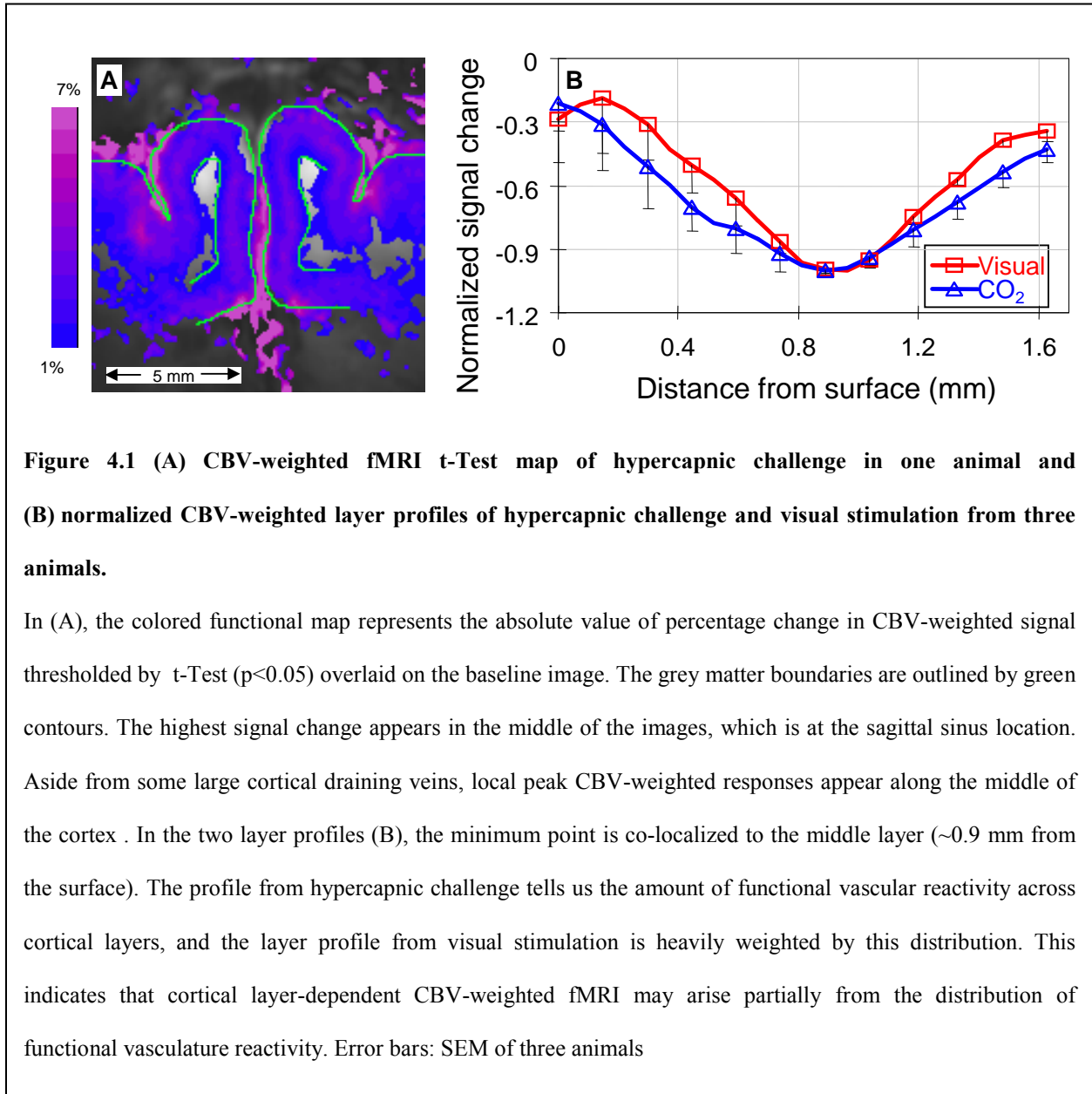
4.1 SUMMARY

In the previous two chapters, I successfully utilized fMRI to generate areal and laminar temporal frequency tuning curves from the visual system in anesthetized cats. The areal BOLD fMRI tuning curve from A17 was compared to tissue pO₂ and electrophysiological measurements such as LFP and spiking activity; the BOLD fMRI tuning curve seems to resemble the LFP low frequency band (LFP_L) and spiking activity, whereas it is less similar to the LFP gamma band (LFP_γ). Significant discrepancy is found between tuning curves obtained from BOLD fMRI and tissue pO₂ studies. Furthermore, the tuning curves for BOLD and relative CBV responses are almost identical for each of the three cortical layers, in contrast to neuronal activity tuning curves, which have different peak frequencies for each of the cortical layers. Hence, laminar hemodynamic responses (including BOLD and relative CBV) may not reflect a change in laminar neural activity. One reasonable explanation may be that the laminar hemodynamic response is dominated by functional vascular reactivity.

4.2 FUTURE DIRECTIONS

4.2.1 Hypercapnia challenge to investigate layer-dependent functional vascular reactivity

Vascular reactivity is known to depend on vessel size (214) and distribution of vessel sizes is layer-dependent (204). Hence, layer-dependent hemodynamic responses may be related to the layer dependence of vascular reactivity (98). To investigate the role of vascular reactivity in layer-dependent hemodynamic responses, my colleague, Dr. Fuqiang Zhao, performed CBV-weighted fMRI studies during hypercapnic challenges during 2-Hz visual stimulus. A hypercapnic challenge induces global (neurally non-specific) hemodynamic responses (59, 215, 216) and therefore has been used to normalize the BOLD response evoked by neural stimuli (217, 218). Thus, hypercapnia is ideal for examining the layer-dependent hemodynamic response induced by vascular reactivity without affecting neural activity itself (219-222). I compared cortical layer profiles of hypercapnic challenge vs. visual stimulation from Dr. Zhao's CBV-weighted fMRI studies. Some preliminary data appears in Figure 4.1, while details of the methods will be included in the manuscript to be submitted.



From Dr. Zhao's CBV-weighted fMRI data during hypercapnic challenge, we ascertain that layer-dependent vascular reactivity has a similar layer profile as the neural stimulus-evoked hemodynamic response. Because the layer-dependent hemodynamic response is independent of underlying neural activity, it is dominated by the layer-dependent vascular reactivity. Therefore, the granular layer of the visual cortex has the most reactive vessels and exhibits the highest hemodynamic response regardless of laminar neural response.

The mechanism behind layer-dependent vascular reactivity can be elucidated by the intrinsic property of laminar hemodynamic regulation which is not specific to neural response. Arteries branching out from the superficial arteries in the pia mater penetrate into parenchyma perpendicular to the surface. Then, these arteries branch into small arterioles normal to the penetrating artery, which connect to the capillary bed. Blood in capillaries drains to small venules, connected penetrating veins, and finally to pial draining veins. The column-like vasculature works as one unit. Whenever a stimulation-induced flow change in the penetrating arteries occurs, corresponding vascular modules may behave similarly regardless of the type of stimulation. This vascular module is critical for cortical hemodynamic regulation. If capillaries, which are close to neurons, actively dilate during increased neural activity, then it is possible that the CBV change can be specific to laminar neuronal activity. Data from our group suggests that actively dilating vessels are not the capillaries (98), but rather larger-than-capillary vessels which deliver blood into multiple layers and do not have layer-specificity. Recently, by using two-photon microscopy and pharmaceutical intervention, precapillary and penetrating arterioles have been shown to actively regulate cerebral blood flow induced by neural activity (223). The same study also demonstrated that capillaries dilate passively, which corroborates our finding. Although hemodynamic responses along blood supply territories may be actively controlled by neurons/astrocytes, there is no evidence of laminar specificity of this effect.

4.2.2 Optogenetic fMRI to study laminar hemodynamic regulation in a single cortical layer

Although the temporal frequency tuning model is able to modulate laminar neural activity, under high temporal frequency stimulus the granular layer has the highest overall neural

activity of the three layers due to its higher neuronal density (224). Thus, a better way to selectively excite a single cortical layer is desirable. Recently, the optogenetic technique (225, 226) has emerged as a new animal model to study the fine control of the hemodynamic response (227). The principle of optogenetics relies on inserting light-sensitive proteins, channelrhodopsins, into the genome of target cells (such as brain neurons) by a virus vector which will then express channelrhodopsins on their membrane. As a result, these neurons can be selectively excited by light at a pre-defined wavelength. This model can then be utilized to selectively excite a single cortical layer and examine BOLD and CBV responses in future laminar studies.

BIBLIOGRAPHY

1. Derrington AM, Fuchs AF. Spatial and temporal properties of X and Y cells in the cat lateral geniculate nucleus. *J Physiol.* 1979;293:347-64. PMID: 1280717.
2. Bisti S, Carmignoto G, Galli L, Maffei L. Spatial-frequency characteristics of neurones of area 18 in the cat: dependence on the velocity of the visual stimulus. *J Physiol.* 1985;359:259-68. PMID: 1193374.
3. Allison JD, Smith KR, Bonds AB. Temporal-frequency tuning of cross-orientation suppression in the cat striate cortex. *Vis Neurosci.* 2001;18(6):941-8.
4. DeAngelis GC, Ohzawa I, Freeman RD. Spatiotemporal organization of simple-cell receptive fields in the cat's striate cortex. I. General characteristics and postnatal development. *J Neurophysiol.* 1993;69(4):1091-117.
5. Duvernoy HM, Delon S, Vannson J. Cortical blood vessels of the human brain. *Brain Research Bulletin.* 1981;7(5):519-79.
6. Herbert DA, Mitchell RA. Blood gas tensions and acid-base balance in awake cats. *J Appl Physiol.* 1971;30(3):434-6.
7. Reinoso-Suárez F. *Topographischer Hirnatlas der Katze für experimental-physiologische Untersuchungen.* Darmstadt: E. Merck AG; 1961.
8. Gardner JL. Is cortical vasculature functionally organized? *NeuroImage.* 2010;49(3):1953-6.
9. Huettel SA, Song AW, McCarthy G. *Functional magnetic resonance imaging.* Sunderland, Mass.: Sinauer Associates, Publishers; 2004.
10. Kim SG, Ugurbil K. High-resolution functional magnetic resonance imaging of the animal brain. *Methods.* 2003;30(1):28-41.
11. Kim SG, Ugurbil K. Functional magnetic resonance imaging of the human brain. *J Neurosci Methods.* 1997;74(2):229-43.
12. Kim SG, Fukuda M. Lessons from fMRI about mapping cortical columns. *Neuroscientist.* 2008;14(3):287-99. PMID: 2613428.

13. Lauterbur PC. Image Formation by Induced Local Interactions: Examples Employing Nuclear Magnetic Resonance. *Nature*. 1973;242(5394):190-1.
14. Mansfield P. Multi-planar image formation using NMR spin echoes. *Journal of Physics C: Solid State Physics*. 1977;10(3):L55-L8.
15. Gerlach W, Stern O. Das magnetische Moment des Silberatoms. *Zeitschrift für Physik A Hadrons and Nuclei*. 1922;9(1):353-5.
16. Mohr PJ, Taylor BN, Newell DB. CODATA recommended values of the fundamental physical constants: 2006. *Reviews of Modern Physics*. 2008;80(2):633.
17. Ogawa S, Lee TM, Nayak AS, Glynn P. Oxygenation-sensitive contrast in magnetic resonance image of rodent brain at high magnetic fields. *Magn Reson Med*. 1990;14(1):68-78.
18. Bandettini PA, Wong EC, Hinks RS, Tikofsky RS, Hyde JS. Time Course Epi of Human Brain-Function during Task Activation. *Magnetic Resonance in Medicine*. 1992;25(2):390-7.
19. Blamire AM, Ogawa S, Ugurbil K, Rothman D, McCarthy G, Ellermann JM, et al. Dynamic mapping of the human visual cortex by high-speed magnetic resonance imaging. *Proc Natl Acad Sci U S A*. 1992;89(22):11069-73. PMID: 50485.
20. Kwong KK, Belliveau JW, Chesler DA, Goldberg IE, Weisskoff RM, Poncelet BP, et al. Dynamic Magnetic-Resonance-Imaging of Human Brain Activity during Primary Sensory Stimulation. *Proceedings of the National Academy of Sciences of the United States of America*. 1992;89(12):5675-9.
21. Ogawa S, Tank DW, Menon R, Ellermann JM, Kim SG, Merkle H, et al. Intrinsic signal changes accompanying sensory stimulation: functional brain mapping with magnetic resonance imaging. *Proc Natl Acad Sci U S A*. 1992;89(13):5951-5. PMID: 402116.
22. Belliveau JW, Kennedy DN, Jr., McKinstry RC, Buchbinder BR, Weisskoff RM, Cohen MS, et al. Functional mapping of the human visual cortex by magnetic resonance imaging. *Science*. 1991;254(5032):716-9.
23. Muckli L. What are we missing here? Brain imaging evidence for higher cognitive functions in primary visual cortex V1. *International Journal of Imaging Systems and Technology*. 2010;20(2):131-9.
24. Fox PT, Mintun MA, Reiman EM, Raichle ME. Enhanced Detection of Focal Brain Responses Using Intersubject Averaging and Change-Distribution Analysis of Subtracted PET Images. *J Cereb Blood Flow Metab*. 1988;8(5):642-53.
25. Raichle ME, Martin WRW, Herscovitch P, Mintun MA, Markham J. Brain Blood Flow Measured with Intravenous H²15O.: II. Implementation and Validation. *J Nucl Med*. 1983;24(9):790-8.

26. Eichling JO, Raichle ME, Grubb RL, Jr., Larson KB, Ter-Pogossian MM. In vivo determination of cerebral blood volume with radioactive oxygen-15 in the monkey. *Circ Res.* 1975;37(6):707-14.
27. Grubb RL, Jr., Raichle ME, Eichling JO, Ter-Pogossian MM. The effects of changes in PaCO₂ on cerebral blood volume, blood flow, and vascular mean transit time. *Stroke.* 1974;5(5):630-9.
28. Reivich M, Kuhl D, Wolf A, Greenberg J, Phelps M, Ido T, et al. The [18F]fluorodeoxyglucose method for the measurement of local cerebral glucose utilization in man. *Circ Res.* 1979;44(1):127-37.
29. Cherry SR. The 2006 Henry N. Wagner Lecture: Of mice and men (and positrons)--advances in PET imaging technology. *J Nucl Med.* 2006;47(11):1735-45.
30. Frostig RD, Lieke EE, Ts'o DY, Grinvald A. Cortical functional architecture and local coupling between neuronal activity and the microcirculation revealed by in vivo high-resolution optical imaging of intrinsic signals. *Proc Natl Acad Sci U S A.* 1990;87(16):6082-6. PMID: 54476.
31. Bonhoeffer T, Grinvald A. Iso-orientation domains in cat visual cortex are arranged in pinwheel-like patterns. *Nature.* 1991;353(6343):429-31.
32. Sherwood L. *Human Physiology: From Cells to Systems (Non-InfoTrac Version with CD-ROM)*; Brooks Cole; 2003.
33. Pauling L, Coryell CD. The Magnetic Properties and Structure of Hemoglobin, Oxyhemoglobin and Carbonmonoxyhemoglobin. *Proc Natl Acad Sci U S A.* 1936;22(4):210-6. PMID: 1076743.
34. Weisskoff RM, Kiihne S. MRI susceptometry: image-based measurement of absolute susceptibility of MR contrast agents and human blood. *Magn Reson Med.* 1992;24(2):375-83.
35. Lide D. *Crc Handbook of Chemistry and Physics, 90th Edition*; CRC; 2009.
36. Schenck JF. Health and physiological effects of human exposure to whole-body four-tesla magnetic fields during MRI. *Ann N Y Acad Sci.* 1992;649:285-301.
37. Spees WM, Yablonskiy DA, Oswald MC, Ackerman JJ. Water proton MR properties of human blood at 1.5 Tesla: magnetic susceptibility, T(1), T(2), T*(2), and non-Lorentzian signal behavior. *Magn Reson Med.* 2001;45(4):533-42.
38. Springer C, Xu Y, editors. *Aspects of bulk magnetic susceptibility in in vivo MRI and MRS.* European Magnetic Resonance Forum; 1991; Blonay, Switzerland.
39. Simpson JH, Carr HY. Diffusion and Nuclear Spin Relaxation in Water. *Physical Review.* 1958;111(5):1201.

40. Ugurbil K, Garwood M, Ellermann J, Hendrich K, Hinke R, Hu X, et al. Imaging at high magnetic fields: initial experiences at 4 T. *Magnetic Resonance Quarterly*. 1993;9(4):259.
41. Einstein A. *Investigations on the Theory of the Brownian Movement*: Dover Publications; 1956.
42. Gulliver G, editor. *Observations on the sizes and shapes of the red corpuscles of the blood of vertebrates, with drawings of them to a uniform scale, and extended and revised tables of measurements* 1875.
43. Thulborn KR, Waterton JC, Matthews PM, Radda GK. Oxygenation dependence of the transverse relaxation time of water protons in whole blood at high field. *Biochim Biophys Acta*. 1982;714(2):265-70.
44. Zhao F, Wang P, Kim SG. Cortical depth-dependent gradient-echo and spin-echo BOLD fMRI at 9.4T. *Magn Reson Med*. 2004;51(3):518-24.
45. Lee S-P, Silva AC, Ugurbil K, Kim S-G. Diffusion-weighted spin-echo fMRI at 9.4 T: Microvascular/tissue contribution to BOLD signal changes. *Magnetic Resonance in Medicine*. 1999;42(5):919-28.
46. Song AW, Wong EC, Tan SG, Hyde JS. Diffusion weighted fMRI at 1.5 T. *Magn Reson Med*. 1996;35(2):155-8.
47. Zhong J, Kennan RP, Fulbright RK, Gore JC. Quantification of intravascular and extravascular contributions to BOLD effects induced by alteration in oxygenation or intravascular contrast agents. *Magn Reson Med*. 1998;40(4):526-36.
48. Boxerman JL, Hamberg LM, Rosen BR, Weisskoff RM. MR contrast due to intravascular magnetic susceptibility perturbations. *Magn Reson Med*. 1995;34(4):555-66.
49. Boxerman JL, Bandettini PA, Kwong KK, Baker JR, Davis TL, Rosen BR, et al. The intravascular contribution to fMRI signal change: Monte Carlo modeling and diffusion-weighted studies in vivo. *Magn Reson Med*. 1995;34(1):4-10.
50. Eichling JO, Raichle ME, Grubb RL, Jr., Ter-Pogossian MM. Evidence of the limitations of water as a freely diffusible tracer in brain of the rhesus monkey. *Circ Res*. 1974;35(3):358-64.
51. Paulson OB, Hertz MM, Bolwig TG, Lassen NA. Filtration and diffusion of water across the blood-brain barrier in man. *Microvascular Research*. 1977;13(1):113-23.
52. Yamaguchi S, Yamakawa T, Niimi H. Red cell velocity and microvessel diameter measurement by a two fluorescent tracer method under epifluorescence microscopy: application to cerebral microvessels of cats. *Int J Microcirc Clin Exp*. 1992;11(4):403-16.
53. Weisskoff RM, Zuo CS, Boxerman JL, Rosen BR. Microscopic susceptibility variation and transverse relaxation: theory and experiment. *Magn Reson Med*. 1994;31(6):601-10.

54. Ogawa S, Menon RS, Tank DW, Kim SG, Merkle H, Ellermann JM, et al. Functional brain mapping by blood oxygenation level-dependent contrast magnetic resonance imaging. A comparison of signal characteristics with a biophysical model. *Biophys J*. 1993;64(3):803-12. PMID: 1262394.
55. Ogawa S, Lee TM, Barrere B. The sensitivity of magnetic resonance image signals of a rat brain to changes in the cerebral venous blood oxygenation. *Magn Reson Med*. 1993;29(2):205-10.
56. Turner R, Le Bihan D, Moonen CT, Despres D, Frank J. Echo-planar time course MRI of cat brain oxygenation changes. *Magn Reson Med*. 1991;22(1):159-66.
57. Ogawa S, Lee TM, Kay AR, Tank DW. Brain magnetic resonance imaging with contrast dependent on blood oxygenation. *Proc Natl Acad Sci U S A*. 1990;87(24):9868-72. PMID: 55275.
58. Ogawa S, Menon RS, Kim SG, Ugurbil K. On the characteristics of functional magnetic resonance imaging of the brain. *Annu Rev Biophys Biomol Struct*. 1998;27:447-74.
59. Rostrup E, Larsson HB, Toft PB, Garde K, Thomsen C, Ring P, et al. Functional MRI of CO₂ induced increase in cerebral perfusion. *NMR Biomed*. 1994;7(1-2):29-34.
60. Kim SG, Rostrup E, Larsson HB, Ogawa S, Paulson OB. Determination of relative CMRO₂ from CBF and BOLD changes: significant increase of oxygen consumption rate during visual stimulation. *Magn Reson Med*. 1999;41(6):1152-61.
61. Kim SG, Ugurbil K. Comparison of blood oxygenation and cerebral blood flow effects in fMRI: estimation of relative oxygen consumption change. *Magn Reson Med*. 1997;38(1):59-65.
62. Davis TL, Kwong KK, Weisskoff RM, Rosen BR. Calibrated functional MRI: mapping the dynamics of oxidative metabolism. *Proc Natl Acad Sci U S A*. 1998;95(4):1834-9. PMID: 19199.
63. Hyder F, Shulman RG, Rothman DL. A model for the regulation of cerebral oxygen delivery. *J Appl Physiol*. 1998;85(2):554-64.
64. He X, Yablonskiy DA. Quantitative BOLD: mapping of human cerebral deoxygenated blood volume and oxygen extraction fraction: default state. *Magn Reson Med*. 2007;57(1):115-26.
65. Lin W, Paczynski RP, Celik A, Hsu CY, Powers WJ. Effects of acute normovolemic hemodilution on T₂*-weighted images of rat brain. *Magn Reson Med*. 1998;40(6):857-64.
66. Lin W, Paczynski RP, Celik A, Hsu CY, Powers WJ. Experimental hypoxemic hypoxia: effects of variation in hematocrit on magnetic resonance T₂*-weighted brain images. *J Cereb Blood Flow Metab*. 1998;18(9):1018-21.

67. Levin JM, Frederick Bd, Ross MH, Fox JF, von Rosenberg HL, Kaufman MJ, et al. Influence of baseline hematocrit and hemodilution on BOLD fMRI activation. *Magnetic resonance imaging*. 2001;19(8):1055-62.
68. Lu H, Zhao C, Ge Y, Lewis-Amezcuca K. Baseline blood oxygenation modulates response amplitude: Physiologic basis for intersubject variations in functional MRI signals. *Magn Reson Med*. 2008;60(2):364-72. PMID: 2597505.
69. Kim SG, Hendrich K, Hu X, Merkle H, Ugurbil K. Potential pitfalls of functional MRI using conventional gradient-recalled echo techniques. *NMR Biomed*. 1994;7(1-2):69-74.
70. Gao JH, Miller I, Lai S, Xiong J, Fox PT. Quantitative assessment of blood inflow effects in functional MRI signals. *Magn Reson Med*. 1996;36(2):314-9.
71. Gao JH, Xiong J, Li J, Schiff J, Roby J, Lancaster JL, et al. Fast spin-echo characteristics of visual stimulation-induced signal changes in the human brain. *J Magn Reson Imaging*. 1995;5(6):709-14.
72. Edelman RR, Siewert B, Darby DG, Thangaraj V, Nobre AC, Mesulam MM, et al. Qualitative mapping of cerebral blood flow and functional localization with echo-planar MR imaging and signal targeting with alternating radio frequency. *Radiology*. 1994;192(2):513-20.
73. Frahm J, Merboldt K-D, Hänicke W, Kleinschmidt A, Boecker H. Brain or vein oxygenation or flow? On signal physiology in functional MRI of human brain activation. *NMR in Biomedicine*. 1994;7(1-2):45-53.
74. Duyn JH, Moonen CT, van Yperen GH, de Boer RW, Luyten PR. Inflow versus deoxyhemoglobin effects in BOLD functional MRI using gradient echoes at 1.5 T. *NMR Biomed*. 1994;7(1-2):83-8.
75. Haacke EM, Hopkins A, Lai S, Buckley P, Friedman L, Meltzer H, et al. 2D and 3D high resolution gradient echo functional imaging of the brain: venous contributions to signal in motor cortex studies. *NMR Biomed*. 1994;7(1-2):54-62.
76. Belliveau JW, Rosen BR, Kantor HL, Rzedzian RR, Kennedy DN, McKinstry RC, et al. Functional cerebral imaging by susceptibility contrast NMR. *Magnetic Resonance in Medicine*. 1990;14(3):538-46.
77. Sorensen AG, Tievsky AL, Ostergaard L, Weisskoff RM, Rosen BR. Contrast agents in functional MR imaging. *J Magn Reson Imaging*. 1997;7(1):47-55.
78. Rosen BR, Belliveau JW, Vevea JM, Brady TJ. Perfusion imaging with NMR contrast agents. *Magn Reson Med*. 1990;14(2):249-65.
79. Rosen BR, Belliveau JW, Aronen HJ, Kennedy D, Buchbinder BR, Fischman A, et al. Susceptibility contrast imaging of cerebral blood volume: human experience. *Magn Reson Med*. 1991;22(2):293-9; discussion 300-3.

80. Lin W, Celik A, Paczynski RP. Regional cerebral blood volume: a comparison of the dynamic imaging and the steady state methods. *J Magn Reson Imaging*. 1999;9(1):44-52.
81. Moseley ME, Chew WM, White DL, Kucharczyk J, Litt L, Derugin N, et al. Hypercarbia-induced changes in cerebral blood volume in the cat: a 1H MRI and intravascular contrast agent study. *Magn Reson Med*. 1992;23(1):21-30.
82. Schwarzbauer C, Syha J, Haase A. Quantification of regional blood volumes by rapid T1 mapping. *Magnetic Resonance in Medicine*. 1993;29(5):709-12.
83. Lauffer RB, Parmelee DJ, Ouellet HS, Dolan RP, Sajiki H, Scott DM, et al. MS-325: a small-molecule vascular imaging agent for magnetic resonance imaging. *Academic radiology*. 1996;3:S356.
84. Johnson KM, Tao JZ, Kennan RP, Gore JC. Gadolinium-bearing red cells as blood pool MRI contrast agents. *Magnetic Resonance in Medicine*. 1998;40(1):133-42.
85. van Zijl PC, Eleff SM, Ulatowski JA, Oja JM, Ulug AM, Traystman RJ, et al. Quantitative assessment of blood flow, blood volume and blood oxygenation effects in functional magnetic resonance imaging. *Nat Med*. 1998;4(2):159-67.
86. Kent TA, Quast MJ, Kaplan BJ, Lifsey RS, Eisenberg HM. Assessment of a superparamagnetic iron oxide (AMI-25) as a brain contrast agent. *Magn Reson Med*. 1990;13(3):434-43.
87. Josephson L, Groman EV, Menz E, Lewis JM, Bengel H. A functionalized superparamagnetic iron oxide colloid as a receptor directed MR contrast agent. *Magnetic resonance imaging*. 1990;8(5):637-46.
88. Weissleder R, Elizondo G, Wittenberg J, Rabito CA, Bengel HH, Josephson L. Ultrasmall superparamagnetic iron oxide: characterization of a new class of contrast agents for MR imaging. *Radiology*. 1990;175(2):489-93.
89. Shen T, Weissleder R, Papisov M, Bogdanov A, Jr., Brady TJ. Monocrystalline iron oxide nanocompounds (MION): physicochemical properties. *Magn Reson Med*. 1993;29(5):599-604.
90. Mandeville JB, Marota JJ, Kosofsky BE, Keltner JR, Weissleder R, Rosen BR, et al. Dynamic functional imaging of relative cerebral blood volume during rat forepaw stimulation. *Magn Reson Med*. 1998;39(4):615-24.
91. Kennan RP, Scanley BE, Innis RB, Gore JC. Physiological basis for BOLD MR signal changes due to neuronal stimulation: separation of blood volume and magnetic susceptibility effects. *Magn Reson Med*. 1998;40(6):840-6.
92. van Bruggen N, Busch E, Palmer JT, Williams SP, de Crespigny AJ. High-resolution functional magnetic resonance imaging of the rat brain: mapping changes in cerebral blood volume using iron oxide contrast media. *J Cereb Blood Flow Metab*. 1998;18(11):1178-83.

93. Mandeville JB, Jenkins BG, Kosofsky BE, Moskowitz MA, Rosen BR, Marota JJ. Regional sensitivity and coupling of BOLD and CBV changes during stimulation of rat brain. *Magn Reson Med*. 2001;45(3):443-7.
94. Kennan RP, Scanley BE, Gore JC. Physiologic basis for BOLD MR signal changes due to hypoxia/hyperoxia: separation of blood volume and magnetic susceptibility effects. *Magn Reson Med*. 1997;37(6):953-6.
95. Kennan RP, Zhong J, Gore JC. Intravascular susceptibility contrast mechanisms in tissues. *Magnetic Resonance in Medicine*. 1994;31(1):9-21.
96. Hoppel BE, Weisskoff RM, Thulborn KR, Moore JB, Kwong KK, Rosen BR. Measurement of regional blood oxygenation and cerebral hemodynamics. *Magn Reson Med*. 1993;30(6):715-23.
97. Yablonskiy DA, Haacke EM. Theory of NMR signal behavior in magnetically inhomogeneous tissues: the static dephasing regime. *Magn Reson Med*. 1994;32(6):749-63.
98. Zhao F, Wang P, Hendrich K, Ugurbil K, Kim SG. Cortical layer-dependent BOLD and CBV responses measured by spin-echo and gradient-echo fMRI: insights into hemodynamic regulation. *Neuroimage*. 2006;30(4):1149-60.
99. Mandeville JB, Leite FP, Marota JJ. Spin-echo MRI underestimates functional changes in microvascular cerebral blood plasma volume using exogenous contrast agent. *Magn Reson Med*. 2007;58(4):769-76.
100. Tropres I, Grimault S, Vaeth A, Grillon E, Julien C, Payen JF, et al. Vessel size imaging. *Magn Reson Med*. 2001;45(3):397-408.
101. Dennie J, Mandeville JB, Boxerman JL, Packard SD, Rosen BR, Weisskoff RM. NMR imaging of changes in vascular morphology due to tumor angiogenesis. *Magnetic Resonance in Medicine*. 1998;40(6):793-9.
102. Bolan PJ, Yacoub E, Garwood M, Ugurbil K, Harel N. In vivo micro-MRI of intracortical neurovasculature. *NeuroImage*. 2006;32(1):62-9.
103. Dunn JF, Roche MA, Springett R, Abajian M, Merlis J, Daghlian CP, et al. Monitoring angiogenesis in brain using steady-state quantification of ΔR_2 with MION infusion. *Magnetic Resonance in Medicine*. 2004;51(1):55-61.
104. Lin CY, Lin MH, Cheung WM, Lin TN, Chen JH, Chang C. In vivo cerebrovasculature visualization using 3D [Delta] R2-based microscopy of magnetic resonance angiography (3D [Delta] R2-mMRA). *NeuroImage*. 2009;45(3):824-31.
105. Lu H, Scholl CA, Zuo Y, Stein EA, Yang Y. Quantifying the blood oxygenation level dependent effect in cerebral blood volume-weighted functional MRI at 9.4T. *Magn Reson Med*. 2007;58(3):616-21.

106. Kiselev VG, Posse S. Analytical model of susceptibility-induced MR signal dephasing: effect of diffusion in a microvascular network. *Magn Reson Med.* 1999;41(3):499-509.
107. Mandeville JB, Jenkins BG, Chen YC, Choi JK, Kim YR, Belen D, et al. Exogenous contrast agent improves sensitivity of gradient-echo functional magnetic resonance imaging at 9.4 T. *Magn Reson Med.* 2004;52(6):1272-81.
108. Fukuda M, Moon CH, Wang P, Kim SG. Mapping iso-orientation columns by contrast agent-enhanced functional magnetic resonance imaging: reproducibility, specificity, and evaluation by optical imaging of intrinsic signal. *J Neurosci.* 2006;26(46):11821-32.
109. Zhao F, Wang P, Hendrich K, Kim SG. Spatial specificity of cerebral blood volume-weighted fMRI responses at columnar resolution. *NeuroImage.* 2005;27(2):416-24.
110. Schelshorn DW, Schneider A, Kuschinsky W, Weber D, Krüger C, Dittgen T, et al. Expression of hemoglobin in rodent neurons. *Journal of Cerebral Blood Flow & Metabolism.* 2008;29(3):585-95.
111. Swanson RA. Physiologic coupling of glial glycogen metabolism to neuronal activity in brain. *Canadian Journal of Physiology and Pharmacology.* 1992;70(S1):138-44.
112. Roy CS, Sherrington C. On the regulation of the blood-supply of the brain. *The Journal of physiology.* 1890;11(1-2):85.
113. Magistretti PJ, Pellerin L. Cellular bases of brain energy metabolism and their relevance to functional brain imaging: evidence for a prominent role of astrocytes. *Cerebral Cortex.* 1996;6(1):50.
114. Iadecola C, Nedergaard M. Glial regulation of the cerebral microvasculature. *Nature neuroscience.* 2007;10(11):1369-76.
115. Attwell D, Iadecola C. The neural basis of functional brain imaging signals. *TRENDS in Neurosciences.* 2002;25(12):621-5.
116. Fox PT, Raichle ME. Focal physiological uncoupling of cerebral blood flow and oxidative metabolism during somatosensory stimulation in human subjects. *Proceedings of the National Academy of Sciences of the United States of America.* 1986;83(4):1140.
117. Fox PT, Raichle ME, Mintun MA, Dence C. Nonoxidative glucose consumption during focal physiologic neural activity. *Science.* 1988;241(4864):462.
118. Magistretti PJ, Pellerin L, Rothman DL, Shulman RG. Energy on demand. *Science.* 1999;283(5401):496.
119. Raichle ME, Mintun MA. Brain work and brain imaging. *Annu Rev Neurosci.* 2006;29:449-76.
120. Moonen CTW, Bandettini PA. *Functional mri*: Springer Verlag; 2000.

121. Faro SH, Mohamed FB, Corporation E. Functional MRI: basic principles and clinical applications: Springer; 2006.
122. Noll DC. A primer on MRI and functional MRI. Retrieved from: <http://www.eecs.umich.edu/~dnoll/primer2pdf>. 2001.
123. Faraci FM, Breese KR. Nitric oxide mediates vasodilatation in response to activation of N-methyl-D-aspartate receptors in brain. *Circulation research*. 1993;72(2):476.
124. Iadecola C. Regulation of the cerebral microcirculation during neural activity: is nitric oxide the missing link? *TRENDS in Neurosciences*. 1993;16(6):206-14.
125. Lee SP, Duong TQ, Yang G, Iadecola C, Kim SG. Relative changes of cerebral arterial and venous blood volumes during increased cerebral blood flow: implications for BOLD fMRI. *Magnetic Resonance in Medicine*. 2001;45(5):791-800.
126. Ito H, Takahashi K, Hatazawa J, Kim SG, Kanno I. Changes in human regional cerebral blood flow and cerebral blood volume during visual stimulation measured by positron emission tomography. *J Cereb Blood Flow Metab*. 2001;21(5):608-12.
127. Vazquez AL, Fukuda M, Tasker ML, Masamoto K, Kim SG. Changes in cerebral arterial, tissue and venous oxygenation with evoked neural stimulation: implications for hemoglobin-based functional neuroimaging. *J Cereb Blood Flow Metab*. 2010;30(2):428-39. PMID: 2900190.
128. Hubel DH, Wiesel TN. Receptive fields, binocular interaction and functional architecture in the cat's visual cortex. *J Physiol*. 1962;160:106-54. PMID: 1359523.
129. DeLahunta A, Glass E. *Veterinary neuroanatomy and clinical neurology*: WB Saunders Company; 2008.
130. Cucchiari JB. Early development of the retinal line of decussation in normal and albino ferrets. *The Journal of Comparative Neurology*. 1991;312(2):193-206.
131. Schober W. The primary optical projection in albino and pigmented rats. *Anatomischer Anzeiger*. 1975;137(3):257.
132. Sherman SM, Guillery RW. On the actions that one nerve cell can have on another: Distinguishing “drivers” from “modulators”. *Proceedings of the National Academy of Sciences of the United States of America*. 1998;95(12):7121-6.
133. Glaser JS. *Neuro-ophthalmology*: Lippincott Williams & Wilkins; 1999.
134. Peters A, Palay SL, Webster HF. *The fine structure of the nervous system: neurons and their supporting cells*: Oxford University Press; 1991.

135. Diaz-Flores L, Gutierrez R, Varela H, Rancel N, Valladares F. Microvascular pericytes, a review of their morphological and functional characteristics. *Histology and histopathology*. 1991.
136. Klein B, Kuschinsky W, Schrock H, Vetterlein F. Interdependency of local capillary density, blood flow, and metabolism in rat brains. *Am J Physiol*. 1986;251(6 Pt 2):H1333-40.
137. Peppiatt CM, Howarth C, Mobbs P, Attwell D. Bidirectional control of CNS capillary diameter by pericytes. *Nature*. 2006;443(7112):700-4. PMID: 1761848.
138. Faraci FM, Heistad DD. Regulation of large cerebral arteries and cerebral microvascular pressure. *Circ Res*. 1990;66(1):8-17.
139. Fujii K, Heistad DD, Faraci FM. Flow-mediated dilatation of the basilar artery in vivo. *Circ Res*. 1991;69(3):697-705.
140. Ogawa S, Tank DW, Menon R, Ellermann JM, Kim SG, Merkle H, et al. Intrinsic Signal Changes Accompanying Sensory Stimulation - Functional Brain Mapping with Magnetic-Resonance-Imaging. *P Natl Acad Sci USA*. 1992;89(13):5951-5.
141. Ekstrom A. How and when the fMRI BOLD signal relates to underlying neural activity: The danger in dissociation. *Brain Res Rev*. 2010;62(2):233-44.
142. Mitzdorf U. Current source-density method and application in cat cerebral cortex: investigation of evoked potentials and EEG phenomena. *Physiological reviews*. 1985;65(1):37.
143. Khawaja FA, Tsui JMG, Pack CC. Pattern motion selectivity of spiking outputs and local field potentials in macaque visual cortex. *The Journal of Neuroscience*. 2009;29(43):13702.
144. Logothetis NK, Pauls J, Augath M, Trinath T, Oeltermann A. Neurophysiological investigation of the basis of the fMRI signal. *Nature*. 2001;412(6843):150-7.
145. Heeger DJ, Ress D. What does fMRI tell us about neuronal activity? *Nat Rev Neurosci*. 2002;3(2):142-51.
146. Rees G, Friston K, Koch C. A direct quantitative relationship between the functional properties of human and macaque V5. *Nature Neuroscience*. 2000;3(7):716-23.
147. Mukamel R, Gelbard H, Arieli A, Hasson U, Fried I, Malach R. Coupling between neuronal firing, field potentials, and FMRI in human auditory cortex. *Science*. 2005;309(5736):951-4.
148. Viswanathan A, Freeman RD. Neurometabolic coupling in cerebral cortex reflects synaptic more than spiking activity. *Nat Neurosci*. 2007;10(10):1308-12.
149. Baker TI, Issa NP. Cortical maps of separable tuning properties predict population responses to complex visual stimuli. *J Neurophysiol*. 2005;94(1):775-87.

150. Yen CC-C, Fukuda H, Kim S-G, editors. The Spatiotemporal Characteristics of Visual Stimulus-Induced BOLD Responses in Cat Visual Areas. International Society for Magnetic Resonance in Medicine; 2010; Stockholm, Sweden.
151. Yen CC-C, Fukuda H, Kim S-G, editors. Temporal Frequency- and Time-dependent BOLD and CBV fMRI Signals in Cat Visual Areas 17 and 18. International Society for Magnetic Resonance in Medicine; 2009; Honolulu.
152. Brainard DH. The Psychophysics Toolbox. *Spat Vis*. 1997;10(4):433-6.
153. Park SH, Masamoto K, Hendrich K, Kanno I, Kim SG. Imaging brain vasculature with BOLD microscopy: MR detection limits determined by in vivo two-photon microscopy. *Magn Reson Med*. 2008;59(4):855-65. PMID: 2628751.
154. Kim T, Kim S-G. Temporal dynamics and spatial specificity of arterial and venous blood volume changes during visual stimulation: implication for BOLD quantification. *J Cereb Blood Flow Metab*. 2011;31(5):1211-22.
155. Jesmanowicz A, Bandettini PA, Hyde JS. Single-shot half k-space high-resolution gradient-recalled EPI for fMRI at 3 tesla. *Magnet Reson Med*. 1998;40(5):754-62.
156. Haacke EM, Lindskogj ED, Lin W. A fast, iterative, partial-fourier technique capable of local phase recovery. *Journal of Magnetic Resonance (1969)*. 1991;92(1):126-45.
157. Moelker A, Pattynama PM. Acoustic noise concerns in functional magnetic resonance imaging. *Hum Brain Mapp*. 2003;20(3):123-41.
158. Beckmann CF, Smith SM. Probabilistic independent component analysis for functional magnetic resonance imaging. *IEEE transactions on medical imaging*. 2004;23(2):137-52.
159. Smith SM, Jenkinson M, Woolrich MW, Beckmann CF, Behrens TEJ, Johansen-Berg H, et al. Advances in functional and structural MR image analysis and implementation as FSL. *Neuroimage*. 2004;23:S208-S19.
160. Rorden C, Karnath HO, Bonilha L. Improving lesion-symptom mapping. *J Cogn Neurosci*. 2007;19(7):1081-8.
161. Strupp J. Stimulate: a GUI based fMRI analysis software package. *Neuroimage*. 1996;3(3):S607-S.
162. Abramoff MD, Magalhaes P, Ram S. Image processing with ImageJ. *Biophotonics international*. 2004;11(7):36-43.
163. Jin T, Kim SG. Cortical layer-dependent dynamic blood oxygenation, cerebral blood flow and cerebral blood volume responses during visual stimulation. *Neuroimage*. 2008;43(1):1-9. PMID: 2579763.

164. Moisy F. EzyFit - A free curve fitting toolbox for Matlab <http://www.fast.u-psud.fr/ezyfit/>. 2011 [updated 2011; cited]; Available from: <http://www.fast.u-psud.fr/ezyfit/>.
165. Winters W, Spector E, Wallach D, Shideman F. Metabolism of thiopental-S35 and thiopental-2-C14 by a rat liver mince and identification of pentobarbital as a major metabolite. *The Journal of pharmacology and experimental therapeutics*. 1955;114(3):343.
166. Issa NP, Rosenberg A, Husson TR. Models and measurements of functional maps in V1. *J Neurophysiol*. 2008;99(6):2745-54.
167. Mullen KT, Thompson B, Hess RF. Responses of the human visual cortex and LGN to achromatic and chromatic temporal modulations: an fMRI study. *Journal of vision*. 2010;10(13):13.
168. Nordmann JP, Casanova C, Denis P, Savard T, Saraux H. Tuning properties of spatial and temporal channels of vision Clinical consequences. *Neuro-Ophthalmology*. 1994;14(1):9-14.
169. Payne BR, Peters A. *The cat primary visual cortex*. San Diego: Academic Press; 2002.
170. Chalupa LM, Werner JS, Barnstable CJ. *The visual neurosciences*: MIT press; 2004.
171. Krukowski AE, Miller KD. Thalamocortical NMDA conductances and intracortical inhibition can explain cortical temporal tuning. *Nature Neuroscience*. 2001;4(4):424-30.
172. Pawela CP, Hudetz AG, Ward BD, Schulte ML, Li R, Kao DS, et al. Modeling of region-specific fMRI BOLD neurovascular response functions in rat brain reveals residual differences that correlate with the differences in regional evoked potentials. *Neuroimage*. 2008;41(2):525-34. PMID: 2483240.
173. Van Camp N, Verhoye M, De Zeeuw CI, Van der Linden A. Light stimulus frequency dependence of activity in the rat visual system as studied with high-resolution BOLD fMRI. *J Neurophysiol*. 2006;95(5):3164-70.
174. Zhang N, Zhu XH, Zhang Y, Chen W. An fMRI study of neural interaction in large-scale cortico-thalamic visual network. *Neuroimage*. 2008;42(3):1110-7. PMID: 2593731.
175. Rooney BJ, Cooper RM. Effects of square-wave gratings and diffuse light on metabolic activity in the rat visual system. *Brain Research*. 1988;439(1-2):311-21.
176. Orban GA, Kennedy H, Maes H. Response to movement of neurons in areas 17 and 18 of the cat: velocity sensitivity. *J Neurophysiol*. 1981;45(6):1043-58.
177. Khaytin I, Chen X, Royal DW, Ruiz O, Jermakowicz WJ, Siegel RM, et al. Functional organization of temporal frequency selectivity in primate visual cortex. *Cereb Cortex*. 2008;18(8):1828-42. PMID: 2790394.

178. Ribot J, Ozawa K, Tani T, Milleret C, S. T, editors. Spatio-temporal frequency preference map in cat primary visual cortex. *Proceeding of Society for Neuroscience*; 2008; Washington, DC.
179. Sun P, Ueno K, Waggoner RA, Gardner JL, Tanaka K, Cheng K. A temporal frequency-dependent functional architecture in human V1 revealed by high-resolution fMRI. *Nat Neurosci*. 2007;10(11):1404-6.
180. Saul AB, Feidler JC. Development of response timing and direction selectivity in cat visual thalamus and cortex. *J Neurosci*. 2002;22(7):2945-55.
181. Wibrall M, Muckli L, Melnikovic K, Scheller B, Alink A, Singer W, et al. Time-dependent effects of hyperoxia on the BOLD fMRI signal in primate visual cortex and LGN. *Neuroimage*. 2007;35(3):1044-63.
182. Li B, Freeman RD. High-resolution neurometabolic coupling in the lateral geniculate nucleus. *J Neurosci*. 2007;27(38):10223-9.
183. Nair P, Whalen WJ, Buerk D. PO₂ of cat cerebral cortex: response to breathing N₂ and 100 per cent O₂. *Microvasc Res*. 1975;9(2):158-65.
184. Padnick LB, Linsenmeier RA, Goldstick TK. Oxygenation of the cat primary visual cortex. *J Appl Physiol*. 1999;86(5):1490-6.
185. Masamoto K, Kim T, Fukuda M, Wang P, Kim S-G. Relationship between Neural, Vascular, and BOLD Signals in Isoflurane-Anesthetized Rat Somatosensory Cortex. *Cerebral Cortex*. 2007;17(4):942-50.
186. Sanchez-Ferrer C, Marin J, Salaices M, Rico M, Munoz-Blanco J. Interference of pentobarbital and thiopental with the vascular contraction and noradrenaline release in human cerebral arteries. *General Pharmacology: The Vascular System*. 1985;16(5):469-73.
187. Newman MF, Croughwell ND, White WD, Sanderson I, Spillane W, Reves JG. Pharmacologic electroencephalographic suppression during cardiopulmonary bypass: a comparison of thiopental and isoflurane. *Anesth Analg*. 1998;86(2):246-51.
188. Maier A, Wilke M, Aura C, Zhu C, Ye FQ, Leopold DA. Divergence of fMRI and neural signals in V1 during perceptual suppression in the awake monkey. *Nat Neurosci*. 2008;11(10):1193-200. PMID: 2754054.
189. Singh M, Kim S, Kim TS. Correlation between BOLD-fMRI and EEG signal changes in response to visual stimulus frequency in humans. *Magnet Reson Med*. 2003;49(1):108-14.
190. Martuzzi R, Murray MM, Meuli RA, Thiran JP, Maeder PP, Michel CM, et al. Methods for determining frequency- and region-dependent relationships between estimated LFPs and BOLD responses in humans. *J Neurophysiol*. 2009;101(1):491-502.

191. Muthukumaraswamy SD, Singh KD. Spatiotemporal frequency tuning of BOLD and gamma band MEG responses compared in primary visual cortex. *Neuroimage*. 2008;40(4):1552-60.
192. Hirsch JA, Martinez LM. Laminar processing in the visual cortical column. *Curr Opin Neurobiol*. 2006;16(4):377-84.
193. Schmid RS, Anton ES. Role of integrins in the development of the cerebral cortex. *Cereb Cortex*. 2003;13(3):219-24.
194. Yang X, Renken R, Hyder F, Siddeek M, Greer CA, Shepherd GM, et al. Dynamic mapping at the laminar level of odor-elicited responses in rat olfactory bulb by functional MRI. *Proc Natl Acad Sci U S A*. 1998;95(13):7715-20. PMID: 22734.
195. Logothetis NK. The neural basis of the blood-oxygen-level-dependent functional magnetic resonance imaging signal. *Philos Trans R Soc Lond B Biol Sci*. 2002;357(1424):1003-37. PMID: 1693017.
196. Goense JB, Logothetis NK. Laminar specificity in monkey V1 using high-resolution SE-fMRI. *Magn Reson Imaging*. 2006;24(4):381-92.
197. Lu H, Patel S, Luo F, Li SJ, Hillard CJ, Ward BD, et al. Spatial correlations of laminar BOLD and CBV responses to rat whisker stimulation with neuronal activity localized by Fos expression. *Magn Reson Med*. 2004;52(5):1060-8.
198. Harel N, Lin J, Moeller S, Ugurbil K, Yacoub E. Combined imaging-histological study of cortical laminar specificity of fMRI signals. *Neuroimage*. 2006;29(3):879-87.
199. Mandeville JB, Marota JJ. Vascular filters of functional MRI: spatial localization using BOLD and CBV contrast. *Magn Reson Med*. 1999;42(3):591-8.
200. Kim T, Kim SG. Cortical layer-dependent arterial blood volume changes: improved spatial specificity relative to BOLD fMRI. *Neuroimage*. 2010;49(2):1340-9. PMID: 2819732.
201. Duong TQ, Silva AC, Lee SP, Kim SG. Functional MRI of calcium-dependent synaptic activity: cross correlation with CBF and BOLD measurements. *Magn Reson Med*. 2000;43(3):383-92.
202. Zhao F, Jin T, Wang P, Kim SG. Improved spatial localization of post-stimulus BOLD undershoot relative to positive BOLD. *Neuroimage*. 2007;34(3):1084-92. PMID: 1876719.
203. Stefanovic B, Hutchinson E, Yakovleva V, Schram V, Russell JT, Belluscio L, et al. Functional reactivity of cerebral capillaries. *J Cereb Blood Flow Metab*. 2008;28(5):961-72.
204. Weber B, Keller AL, Reichold J, Logothetis NK. The microvascular system of the striate and extrastriate visual cortex of the macaque. *Cereb Cortex*. 2008;18(10):2318-30.

205. Tieman SB, Mollers S, Tieman DG, White J. The blood supply of the cat's visual cortex and its postnatal development. *Brain Res.* 2004;998(1):100-12.
206. Leventhal AG, Hirsch HV. Receptive-field properties of neurons in different laminae of visual cortex of the cat. *J Neurophysiol.* 1978;41(4):948-62.
207. O'Keefe LP, Levitt JB, Kiper DC, Shapley RM, Movshon JA. Functional organization of owl monkey lateral geniculate nucleus and visual cortex. *J Neurophysiol.* 1998;80(2):594-609.
208. Hubel DH. *Eye, brain, and vision.* New York: Scientific American Library : Distributed by W.H. Freeman; 1988.
209. Chaigneau E, Oheim M, Audinat E, Charpak S. Two-photon imaging of capillary blood flow in olfactory bulb glomeruli. *Proc Natl Acad Sci U S A.* 2003;100(22):13081-6. PMID: 240748.
210. Xu F, Kida I, Hyder F, Shulman RG. Assessment and discrimination of odor stimuli in rat olfactory bulb by dynamic functional MRI. *Proc Natl Acad Sci U S A.* 2000;97(19):10601-6. PMID: 27071.
211. Logothetis N, Merkle H, Augath M, Trinath T, Ugurbil K. Ultra high-resolution fMRI in monkeys with implanted RF coils. *Neuron.* 2002;35(2):227-42.
212. Yen CC-C, Fukuda M, Kim S-G. BOLD responses to different temporal frequency stimuli in the lateral geniculate nucleus and visual cortex: Insights into the neural basis of fMRI. *Neuroimage.* In Press, Accepted Manuscript.
213. Moon CH, Fukuda M, Park SH, Kim SG. Neural interpretation of blood oxygenation level-dependent fMRI maps at submillimeter columnar resolution. *Journal of Neuroscience.* 2007;27(26):6892-902.
214. Shimokawa H, Yasutake H, Fujii K, Owada MK, Nakaike R, Fukumoto Y, et al. The importance of the hyperpolarizing mechanism increases as the vessel size decreases in endothelium-dependent relaxations in rat mesenteric circulation. *J Cardiovasc Pharmacol.* 1996;28(5):703-11.
215. Bakalova R, Matsuura T, Kanno I. Frequency dependence of local cerebral blood flow induced by somatosensory hind paw stimulation in rat under normo- and hypercapnia. *Jpn J Physiol.* 2001;51(2):201-8.
216. Zappe AC, Uludag K, Logothetis NK. Direct measurement of oxygen extraction with fMRI using 6% CO₂ inhalation. *Magn Reson Imaging.* 2008;26(7):961-7.
217. Cohen ER, Rostrup E, Sidaros K, Lund TE, Paulson OB, Ugurbil K, et al. Hypercapnic normalization of BOLD fMRI: comparison across field strengths and pulse sequences. *Neuroimage.* 2004;23(2):613-24.

218. Bandettini PA, Wong EC. A hypercapnia-based normalization method for improved spatial localization of human brain activation with fMRI. *NMR Biomed.* 1997;10(4-5):197-203.
219. Ho YC, Petersen ET, Zimine I, Golay X. Similarities and differences in arterial responses to hypercapnia and visual stimulation. *J Cereb Blood Flow Metab.* 2011;31(2):560-71.
220. Yezhuvath US, Lewis-Amezcu K, Varghese R, Xiao G, Lu H. On the assessment of cerebrovascular reactivity using hypercapnia BOLD MRI. *NMR Biomed.* 2009;22(7):779-86. PMID: 2726998.
221. Lopez de Pablo AL, Gonzalez MC, Dieguez G, Gomez B, Lluch S. Reduction of cerebrovascular reactivity during hypercapnia. *Am J Physiol.* 1982;242(5):R441-6.
222. Lu J, Dai G, Egi Y, Huang S, Kwon SJ, Lo EH, et al. Characterization of cerebrovascular responses to hypoxia and hypercapnia using MRI in rat. *Neuroimage.* 2009;45(4):1126-34.
223. Fernandez-Klett F, Offenhauser N, Dirnagl U, Priller J, Lindauer U. Pericytes in capillaries are contractile in vivo, but arterioles mediate functional hyperemia in the mouse brain. *Proc Natl Acad Sci U S A.* 2010;107(51):22290-5. PMID: 3009761.
224. Beaulieu C, Colonnier M. Number of neurons in individual laminae of areas 3B, 4 gamma, and 6a alpha of the cat cerebral cortex: a comparison with major visual areas. *J Comp Neurol.* 1989;279(2):228-34.
225. Zemelman BV, Lee GA, Ng M, Miesenböck G. Selective Photostimulation of Genetically ChARGed Neurons. *Neuron.* 2002;33(1):15-22.
226. Boyden ES, Zhang F, Bamberg E, Nagel G, Deisseroth K. Millisecond-timescale, genetically targeted optical control of neural activity. *Nat Neurosci.* 2005;8(9):1263-8.
227. Lee JH, Durand R, Gradinaru V, Zhang F, Goshen I, Kim DS, et al. Global and local fMRI signals driven by neurons defined optogenetically by type and wiring. *Nature.* 2010;465(7299):788-92.